Spring 2019

Leading-edge vortex development on a maneuvering wing in a uniform flow

Kevin Wabick
University of Iowa

LEADING-EDGE VORTEX DEVELOPMENT ON A MANEUVERING WING IN A UNIFORM FLOW

by

Kevin Wabick

A thesis submitted in partial fulfillment of the
requirements for the Doctor of Philosophy
degree in Mechanical Engineering
in the Graduate College of
The University of Iowa

May 2019

Thesis Supervisor: Associate Professor James H. J. Buchholz

ACKNOWLEDGEMENTS

I would like to begin by thanking Professor James Buchholz for the tremendous encouragement, guidance and support that he has provided to me throughout this endeavor. Without his inspiration, optimism and confidence in my abilities, this work could not have been accomplished. I would also like to thank him for affording me the privilege of participating in the Air Force Summer Faculty Fellowship Program and for giving me the opportunity to present my work at several conferences.

I would also like to thank my esteemed committee members, Prof. Pablo Carrica, Prof. Casey Harwood , Prof. Albert Ratner and Prof. Brian Thurow for their valuable time and insightful discussion.

It has been my pleasure to work with an amazing research team at the University of Iowa. Azar Eslam Panah, Jim Akkala, and Austin Krebill, in particular, have been outstanding co-collaborators and I am fortunate to have had the chance to work with them.

I also like to extended much gratitude to the researchers that directly helped tackle the problem at hand. Randall Berdon, without the guidance from his flow visualizations, the parameters would not have been as evident. Kyle Johnson, who came to the University of Iowa with the Plenoptic camera system, in which made this problem tractable. Prof. James Buchholz and Prof. Brian Thurow for all the help, and guidance that was given over the course of this experiment, I can not thank you enough. I am honored to have worked with the entire team.

Last but not least, I want to thank my parents for all of their unwavering support in

all my endeavors, in which none of this would be possible.

This work was supported in part by the Air Force Office of Scientific Research, award number FA9550-1-16-0107.

ABSTRACT

Vortices interacting with the solid surface of aerodynamic bodies are prevalent across a broad range of geometries and applications, such as dynamic stall on wind turbine and helicopter rotors, the separated flows over flapping wings of insects, birds, formation of the vortex wakes of bluff bodies, and the lift-producing vortices formed by aircraft leading-edge extensions and delta wings. This study provides fundamental insights into the formation and evolution of such vortices by considering the leading-edge vortices formed in variations of a canonical flapping wing problem.

Specifically, the vorticity transport for three distinct maneuvers are examined, a purely rolling wing, a purely pitching wing and a rolling and pitching wing, of aspect-ratio two. Once the maneuvers are characterized, a passive bleed hole will be introduced to a purely rolling wing, to alter flow topology and vorticity transport governing the circulation on the wing.

Three-dimensional representations of the velocity and vorticity fields were obtained via plenoptic particle image velocimetry (PPIV) measurements are used to perform a vorticity flux analysis that serves to identify the sources and sinks of vorticity within the flow. Time-resolved pressure measurements were obtained from the surface of the airfoil, and used to characterize the flux of vorticity diffusing from the solid surface.

Upon characterizing all of the sources and sinks of vorticity, the circulation budget was found to be fully accounted for. Interpretation of the individual vorticity balance contributions demonstrated the Coriolis acceleration did not contribute to vorticity generation

and was a correction term for the apparent vorticity. The transport characteristics varied among the three cases that were investigated. The spanwise convective contribution was signification over various spanwise locations for the pure roll case. For the pure pitch the shear layer contribution and the diffusive contribution. The circulation was dependent the pitch rate, which was evident only at the beginning of the motion, and circulation growth at later times depended only on the pitch angle.The combined pitch roll cases, the transport behavior strongly resembled that of pitch, with little evidence of roll influence, despite that the flow structure and circulation distribution on the inboard part of the wing exhibited roll-like behaviors. In the final case where the wing is pitching and rolling , the shear layer contribution was balanced by the diffusive contribution, similar to that of the pure pitch case. By adding a passive bleed hole to the purely rolling cases, it was found to alter the both the flow topology and vorticity transport.

PUBLIC ABSTRACT

The interaction between vortices and the solid surface of an aerodynamic body is a ubiquitous feature of high-angle-of-attack aerodynamics associated with a broad range of aerospace structures, including maneuvering and flapping wings, blades on helicopter rotors and gas turbine engines, the aerodynamic forebodes of missiles and high-performance aircraft. This study provides fundamental insights into the development of such vortices by considering the vortex formed at the leading edge of a rotating airfoil in a free-stream.

The primary goal of this work was to rigorously characterize the formation and evolution of the leading-edge vortex (LEV) based on the transport of vorticity both the bulk flow, and the near surface of the airfoil. By performing this novel analysis that served to quantify the effect of rotational accelerations has on the formation and evolution an a LEV, which were found to be insignificant. It was also shown, that a wing rolling in a free-stream can contain a myriad of behaviors. Each of these behaviors had different evolutions from a vorticity transport perspective. Rotating about a different axis to preform a pitching maneuver, resulted in relatively 2D behavior.

By explicitly characterizing how the vortex-airfoil interaction affects the evolution of the LEV, the results of this study have significantly enhanced our understanding of why the LEV develops the way it does, and how rotational accelerations alter this development. The insight into the vortex dynamics this work provides, guides future work to novel flow control strategies for altering aerodynamic loads in a meaningful manner.

TABLE OF CONTENTS

LIST OF TABLES

Table

LIST OF FIGURES

Figure

NOMENCLATURE

AoA	Ange of attack
α	Geometric angle of attack while pitching
$\dot{\alpha}$	Pitch Rate
ϕ	Roll angle
$\dot{\phi}$	Roll rate
α_{eff}	The effective angle of attack modified by the downwash
$k = \frac{\dot{\alpha}c}{2U_\infty}$	Reduced Pitch Rate
R_g	Radius of Gyration
R_g/c	Non-dimensional Radius of gyration
U_∞	Free-Stream Velocity, m/s
U_{Rg}	Velocity at Radius of gyration
Ω_x	Angular velocity of roll
J	Advance Coefficient
k_{Rg}	effective Pitch rate during a roll maneuver
APG	Adverse Pressure Gradient
AR	Aspect-Ratio
BVF	Boundary Vorticity Flux
SPCF	Spanwise Convective Flux
c	Chord Length, m
$C_p = \frac{p - p_\infty}{0.5\rho U_\infty^2}$	Pressure Coefficient

FPG	Favorable Pressure Gradient
Γ	Circulation, m^2/s
LEV	Leading-Edge Vortex
ν	Kinematic Viscosity, m^2/s
ω	Vorticity, s^{-1}
OSV	Opposite-Signed Vortex
PIV	Particle Image Velocimetry
ρ	Density, kg/m^3
$Re_C = \frac{U_\infty c}{\nu}$	Chord-Based Reynolds Number
s	Airfoil Span, m
TEV	Trailing-Edge Vortex
TiV	Tip Vortex
u	Velocity, m/s

CHAPTER 1
INTRODUCTION

Interactions between vortices and solid surfaces are ubiquitous in engineering applications. Some examples include, dynamic stall vortices , the streamwise vortices separating from the forebodies of air vehicles (Figure 1.1a), delta wings (Figure 1.1b and Figure 1.1c), biological locomotion, wind turbine blades, and propellers. Present day engineered air vehicles outperform biological locomotion in velocity and altitude. However, natural fliers and swimmers can outperform at low-speeds and at small scales. Shelton et al. [72] observed cliff swallows in tandem flight performing maneuvers up to 7.8 g's. Fixed wing aircraft can match the high speed and accelerations of natural swimmers and fliers, but lack the capability to harness the power of the unsteady nature of these low speed flows. Birds of prey have to be fast and agile. For example, Aquila nipalensis utilize control devices, both passive separation of specialized feathers, and active manipulation of the alula, specifically for such low-speed perching [16]. Rotary-wing aircraft are capable of bird-like, low-speed performance, like the perching demonstrated by Doyle et al. [22], but have thrust-to-weight ratios rarely exceeding three. Natural flyers and swimmers achieve the above capabilities efficiently and with little noise, and this is why scientists have looked towards these creatures to harness their unsteady nature for performance, noise-reduction and the active and passive flow control capabilities.

Rotating aerodynamic bodies and plates have been shown to achieve lift coefficients that are higher than their translating counterparts since stall is delayed until higher angles of attack [4, 49, 78, 79, 80]. For the National Renewable Energy Laboratory (NREL)

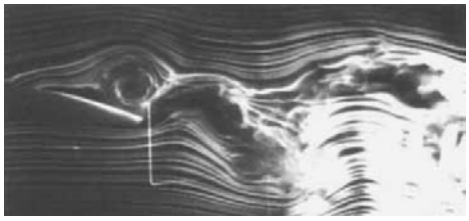

(a) Smoke-wire flow visualization of the dynamic stall vortex formed on a pitching NACA 0012 airfoil. Adopted from Panda and Zaman [62].

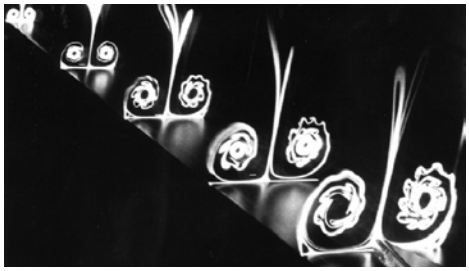

(b) Flow visualization of the leading-edge vortices formed on aerodynamic body. Adopted from Nelson and Pelletier [56].

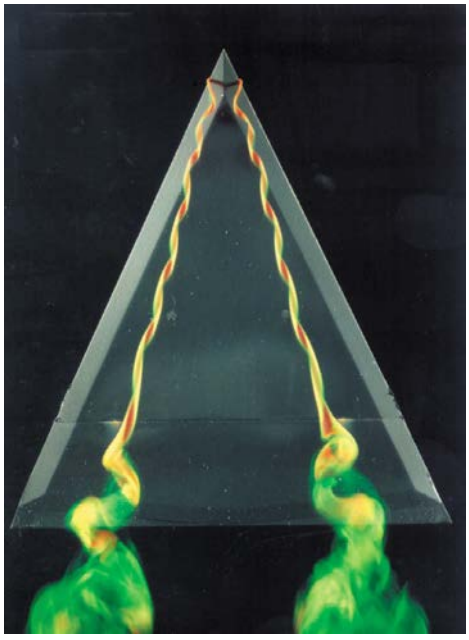

(c) Dye visualization of the leading edge highlighting spanwise vortex structures formed by a delta wing.

Figure 1.1: Flow visualizations of the vortical structures shed from the leading edge of a variety of aerodynamic bodies.

S809 airfoil, Tangler [78] showed that the lift coefficient increased by as much as 2.5 times at inboard radial positions during rotation compared to the translation case at the same effective angle of attack. However, the fundamental mechanisms that maintain an attached Leading edge vortex (LEV) on a rotating body are not understood [10, 25, 48, 49]. A rotating blade creates a conical LEV which, under certain conditions can remain attached to the wing. Lentink and Dickinson [49] have shown that the aerodynamics of flapping flight relies significantly on the generation of a large, conical LEV [20].

In the work presented here, the LEV formation and evolution on rotating wings will be examined through the lens of vorticity transport, in a non-inertial reference frame, which is attached to the wing. Using this framework, the highly debated rotational accelerations can be studied, for various rotating wings in a free-stream. Once understood, the kinematics will be combined into a pitching and rolling wing in a free-stream, to examine how robust these rotational accelerations are. Since vorticity transport is being used to quantify the flow, this gives insight into what transport contributions can be manipulated to augment the flow. Alternatively, can the flow be perturbed in a meaningful manner, such as increasing lift or maintaining lift. By quantifying the sources and sinks of this transport and correctly quantifying circulation, the circulation can be correlated back to lift. The overarching goal of this work will be to provide a more thorough description of the LEV formation processes that determine how the LEV develops and the extent to which rotational accelerations contribute.

The following is a brief summery that will be covered in this manuscript. In Chapter 2, a review of relevant literature that supports the comping chapters. The topics consist

of vortex formation, spanwise flow on aerodynamic bodies, rotational accelerations and vorticity transport. Chapter 3 will cover an in depth derivation of the vorticity transport equation in the non-inertial reference frame, and look at the effects of rotational accelerations, and on the diffusive term. In chapter 4, the experimental setup and procedures will be covered. Chapter 5 will examine four different pure rolling cases in a free-stream. This will give insight into the development of conical LEVs and how rotational accelerations contribute and manifest themselves. Chapter 6 will examine a wing undergoing a pure pitching motion, which will set up a reference case for a later study. Chapter 7 will examine a wing that will perform a pitching maneuver during a roll maneuver. This simultaneous pitching and rolling maneuver, will emulate an aggressive maneuver performed by an aircraft or by a bird of prey. Chapter 8 will re-examine the pure roll maneuver, but this time a passive bleed hole will be introduced, in an attempt to alter flow topology, flux contributions and aerodynamics forces. Finally, Chapter 9 will summarize the findings in this manuscript and propose some future work.

CHAPTER 2
LITERATURE REVIEW

This chapter will review prior observations of flow topology, aerodynamic performance, and mechanisms of LEV development on various kinematics, such as translating, pitching and rotating aerodynamic bodies and what sets them apart from each other. This will cover natural fliers and the driving fluid mechanics isolating rotating motions on simple geometries.

2.1 The Leading-Edge Vortex

The formation of the leading-edge-vortex is due to the instability in the shear layer and roll-up of the separated shear layer. This roll up can alter the dynamics around the wing, which, then affects the separated flow emanating from the leading edge. The conditions in which the LEV forms govern the vorticity fluxes contributing to its growth or decay. An example of this is the surface pressure gradients established by the vortex interacting with the boundary leading to the generation of opposite-sign vorticity [51, 94], which can cause significant decay of the vortex through cross-cancellation [89, 88]. This section serves to review our current understanding of the formation, evolution and aerodynamic effect of the leading-edge vortex.

2.1.1 LEV Formation Process

The formation of an LEV is preceded by the formation of a boundary layer on the surface of an airfoil, due to the no-slip condition at the boundary. At this point there is no

identifiable coherent vortical structure. A fundamental way to alter the fluid dynamics that lead to the formation of an LEV over a wing is by changing the angle of attack. This change causes the stagnation point on the surface of the airfoil to move away from the leading edge. The result of this process is the development of an adverse pressure gradient (APG) upon the surface of the airfoil near the leading edge [21, 33]. The incipient formation of the LEV begins as the APG of sufficient strength is forced upon the boundary layer, triggering an ejection of vorticity into the flow from the surface [81, 21]. In 1980 Van Dommelen and Shen [81] showed that the formation of a stagnation point on the surface of the airfoil would spontaneously generate a singularity in the laminar boundary layer equation. The separation process has since been characterized as the formation of reversed flow at the surface of the airfoil and once the boundary layer separates, the structure rolls up to create the leading-edge vortex. After the LEV separates, it remains connected to the leading edge via a shear layer that provides a continued flux of vorticity into the LEV to increase its circulation. As the LEV continues to grow, it begins to impose large pressure gradients on the surface of the airfoil. Due to the no-slip condition, this leads to the formation of a layer of opposite-signed vorticity beneath the LEV [1, 35].

The LEV is considered detached when the connection to the feeding shear layer is broken, preventing the main source of circulation to cease, and halting the additional accumulation of circulation. The process can be described using ideas from turbulent boundary layer theory, where the approach of the LEV towards the surface of the airfoil results in a "sweep event" that causes an eruption of opposite-signed vorticity [21, 6]. In most cases the phenomenon is characterized as the layer of opposite-signed vorticity accumulating

enough circulation for it to break the connection between the LEV and its feeding shear layer [1]. This process was first described by Acharya and Metwally [1] when they showed opposite-sign vorticity cutting off a dynamic-stall vortex from the leading-edge shear layer. In their study of a plunging airfoil, Lewin and Haj-Hariri [50] also found the evolution of the secondary vorticity to play a significant role in the detachment of the LEV.

$$k = \pi f c / U_\infty \tag{2.1}$$

While it has been accepted that the detachment of the LEV is caused by the interaction between the LEV and secondary vortex, there are multiple ways in which secondary vorticity can be introduced into the flow. Widmann and Tropea [86] describe two fundamental mechanisms by which the detachment of the LEV can occur: bluff body detachment and boundary layer eruption. They used topological analyses to characterize these mechanisms, as shown in Figures 2.1 and 2.2. In bluff body detachment, the LEV separates from the airfoil but maintains a reattachment point that proceeds to move downstream (Figure 2.1a). When the reattachment point reaches the trailing edge, the LEV detaches and allows reverse flow to extend up the airfoil from the trailing edge (Figure 2.1b). On the other hand, the boundary layer eruption detachment mechanism occurs when the viscous vortex-wall interaction causes an eruption of secondary vorticity from beneath the LEV before the reattachment point of the LEV reaches the trailing edge. This breaks the topology between the shear layer and the LEV by forming a counter-rotating region between the two, the division of which incites detachment. As the advection of the reattachment point of an LEV has been shown to be dependent on reduced frequency [18], this transition to the boundary

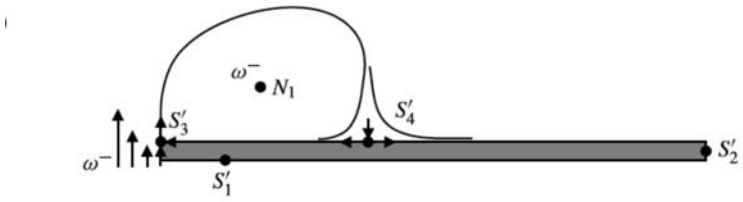

(a)

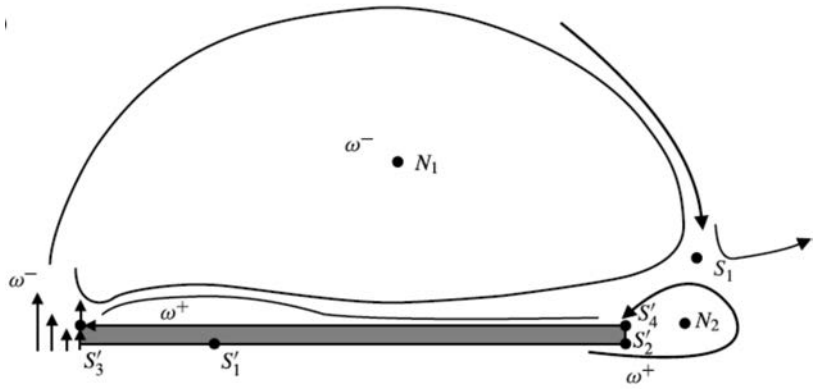

(b)

Figure 2.1: Topological representation of the bluff body detachment mechanism from Widmann and Tropea [86].

layer eruption mechanism is associated with high frequency motions shown in equation 2.1. where f is the motion frequency, c is chord length and U_∞ is the free-stream velocity. While boundary layer eruption has been studied for a plate in pure pitch, it has yet to be looked at wing in a pure rotating motion.

2.1.2 LEV Scaling

Interest in the LEV primarily stems from its ability to produce large lift values, a byproduct of the high kinetic energy within the LEV generating low pressure regions on

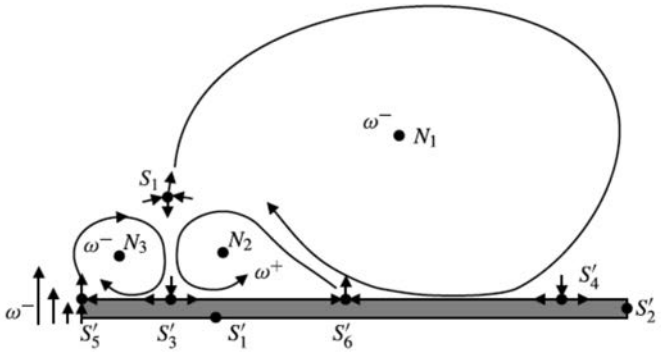

Figure 2.2: Topological representation of the boundary layer eruption mechanism. Adopted from Widmann and Tropea [86]. The plate is a plunging kinematic, where the plate moves perpendicular to the free-stream.

the upper surface of the airfoil. It has long since been established that the total lift produced by an airfoil is related to the total circulation of the flow [96] and the fact that most of the circulation about an airfoil is contained within the LEV [63] results in the maximum lift values being achieved just before detachment of the LEV [37]. Thus, developing a non-dimensional circulation-threshold for the detachment of the LEV provides a useful means for characterizing the maximum lift of an airfoil. Although many attempts have been made to come up with a universal scaling, no such scaling has been founds, which means there is still governing mechanism that still needs to be found. The following paragraphs will highlight some general ways that scaling has been applied to specific flows.

Since the bluff body detachment mechanism is characterized by the reattachment point of the LEV arriving at the trailing edge, some studies have demonstrated success in using the chord length to scale the circulation of an LEV [69, 43]. However, Widmann

and Tropea [86] showed that for a plate in a plunging kinematic, this was an insufficient scaling parameter in the case of the eruption-based detachment, as it had no way to account for the viscous effects near the leading edge that inevitably cause the eruption of secondary vorticity. Instead, they found the best way to scale the circulation of the LEV was to use the thickness of the shear layer (Figure 2.3). Alternatively, both Rival et al. [70] and Kriegseis et al. [46] found the effective shear-layer velocity to be a suitable scaling parameter for the LEV circulation. Akkala et al. [2] proposed yet another scaling parameter for leading-edge vortex circulation using a kinematically-based velocity and length scale, which was found to be particularly effective for flexible plunging airfoils. Buchholz et al. [13] demonstrated success in scaling the total circulation shed by finite aspect-ratio pitching panels based on a simple model of surface pressure gradients. Yet in spite of the many scaling parameters that have been proposed, no robust predictor of LEV circulation has been identified. This is primarily because the boundary layer eruption mechanism is still poorly understood, and without sufficient knowledge of the pertinent flow physics it becomes very difficult to identify any sort of unifying principle.

2.2 Kinematics and Leading Edge Vortex Formation

Basic research on maneuvering wings has focused on simple canonical motions to isolate physical mechanisms present in unsteady aerodynamics of engineered vehicles and biological locomotion. The basic kinematics are forward translation, pitching, plunging and rotation (rolling). Since the formation of an LEV is a non-linear process, these base kinematics can not be superimposed on one another, but can give insight into fundamental

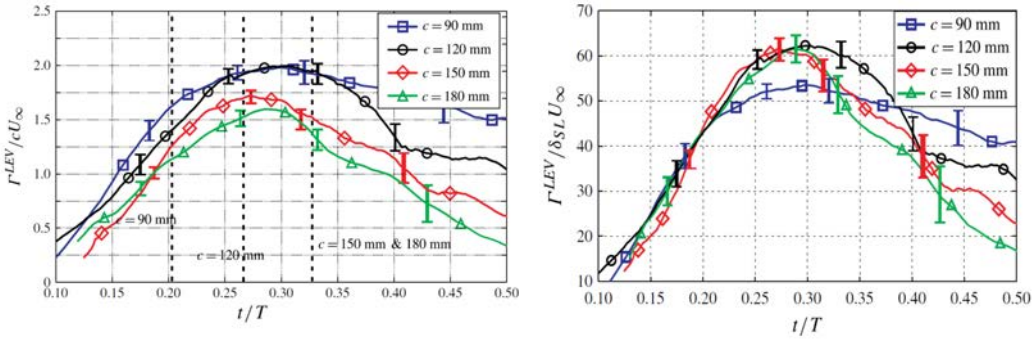

Figure 2.3: Scaled LEV circulation using chord length (left) and shear layer thickness (right) for the four chord lengths tested by Widmann and Tropea. Adopted from Widmann and Tropea [86].

mechanisms that are governing the LEV.

2.2.1 Translating Plates

The simplest kinematics is that of a pure translation, which is defined by a wing at fixed angle of attack, typically starting from rest in a quiescent flow. A leading-edge vortex is usually created and shed within the first few chord lengths of travel, with a commensurate rise and rapid drop in lift.

By increasing the wing velocity (freesteam) this will vary the generation of the LEV and the circulation. This, in turn, affects the shedding and directly the force history. The velocity of the plate will dictate the strength, and structure, of the LEV. Increasing the velocity will lead to more compact, stronger LEV, while a slower velocity will lead to weaker vortices and lower forces [17, 53]. Once the LEV has shed, the trajectory of the LEV is relatively robust [53, 52]. Once the LEV has shed the startup transient will persists

for many convective times until a fully developed wake is established.

While the force history is driven by the LEV, it is also a direct function of the added mass [68, 64]. When the added mass component is removed, it can be show that the remaining circulatory force, is not as influenced by impulsively starting motions [17]. Early in the motion, the trailing-edge vortex (TEV) is still rolling up and all of the circulation is contained in the LEV and TEV [64]. The circulation within the LEV and TEV are nearly equal and opposite, which makes the bounded circulation contribution small. The total lift force on the plate can be attributed to added mass and LEV [68, 65].

Finite wings have more three-dimensionality which derives partially from the tip vortex, which affects both the formation of the LEV and, by extension, the shedding process. With increasing aspect ratios, these three-dimensional effects decrease, but still can exhibit spanwise arch vortices and stall cells. Through both numerical simulations and flow visualizations experiments it has been shown that, at early times in the motion, the flow development is relatively insensitive to aspect ratio (AR=1,2, and 4). Figure 2.4 shows an impulsively started translating wing. Flow separates at the leading and trailing edge and forms a closed loop vortex system. The wake of the wing becomes more sensitive to aspect ratio as tip vortices gain strength. For instance, in the AR=1 case in figure 2.4 the tip vortices cover nearly the entire surface, which causes the vortex sheet to detach. At higher aspect ratios this effect is not seen. For the AR=2 and 4 case the shear layer separates from the wing and forms an arch [77, 45].

The overall dynamics of the LEV on a translating rectangular wing have distinct features, such as, a tip vortex that increases spanwise flow. In higher aspect ratio cases,

vorticity transport in these two-dimensional kinematics is not great enough to allow for an LEV to remain attached for longer period of times [77, 53].

2.2.2 Pitching Plates

A pitching maneuver is when a wing changes its angle of attack in time, shown in figure 2.5. This motion is governed by reduced frequency (Eq. 2.1), $k = \pi f c / U_\infty$, pitch axis location x_p/c, and aspect ratio. It is important to note that the Reynolds number has a relatively unimportant role in the studies conducted from $Re = 100 - 100,000$, in which they all share a common behavior [57]. The LEV dynamics are also seemingly unaffected by the wings' cross-sectional geometry. Beside for the differences in the pitch angles, during which large events take place, the literature shows the same physical mechanisms and trends for the other parameters.

Many have studied this problem through flow visualizations [85, 74, 98, 30] or numerical investigations [38, 84, 23, 38, 83], to shed light on the dynamics of a pitch up maneuver, which have shown the flow follows a characteristic sequence of events. During low angles, the separation point starts near the trailing edge, and a recirculation zone forms just aft of this point. As the angle increases, the separation point moves towards the leading edge until it reaches the leading edge, at which point the flow departs from the quasi-steady behavior observed in the translating wing. At this point a closed loop of circulation forms, and the boundary layer begins to roll up and a LEV begins to form.

By increasing the dimensionless pitch rate, k, all the processes are observed but change in two ways. First, the LEV becomes more compact, and stronger and larger pres-

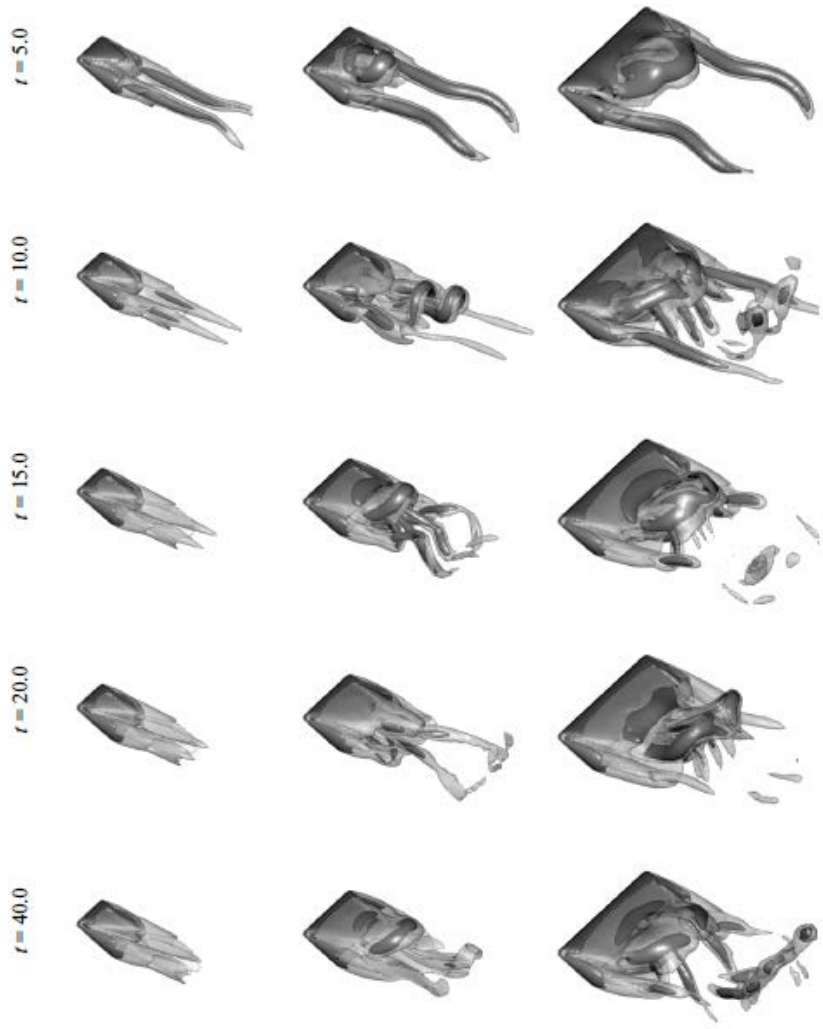

Figure 2.4: Top-port view of the wake vortices behind rectangular plates of AR=1,2 and 4 at $\alpha = 30^{\circ}$ in a translating motion.

Source: Taira and Colonius **Journal of Fluid Mech.** *623*, 187-207 (2009).

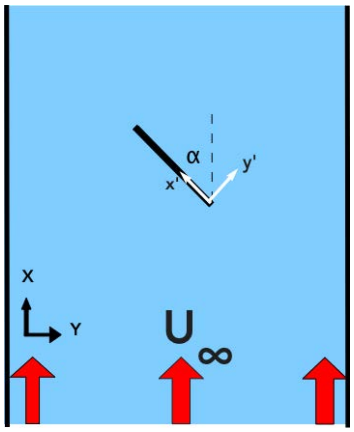

Figure 2.5: A diagram depicting a pitch maneuver where the pitch location is about the leading edge.

sure gradients are induced by the rotation. Second, many of the features (recirculation zone, LEV roll up) are delayed in the development, and shedding is delayed to higher angles of attack [85, 84, 30, 14, 44, 76]. Figure 2.6 shows a CFD computed on an AR=2 plate, at Re=300. In the first column the development looks similar to early time in a translating at a fixed incidence. However, once the LEV begins to roll up, is where the difference is are observed. An easily observable difference is the much smaller influence the tip vortices have on the overall flow.

Delays in aforementioned processes can also be seen by changing the pitch axis aft [84, 99]. The normal component to velocity at the leading edge, with respect of the incident flow is $U\left(sin\alpha - 2kx_p/c\right)$, which a change in either parameter will change this component. However, a change in the pivot location does not increase the LEV strength. It will merely move the processes in time. It was found that the peak suction increases with k but decreases with increasing x_p/c [84].

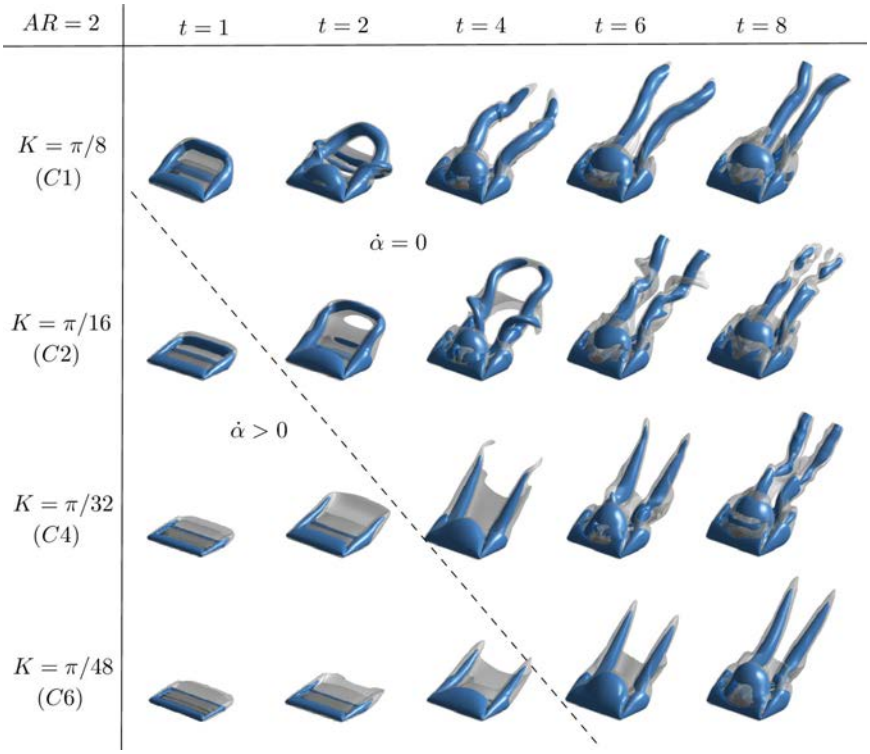

Figure 2.6: Instantaneous Q-criterion iso-surace and vorticity magnitude. Showing three-dimensional flow structure for an AR=2 flat plate at Re=300.

Source: Jantzen et. al. *Physics of Fluids* **26**, (2014).

A translating and pitching wing has different features than a wing at a fixed angle of incidence. A large difference can be seen in the force histories, since the wing is pitching and translating. There is the circulatory component form the leading and trailing edge vortices and the inertial mass from the movement. The lift in the pitching case can be achieved for longer times and reach larger values. During the formation of the LEV the two kinematics have similar loop vortices at early times in the motion. However, once the LEV rolls up in the pitch case that is where similarities end.

2.2.3 Rotating Plates

Compared to translating and pitching wings, a rotating blade, which is a blade under rotation about an axis parallel to the free-stream (fig. 2.7) , at high angle of attack, creates a conical LEV which, under certain conditions can remain attached to the wing, as shown in figure 2.8. Dickinson et al. [20] have shown that the aerodynamics of flapping flight relies significantly on the generation of a large, conical LEV. The initial development of this LEV occurs in the same manner to that of the translating wing. The vortex lift generated during the rotation remains throughout the motion.This is divergent to the LEV that forms on a translating wing and pitching wing that is shed into the wake followed by periodic shedding [77]. The works of Lentik and Dickinson, and Jardin and David [49, 40, 41], suggest that the Coriolis acceleration that accompanies rotation plays a key role in the robust attachment of the LEV.

Lentink and Dickinson [48, 49] performed a non-dimensionalization of the Navier-Stokes equation in a non-inertial reference frame for a purely rotating wing at a constant

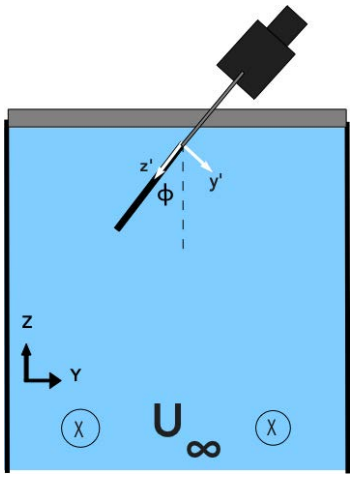

Figure 2.7: A diagram depicting a roll maneuver. In the absence of free-stream this maneuver is considered a rotating wing.

angular velocity to determine the effects of rotation which is shown in Equation 2.2, to show how rotating affected the flow.

$$\frac{D\mathbf{u}}{D\mathbf{t}} + \frac{1}{A^*}\frac{d\mathbf{\Omega}}{dt} \times \mathbf{r} + \frac{1}{Ro} \cdot \mathbf{\Omega} \times (\mathbf{\Omega} \times \mathbf{r}) + \frac{1}{Ro} \cdot 2\mathbf{\Omega} \times \mathbf{u} = -Eu \cdot \nabla \mathbf{p} + \frac{1}{Re} \cdot \nabla^2 \mathbf{u} \qquad (2.2)$$

Where the first term on the left hand side (LHS) is the unsteady term, the second term is the angular acceleration term over the stroke amplitude for an angular, A^*, for a given angular acceleration, $\mathbf{\Omega}$, the third term is the Centripetal acceleration, and the fourth and final term is the Coriolis acceleration term. On the right hand side (RHS) the first term is the pressure term and the second term is the viscous term, where Eu is the Euler number, defined as $Eu = p/\rho u^2$, where p is the pressure, ρ is the density, and u is the fluid velocity, and the Reynolds number, Re, is defined as $Re = \rho uc/\mu$, where ρ is the density, u is the free-stream, c is the chord length and μ is the dynamic viscosity. From

the nondimensionalization, it was shown that the centripetal and Coriolis accelerations (Equations 2.3 and 2.4, respectively) are governed by the inverse of the Rossby number ($Ro = R/c$; where R is the wingtip radius and c is the chord length).

$$a_{cent} = \frac{1}{Ro} \cdot \mathbf{\Omega} \times (\mathbf{\Omega} \times \mathbf{r}) \tag{2.3}$$

$$a_{Cor} = \frac{1}{Ro} \cdot 2\mathbf{\Omega} \times \mathbf{u} \tag{2.4}$$

In the case of translating wings, the Rossby number tends to infinity which makes a null contribution for the Coriolis and centripetal accelerations. However, the analysis shows that the centripetal and Coriolis accelerations could not be neglected in a rotation case since the Rossby number will be relatively low, and would influence LEV development.

The strength of the LEV is highly dependent on the angle of attack [59, 89], but interestingly the Reynolds number does not have an effect on the LEV strength [19, 59, 89]. It has been shown by Wojcik et. al [89] that the circulation of the LEV on a rotating wing at a given spanwise location exceeded the bound circulation predicted by thin airfoil theory, but Pitt Ford and Babinsky [63] show it still agreed well with the measured forces, supporting the claims that lift on the wing is the result of the LEV and not bound circulation.

Lentink and Dickinson observed for a $Re < 14,000$, over 300 species can be associated with a Rossby number of three [48]. In this range of Reynolds number the wings rotate about their root, and the Rossby number is proportional to the aspect ratio. For revolving wings about their root, detailed analysis of the flow structure revealed an overall loss of coherency of the LEV as the Rossby number increases [49, 90, 91]. Likewise, Garmann et.

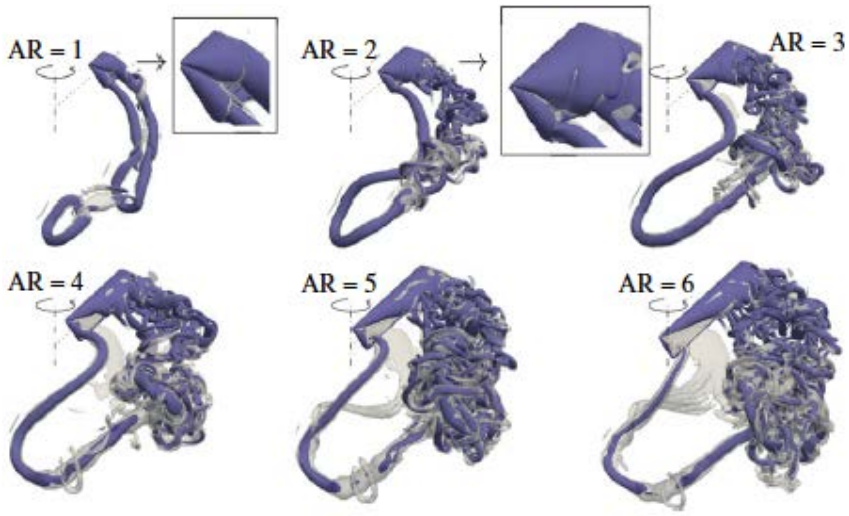

Figure 2.8: Q-criterion isosurfaces of a rotating plate for various AR.

Source: Jardin et. al. *Journal of The Royal Society Interface* **15**, (2018).

al, Harbig et al. and Carr et al. [34, 27, 15] showed for wings undergoing small amplitude revolution, that there are two different flow regions along the span of the wing. The first is an inboard region where the LEV is stable and generates high lift, and the second is an outboard region where the LEV lifts away from the surface, resulting in a local loss in flow structure.

For most of the purely revolving wing cases, spanwise flow has been claimed to be the mechanism keeping the LEV attached along the span of the wing because it is hypothesized to carry circulation out of the LEV, maintaining a bounded LEV strength and size. However, Birch and Dickinson [10] performed a study on a *Drosophila melanogaster* robotic wing that was rotated about a central axis. In this study, fences and baffles were installed along the span of the wing to impede the spanwise flow. By using digital particle

image velocimetry, it was observed that the LEV remained attached while the spanwise flow was mitigated. It was noted that the circulation of the LEV drops in most cases when the fences and baffles were installed. However, in a particular case, when a cylindrical wall was added just on the edge of the wingtip radius to avert spanwise flow from the tip vortex, the LEV's circulation increased by 14%. Showing the wing tip interaction, does indeed have destructive relationship with the LEV. Even though axial flow was not observed, a large outboard velocity was seen just behind the LEV. An attached LEV was observed, even though spanwise flow was not. It was hypothesized that the attached flow was maintained by the tip vortex inducing a downwash on the LEV, pushing the LEV into the surface. This also been observed Shyy et al [75] on a flapping flat plate (aspect ratio 4) where the tip vortex was found to create a low pressure region near the tip of the wing, in turn, anchoring the LEV.

2.3 Spanwise Flow

Under steady conditions, the effect of sweep on lift enhancement through leading-edge vortex (LEV) stabilization is well understood, particularly in the context of delta-wing aircraft, as discussed by Polhamus [66]. With increasing degrees of sweep, one finds a proportionally stronger corewise flow drawing vorticity away from the leading edge vortex, which in turn is sufficient to maintain LEV attachment.

When allowing for the possibility of spanwise vortex stabilization on rotating wings, Ellington et al. [25] were the first to observe this phenomenon for the case of a flapping model-hawkmoth wing (Re = 100). Ellington et al. postulated that spanwise flow through

the core of the vortex causing a conical spiral vortex, was responsible for the redirection of momentum toward the wing tip. This would then allow for the LEV circulation to remain indefinitely bounded, similar to the quasi-steady stabilization experienced in the delta-wing LEV arrangement. Beem et al. [8] showed that the spanwise flow in isolation was not responsible for vortex stability, which corroborated previous findings by Birch & Dickinson [10] that spanwise flow was not responsible for LEV stability on rotating wings. However, nominally two-dimensional spanwise flow, such as that investigated by Beem et al. [8], cannot result in three-dimensional effects because the convection of spanwise-oriented vorticity, depends also on a gradient of vorticity magnitude.

As the nature of LEV growth and detachment remains poorly understood, reduced-order models are currently being developed to account for LEV growth on simple geometries. These reduced-order models are often based on potential flow, such as those described by Ansari et al. [7], and Hammer [32]. Xia et al. [97] extended a discrete vortex method to include quasi-three-dimensional effects by including a potential sink to simulate spanwise flow. However, in a computational study by Garmann et al. [28] that compared LEV stability of a rotating wing to that of a plunging twisted wing, it was demonstrated that LEV stability was not an effect of a spanwise variation of effective incidence. The results of Garmann et al. [28] and Beem et al. [8] showed that neither spanwise variation in effective incidence nor uniform spanwise flow was responsible for LEV stability. Therefore, a fully three-dimensional model for LEV growth that accounts for both spanwise flow and spanwise variation in effective incidence may be required to capture the mechanism of LEV stability.

On a nominally two-dimensional geometry, spanwise flow alone is not sufficient to produce vortex stabilization. Rather there must be spanwise gradients in vorticity or spanwise flow, such that vorticity can be convected and stretched. Planforms such as delta wings drain vorticity with spanwise flow to produce a stable LEV, such as that shown by Gursul et al. [31]. However, it is not clear what specific three-dimensional features, such as wing kinematics or shape, would result in an appropriate balance of vortex convection and stretching on planforms with a spanwise variation in effective incidence, such as for a flapping wing. The question of what form of flapping-wing kinematics can result in an appropriate balance of vorticity convection and stretching ultimately motivates the development of reduced-order modeling tools, such as those described in the following section.

2.4 Vorticity Flux Analysis

With the advent of high resolution cameras and modern day scientific equipment, we have gained the ability quantify the local variables and how they affect the global flow. Vorticity transport analysis has been a tool employed, in which this gap has been filled. In the ground breaking work done by Wojcik et. al [89] they were able to quantify the sources and sinks of vorticity in a rotating blade in quiescent fluid, by using equation 2.5 and integrating around a closed loop that encases the LEV. Where the term on the LHS is the time rate of change of circulation in the control region. The first term on the RHS is the spanwise convective flux over a control region that encases the LEV, the second term is the tilting x and y, the third term is the in-plane convective flux, the annihilation term is the cross cancelation of negative sign vorticity from the opposite sign vorticity .This

study illuminated fundamental insight into the rotating plate problem. The first important finding that came from this analysis was that a diffusive flux of secondary opposite-sign vorticity from the surface of the wing was necessary, but not sufficient for LEV stability, under at least some cases of rotating wings. Spanwise flux was found to be negligible in some attached LEVs, demonstrating that it is not always necessary for LEV stability.

$$\frac{d\Gamma_z}{dz} = \int_{A_z} U_z \frac{\partial \omega_z}{\partial z} dA_z + \int_{A_z} \left(\omega_y \frac{\partial U_z}{\partial y} + \omega_x \frac{\partial U_z}{\partial x} \right) dA_z + \int_{L-y} U_x \omega_z dL - Annihilation \quad (2.5)$$

Eslam Panah et al. further expanded the vorticity flux analysis, by expanding the vorticity transport equation and computing the diffusive flux term in equation 2.6, from surface pressure measurements. By applying equation 2.6 Eslam Panah et. al were able to bring new insight to the plunging plate problem. For a rectangular plate in a pure plunge motion, during the downstroke, the surface vorticity flux due to the pressure gradient is consistently about half that due to the leading-edge shear layer for all parameter values investigated, demonstrating that production and entrainment of secondary vorticity is also an important mechanism regulating LEV strength in periodic plunging. A small but non-negligible vorticity source was also attributed to spanwise flow toward the end of the down-stroke. Aggregate vortex tilting is notably more significant for higher plunge frequencies, suggesting that the vortex core is more three-dimensional [60].

$$\frac{d\Gamma}{dt} = \int_A u_z \frac{\partial \omega_z}{\partial z} dA + \int_A \left(\omega_x \frac{\partial u_z}{\partial x} + \omega_y \frac{\partial u_z}{\partial y} \right) dA - \oint_{\partial A} (\mathbf{u} \cdot \mathbf{n}_{\partial A}) \omega_z ds + \frac{1}{\rho} \int_{bound4} \frac{\partial p}{\partial x} dx \quad (2.6)$$

when rotation was introduced to the model with a sweptback leading edge, Wong &

Rival [92] demonstrated that the 'relative' stability of the LEV (defined as the convective speed of the LEV relative to the wing) can be improved by regulating the LEV growth via the enhancement of the spanwise vorticity transport and vortex stretching, in which the latter helps to keep the vortex size under the critical length scale of one chord length, which, once breached, the vortex must inevitably separate, as suggested by Rival et al. (2014). The finding of Wong & Rival [92] reinforced the importance of rotation in the stabilization of the LEV.

More recently, Onoue et al. [58] characterized the LEV dynamics on a rapidly pitching plate over a wide range of flow conditions, and demonstrated through a vorticity transport analysis, that the LEV circulation and formation time scale uniformly with the feeding shear-layer velocity at the leading edge shown in Equation 2.7, where f , c and $\Delta\alpha$ denote pitching frequency, plate's chord length, and maximum pitching amplitude in radians, respectively. The vortex scaling proposed in Onoue et al. [58] conformed very well with the concept of optimal vortex formation number originally introduced in the seminal work of Gharib et al. [29]. This offered an appealing framework for us to think about how we can potentially control and predict the strength and formation time of the LEV.

$$U_{SL} = \frac{4fc\alpha}{2 + U_{\infty} sin(\alpha(t))} \tag{2.7}$$

The fluid dynamic field says that the prolonged attachment from a rotating wing is due to Coriolis accelerations. Jardine and David [41] have artificially tuned the Coriolis term in the Navier Stokes equation and showed that the LEV remained attached longer for a higher values. Eldredge and Jones [24] said the Coriolis is a a tilting term, which

acts similar to tilting and stretching and then combine all three of the terms into a single term called Coriolis tilting term. Garmann and Visbal [28] claimed that the Coriolis term can act as a stabilizing force if the vector is point to the surface of the wing. The one thing all these arguments have in common, is that the Coriolis accelerations stabilize the LEV. Once the Coriolis term is understood on a rolling wing in a freestream, this work will extend he knowledge of rotational augmentation. It will examine a plate that is actively pitching during a rolling maneuver in a free stream. Once the foundation is laid out for rotational augmentation, a strategy to manipulate the flow to alter aerodynamic loads and flow topology will be employed.

CHAPTER 3
VORTICITY FLUX ANALYSIS

The objective of the vorticity flux analysis is to identify the governing sources and sinks in LEV development. As the behavior of the LEV is governed by the vorticity transport equation, its integration over a control surface provides a characterization of the vorticity dynamics. The overarching goal, that comes with the vorticity transport analysis, is to identify the transport quantities that can manipulated in a meaningful way, to alter the flow dynamics in a favorable way. The control region, where the vorticity transport analysis will be conducted, is in the non-inertial reference frame, i.e wing reference frame. It is computed this way such that a measurement can be directly made from pressure taps, to capture the diffusive flux.

3.1 Derivation of Vorticity Flux Equation in a Non-Inertial Reference Frame

For a fluid with constant properties, the rate of change of circulation within a control region can be expressed as in equation 3.1 by substitution of the Navier-Stokes equation [67]:

$$\begin{aligned}\frac{\mathrm{d}\Gamma}{\mathrm{d}t} &= \oint \frac{\partial \mathbf{u}}{\partial t} \cdot \mathrm{d}\mathbf{s} \\ &= -\int_A [\nabla \times (\omega \times \mathbf{u})] \cdot \mathbf{n}_A \, \mathrm{d}A - \oint_{\partial A} \frac{\mathrm{d}p}{\rho} - \oint_{\partial A} \mathbf{a}_I \cdot \mathrm{d}\mathbf{s} + \oint_{\partial A} \nu \nabla^2 \mathbf{u} \cdot \mathrm{d}\mathbf{s}\end{aligned} \tag{3.1}$$

for the planar control region shown in figure 3.1, $\mathbf{n}_A = \mathbf{e}_z$ is the surface normal to the plane of the control region. The term on the RHS is the time rate of change of circulation, the first term on the RHS is the unsteady term, the second term is the inertial term, the third term is the pressure term, the last term is the viscous term, and $\mathbf{a}_I$ is the local acceleration

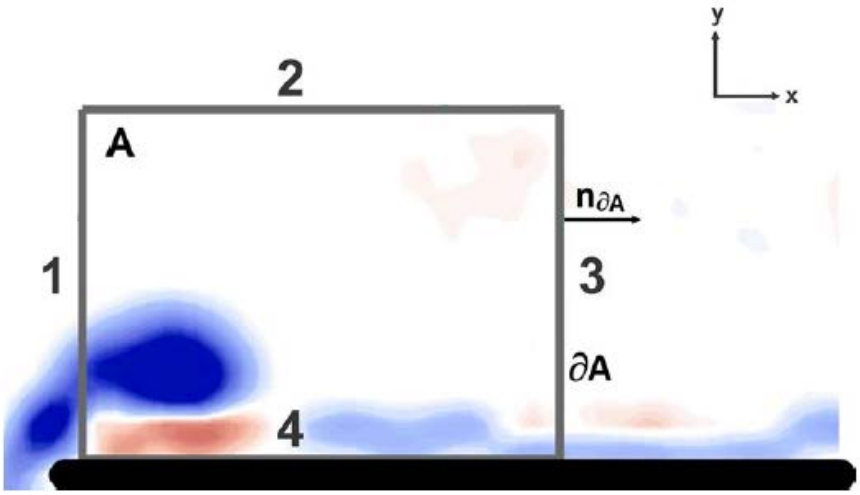

Figure 3.1: Control region where the vorticity flux analysis will be computed from. This is in the non-inertial, plate aligned coordinate system.

---

in the inertial frame, which can be written as:

$$\boldsymbol{a}_I = -2\boldsymbol{\Omega} \times \mathbf{u} - \frac{d\boldsymbol{\Omega}}{dt} \times \mathbf{r} - \boldsymbol{\Omega} \times (\boldsymbol{\Omega} \times \mathbf{r}) \,. \tag{3.2}$$

The terms on the right side of equation 3.2 are the Coriolis, angular, and centripetal accelerations, respectively.

Following Eslam Panah's derivation [61], who derived the transport equation in a non-rotating reference frame. The resulting equation that was derived, results in the vorticity transport equation shown in equation 3.3. Where the terms can be read starting on the LHS, which is the time rate of change of circulation in a defined control region. Moving to the RHS the first term is the spanwise convective flux, the second is the in-plane convective flux, the third term is the diffusive flux, the fourth term is the tilting term, and the final term is the non-inertial acceleration term. This term was zero the Eslam Panah's

work since the work was conducted on a plunging plate, which is a linear motion.

$$\begin{aligned}\frac{d\Gamma}{dt} = &-\int_{A_z}\left(u_z\frac{\partial\omega_z}{\partial z}\right)dA - \oint(\mathbf{u}\cdot\mathbf{n}_{\partial\mathbf{A}})\,\omega_z\,ds + \frac{1}{\rho}\int_{\text{bound 4}}\frac{\partial p}{\partial x}\,dx \\ &+\int_{A_z}\left(\omega_x\frac{\partial u_z}{\partial x}+\omega_y\frac{\partial u_z}{\partial y}\right)dA - \oint_{\partial A}\mathbf{a}_I\cdot\mathrm{d}\mathbf{s}\end{aligned} \tag{3.3}$$

Since linear accelerations do not affect the representation or transport of vorticity in the control region, they are not represented in equation 3.2. The terms in equation 3.2 can be expressed, for the control region of figure 3.1, in terms of rotations about the three principal axes in the non-inertial frame $(\Omega_x, \Omega_y, \Omega_z)$ and their accelerations $(\dot{\Omega}_x, \dot{\Omega}_y, \dot{\Omega}_z)$.

The angular acceleration term can be expressed in terms of the components of the rotational acceleration of the non-inertial system, $\mathbf{\Omega} = (\Omega_x, \Omega_y, \Omega_z)$:

$$-\oint_{\partial A}\mathbf{a}_{I,ang}\cdot\mathrm{d}\mathbf{s} = \oint_{\partial A}(\dot{\mathbf{\Omega}}\times\mathbf{r})\cdot\mathrm{d}\mathbf{s} \tag{3.4}$$

The centripetal acceleration can be examined by application of a vector identity to yield:

$$\begin{aligned}-\oint_{\partial A}\mathbf{a}_{I,cen}\cdot\mathrm{d}\mathbf{s} &= \oint_{\partial A}\mathbf{\Omega}\times(\mathbf{\Omega}\times\mathbf{r})\cdot\mathrm{d}\mathbf{s} \\ &= \oint_{\partial A}[\mathbf{\Omega}(\mathbf{\Omega}\cdot\mathbf{r}) - \mathbf{r}(\mathbf{\Omega}\cdot\mathbf{\Omega})]\cdot\mathrm{d}\mathbf{s}.\end{aligned} \tag{3.5}$$

Expressing equation 3.6 in Cartesian coordinates for the planar control region where $\mathrm{d}\mathbf{s} = \mathrm{d}x\hat{e}_x + \mathrm{d}y\hat{e}_y$, and expanding the scalar products yields:

$$\begin{aligned}-\oint_{\partial A}\mathbf{a}_{I,cen}\cdot\mathrm{d}\mathbf{s} = \oint_{\partial A}\Big\{&\Big[(\Omega_x r_x + \Omega_y r_y + \Omega_z r_z)\Omega_x - \Omega^2 r_x\Big]\mathrm{d}x \\ &+\Big[(\Omega_x r_x + \Omega_y r_y + \Omega_z r_z)\Omega_y - \Omega^2 r_y\Big]\mathrm{d}y\Big\}\end{aligned} \tag{3.6}$$

Applying Green's theorem to convert equation 3.6 to an area integral reveals that the centripetal acceleration makes no contribution to the rate of change of circulation within the

control region:

$$-\oint_{\partial A} \mathbf{a}_{I,cen} \cdot \mathrm{d}\mathbf{s} = \iint_A \left(\Omega_y \Omega_x - \Omega_x \Omega_y\right) \mathrm{d}x\,\mathrm{d}y = 0 \tag{3.7}$$

Evaluating the closed contour integral of the Coriolis acceleration about the control region depicted in figure 3.1 yields:

$$\begin{aligned}
-\oint_{\partial A} \mathbf{a}_{I,\mathrm{Cor}} \cdot \mathrm{d}\mathbf{s} &= -\oint_{\partial A} (2\boldsymbol{\Omega} \times \mathbf{u}) \cdot \mathrm{d}\mathbf{s} \\
&= -\oint_{\partial A} \left[\left(\Omega_y w - \Omega_z v\right)\hat{i} - \left(\Omega_x w - \Omega_z u\right)\hat{j} + \left(\Omega_x v - \Omega_y u\right)\hat{k}\right] \cdot ds \\
&= -\oint_{\partial A} \left\{2(\Omega_y u_z - \Omega_z u_y)\mathrm{d}x + 2(\Omega_z u_x - \Omega_x u_z)\mathrm{d}y\right\} \\
&= -\oint_{\partial A} 2\Omega_z(-u_y \mathrm{d}x + u_x \mathrm{d}y) - \oint_{\partial A} 2\left(\Omega_y u_z \mathrm{d}x - \Omega_x u_z \mathrm{d}y\right) \\
&= -\oint_{\partial A} 2\Omega_z(\mathbf{u} \cdot \mathbf{n})\mathrm{d}s - \oint_{\partial A} \left(\Omega_y u_z \mathrm{d}x - \Omega_x u_z \mathrm{d}y\right)
\end{aligned} \tag{3.8}$$

The first term is the integrated convective flux of apparent z-vorticity ($2\Omega_z$) due to the perceived solid body rotation of fluid within the rotating reference frame as a result of a pitch rotation (which does not exist in the present case). Thus it is a correction to the augmented ω_z measured in the rotating frame. The second term can be further manipulated, using Green's theorem:

$$-\oint_{\partial A} \left(\Omega_y u_z \mathrm{d}x - \Omega_x u_z \mathrm{d}y\right) = \iint_A \left(2\Omega_x \frac{\partial u_z}{\partial x} + 2\Omega_y \frac{\partial u_z}{\partial y}\right) \mathrm{d}A. \tag{3.9}$$

The resulting expression is identical in structure to the tilting term in equation 3.1, with the exception that the vorticity components ω_x and ω_y in equation 3.1 are replaced by the apparent vorticity components $2\Omega_x$ and $2\Omega_y$ in equation 3.9. Whereas the measured vorticity vector $\boldsymbol{\omega} = (\omega_x, \omega_y, \omega_z)$ is free to tilt, the *apparent* vorticity components, $2\Omega_x$ and $2\Omega_y$ are determined by the kinematics of the reference frame, and thus cannot provide any

real contribution to the vorticity dynamics. Thus, this apparent tilting is, as with the $2\Omega_z$ term, a correction to fictitious contributions to the tilting term of equation 3.1 manifest in the measurement of ω_x and ω_y within the rotating frame. The above equation can also derived in the similar manner:

$$\int 2\boldsymbol{\Omega} \times \mathbf{u} \cdot ds$$

$$\int \nabla \times [2\boldsymbol{\Omega} \times \mathbf{u}] \cdot \mathbf{n}_{\partial A} dA$$

$$= (\boldsymbol{u} \cdot \nabla)\boldsymbol{\Omega} + \boldsymbol{\Omega}(\nabla \cdot \boldsymbol{u}) - (\boldsymbol{\Omega} \cdot \nabla)\boldsymbol{u} - \boldsymbol{u}(\nabla \cdot \boldsymbol{\Omega}) \tag{3.10}$$

$$= \left(\boldsymbol{u}\frac{\partial}{\partial x} + \boldsymbol{v}\frac{\partial}{\partial y} + \boldsymbol{w}\frac{\partial}{\partial z}\right)\boldsymbol{\Omega} - \left(\boldsymbol{\Omega}_x\frac{\partial}{\partial x} + \boldsymbol{\Omega}_y\frac{\partial}{\partial y} + \boldsymbol{\Omega}_z\frac{\partial}{\partial z}\right)\boldsymbol{u} \tag{3.11}$$

$$+ \boldsymbol{\Omega}\left(\frac{\partial u}{\partial x} + \frac{\partial v}{\partial y} + \frac{\partial w}{\partial z}\right) - \boldsymbol{u}\left(\frac{\partial}{\partial x}\boldsymbol{\Omega}_x + \frac{\partial}{\partial y}\boldsymbol{\Omega}_y + \frac{\partial}{\partial z}\boldsymbol{\Omega}_z\right)$$

$$= 2\int_A \left(\boldsymbol{\Omega}_x\frac{\partial w}{\partial x} + \boldsymbol{\Omega}_y\frac{\partial w}{\partial y} + \boldsymbol{\Omega}_z\frac{\partial w}{\partial z}\right) \cdot \hat{n} d\boldsymbol{A} \tag{3.12}$$

Combining all the terms, and assuming we only have pitch (Ω_x) and roll (Ω_z), gives the following equation for a pitching and rolling plate.

$$\boxed{\begin{aligned}\frac{d\Gamma}{dt} = \int_A \left(\omega_x\frac{\partial u_z}{\partial x} + \omega_y\frac{\partial u_z}{\partial y} - u_z\frac{\partial \omega_z}{\partial z}\right)dA - \oint (\mathbf{u} \cdot \mathbf{n}_{\partial \mathbf{A}})\,\omega_z ds + \frac{1}{\rho}\int_{\text{bound 4}} \frac{\partial p}{\partial x}dx \\ -2\oint_{\partial A} \Omega_z\,(\mathbf{u} \cdot \mathbf{n}_{\partial \mathbf{A}})\,ds + 2\oint_{\partial A} \Omega_x w \cdot ds + \oint_{\partial A} \left[\dot{\Omega}_z r_y dx + \dot{\Omega}_z r_x d_y\right] dA\end{aligned}} \tag{3.13}$$

In the results section, pure roll is considered. This gives the equation that will be used for this work as:

$$\frac{d\Gamma}{dt} = \int_A \left(\omega_x \frac{\partial u_z}{\partial x} + \omega_y \frac{\partial u_z}{\partial y} - u_z \frac{\partial \omega_z}{\partial z} \right) dA - \oint (\mathbf{u} \cdot \mathbf{n}_{\partial \mathbf{A}})\, \omega_z ds + \frac{1}{\rho} \int_{\text{bound 4}} \frac{\partial p}{\partial x} dx + 2 \oint_{\partial A} \left(\Omega_y u_z \mathrm{d}x - \Omega_x u_z \mathrm{d}y \right) \tag{3.14}$$

This gives the terms on the right hand side, first integrand is the out-of-plane fluxes, tilting and spanwise convective. The second integrand is the shear layer flux. The third integrand is the diffusive flux and the last integrand is the Coriolis flux due to the rolling motion.

3.2 Diffusive Flux of Vorticity

While most of the terms within Equation 3.13 are in their final form, the term that accounts for the diffusion of vorticity from the surface of the airfoil in Equation 3.13 needs some additional modification. In order to quantify the diffusive flux in its current form, the gradient of the vorticity field at the surface of the airfoil would need to be measured. This would require the velocity field near the surface of the airfoil to be very accurately resolved. This was achieved within the works of both Shih and Ho [73] and Kuo and Hsieh [47] through the use of Laser Doppler Anemometry (LDA). Particle Image Velocimetry (PIV) will be used within the current work, and while this will allow for the characterization of the entire velocity field above the surface of the airfoil, laser reflections will decrease the accuracy of measurements made near the surface of the airfoil. Furthermore, particle seeding considerations will limit the resolution at which the velocity field can be specified. It is therefore desirable to modify the final term on the RHS of Equation 3.13 so that it can be characterized without the use of the near-wall velocity field.

Lighthill [51] tells us that all the vorticity within a barotropic flow must be gener-

ated on a solid boundary, as the no-slip condition allows forces within the flow to impose a rotation on wall-bounded fluid elements. The term expressed within Equation 3.13 essentially characterizes how much vorticity is diffused into the flow after this on-wall generation occurs. It is therefore possible to derive an alternate form for this diffusive flux term by identifying the specific vorticity generation mechanisms that are present at the wall.

All of the subsequent derivations have been adapted from the works of Wu et al. [94, 93, 36], who pioneered the development of an equation that fully characterizes the vorticity generation mechanisms of any arbitrary fluid-structure interface. The exception to this, is the rotational accelerations, which were derived for the Vorticity Transport equation. While the following derivation follows the same approach used by Wu et al. [94, 93], the current analysis assumptions and simplifications in order to present a concise characterization of the physics relevant to the types of fluid-structure interactions that are considered within this manuscript. In the quest to find the what effect pressure gradients had on the surface of the plate, Wu and Wu started with the Navier stokes equation's and found the relation shown in equation 3.15

$$\vec{a} + \frac{\nabla p}{\rho} + \nu \nabla \times \vec{\omega} = 0 \tag{3.15}$$

Where $\vec{a}$ is equal to,

$$\vec{a} = -\dot{\mathbf{\Omega}} \times \boldsymbol{r} - \mathbf{\Omega} \times (\mathbf{\Omega} \times \mathbf{r}) - 2\mathbf{\Omega} \times \mathbf{u} \tag{3.16}$$

The first term in equation 3.16 is the angular acceleration, the second term centripetal acceleration and the third is the Coriolis acceleration. Carrying out the cross product yields,

$$-\dot{\boldsymbol{\Omega}} \times \boldsymbol{r} = \left(\dot{\boldsymbol{\Omega}}_z r_y - \dot{\boldsymbol{\Omega}}_y r_z\right)\hat{x} + \left(\dot{\boldsymbol{\Omega}}_x r_z - \dot{\boldsymbol{\Omega}}_z r_y\right)\hat{y} + \left(\dot{\boldsymbol{\Omega}}_y r_x - \dot{\boldsymbol{\Omega}}_x r_y\right)\hat{z} \tag{3.17a}$$

$$-\boldsymbol{\Omega} \times (\boldsymbol{\Omega} \times \boldsymbol{r}) = 0 \tag{3.17b}$$

$$-2\boldsymbol{\Omega} \times \boldsymbol{u} = 2\left[\left(\boldsymbol{\Omega}_z \boldsymbol{u}_y - \boldsymbol{\Omega}_y \boldsymbol{u}_z\right)\hat{x} + \left(\boldsymbol{\Omega}_x \boldsymbol{u}_z - \boldsymbol{\Omega}_z \boldsymbol{u}_x\right)\hat{y} + \left(\boldsymbol{\Omega}_y \boldsymbol{u}_x - \boldsymbol{\Omega}_x \boldsymbol{u}_y\right)\hat{z}\right] \tag{3.17c}$$

As defined by Wu and Wu [94]–and illustrated within Figure 3.2–vorticity is generated at the surface of the airfoil when a force is applied to a surface-bound fluid element so that the principal axes of its strain-rate tensor is rotated out of the wall-normal direction. This definition was posed after Wu and Wu [94] claimed that the no-slip condition prevents a wall-bound fluid element from rotating, and that a vorticity-containing fluid element only develops an angular velocity after it has been diffused into the flow. Thus, the "rotation of the principle axis of the strain-rate tensor" was used to characterize a way for a wall-bound fluid elements to contain vorticity without actually rotating. While it is worth considering, this detailed description is not particularly relevant to vortex generation, and a majority of studies are content with characterizing the process as if the wall-bound fluid element were actually allowed to rotate [51, 55, 95, 11].

Consider the arbitrary solid surface S shown in Figure 3.3 that has the surface-normal unit vector $\hat{y}$ and surface-tangent unit vectors $\hat{x}$ and $\hat{z}$, which are defined such that $\hat{z} = \hat{x} \times \hat{y}$. Note that all subsequent derivation within this section will utilize this coordinate system shown in figure 3.3. However, $\hat{z}$ can be specified in the spanwise direction, so that this analysis is consistent in the previous section (section 3.1) for the generation of ω_z, but this time at the surface boundary.

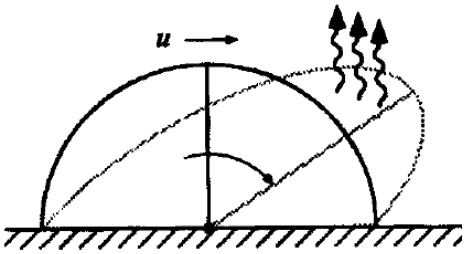

Figure 3.2: Schematic depicting the generation of vorticity via the deformation of a wall-bound fluid element. Adopted from Wu and Wu [94].

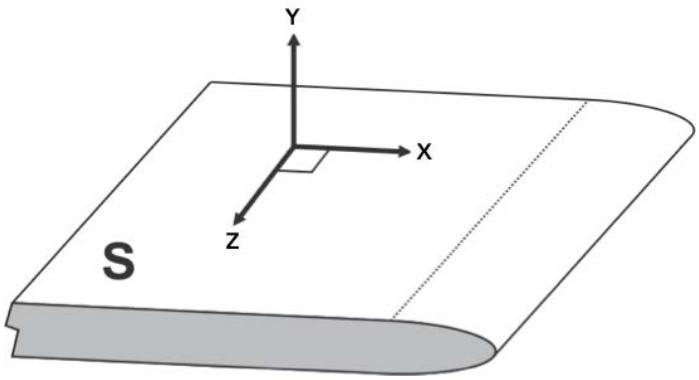

Figure 3.3: Coordinate system of an arbitrary solid surface S upon which vorticity is generated.

The generation of vorticity on surface S can be quantified by taking the cross product of the surface-normal unit vector ($\hat{y}$) and Equation 3.15, the result of which is shown in Equation 3.18.

$$(\hat{y}\times\vec{a}) + (\hat{y}\times\frac{\nabla p}{\rho}) + \nu(\hat{y}\times(\nabla\times\vec{\omega})) = \left(a_z + \frac{1}{\rho}\frac{\partial p}{\partial z} + \nu\left(\frac{\partial \omega_y}{\partial x} - \frac{\partial \omega_x}{\partial y}\right)\right)\hat{x} + \left(a_x - \frac{1}{\rho}\frac{\partial p}{\partial t} + \nu\left(\frac{\partial \omega_y}{\partial z} - \frac{\partial \omega_z}{\partial y}\right)\right)\hat{z} \quad (3.18)$$

where a_x, a_y and a_z are the $\vec{x}$, $\vec{y}$ and $\vec{z}$ components of $\vec{a}$,which are in the chordwise, surface normal and spanwise directions, respectively. The objective of the current analysis is to quantify the diffusion of the spanwise component of vorticity from the surface of the airfoil, for a non-inertial reference frame, and will therefore only utilize the z-component that is defined in Equation 3.18. Substituting the values in for $\vec{a}$ in equation 3.18 and then only using $\hat{z}$ results in equation 3.19.

$$0 = -\Omega_z u_y - \frac{1}{\rho}\frac{\partial p}{\partial x} + \nu\left(\frac{\partial \omega_y}{\partial z} - \frac{\partial \omega_z}{\partial y}\right) \quad (3.19)$$

Where the $\Omega_z u_y$ is the only contributing factor from the acceleration term, more specifically this originates from the Coriolis acceleration. Equation 3.19 can then be rearranged to provide an expansion for the wall-normal gradient of ω_z, which represents the diffusive flux of spanwise vorticity from the surface.

$$\nu\frac{\partial \omega_z}{\partial n} = -\Omega_z u_y - \frac{1}{\rho}\frac{\partial p}{\partial x} + \nu\frac{\partial \omega_y}{\partial z} \quad (3.20)$$

The first two terms of the RHS of equation 3.20 represent vorticity generated by the chordwise component of the wall acceleration and the chordwise gradient of the distribution of surface pressure. The mechanism that are associated with the third term of the

RHS in equation 3.20 are not as apparent, as the previous two terms. This term has been associated with vorticity generation mechanisms that occur on curved surfaces [94, 5]. For all experiments considered in this manuscript, a flat-plate with a uniform span will be used, this means that both the spanwise gradients of ω_y and ω_x will be zero. It is also important to note that in order for this simplification to be valid, any point of the airfoil's surface where the diffusive flux of vorticity in considered must have zero curvature.

Equation 3.20 can be reduced further, since pressure measurements are being made directly on the surface of the plate, it can be assumed the u_y is zero. There will be no flow passing through either side of the plate. Thus equation 3.20 can be rewritten as:

$$\nu \frac{\partial \omega_z}{\partial y} = -\frac{1}{\rho}\frac{\partial p}{\partial x} \tag{3.21}$$

The only aposite generation mechanism, Figure 3.4 presents a schematic from Wu et al. [95] to show how a surface pressure gradient leads to the generation of vorticity. The figure illustrates how a wall-bound fluid element exposed to a pressure gradient will experience a force that is directed opposite the pressure gradient. Since the fluid-element remains stationary at the surface of the airfoil due to the no-slip condition, this force will impose a torque on the element that results in the generation of vorticity that can then diffuse into the flow.

While deriving Equation 3.21 has helped resolve the physics associated with the diffusive flux of vorticity acting at the surface of a rotating airfoil, this parallel will also help with the implementation of the vorticity flux analysis. As stated at the beginning of this section, it is very difficult to quantify ω_z at the surface of the airfoil based on the non-obtrusive measurements such as PIV data, which is used in this work. However, Equation

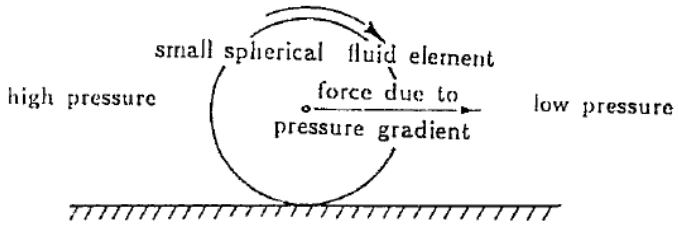

Figure 3.4: Schematic depicting the generation of vorticity via a surface pressure gradient. Adopted from Wu et al. [95].

3.21 gives a means to measure the surface gradients, by using pressure gradients on the surface. Equation 3.21 will be used to calculate transient pressure data which were obtained.

CHAPTER 4
METHODOLOGY

4.1 Overview

Four distinct experiments are considered within this dissertation, all of which are conducted with an aspect ratio (AR) two flat plate, with a chord length c =76.3 *mm*, span b =152.6*mm*, and a with a thickness of 3.3% with both leading and trailing edges were rounded with a constant half radius of the thickness of the plate. A chord based Reynolds number (Re) of 10,000 is used for all experiments. The first experiment was a wing fixed to a geometric angle of attack and then rolled. The next experiment was a wing articulated in pure pitch about its leading edge. This experiment was then followed by a wing articulated in roll, and while rolling the pitch motion was articulated. This gave the kinematics of a simultaneous pitching and rolling wing. The final experiment, the wing articulated in roll, but this time a passive bleed hole was introduced to alter the flow evolution. A more detailed explanation is given in the following sections

4.2 Experimental Setup

4.2.1 Model Geometry

The four cases to be considered employed a flat-plate wing, with an aspect ratio of two. The flat-plate wing was manufactured from acrylic to minimize laser reflections, and had a chord length, c = 76.3 mm , span b= 152.6, and thickness of 3.3% (figure 4.1) of the chord, with both the leading and trailing edges rounded with a constant radius of half the plate thickness. To ensure negligible deflection, the root of the wing was inserted into

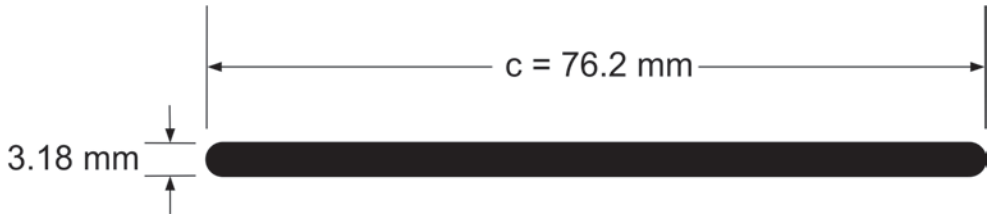

Figure 4.1: Wing geometry used in experiments.

a bracket extending the full chord length, and supported by a 3.175 mm diameter rod at the leading edge. Figure 4.2a illustrates the motion mechanism and wing, its important to note the wing is not surface piercing, but is shown in that manner to highlight where the wing is located in reference to the motors. The wing was articulated in a roll maneuver about an axis aligned with the free stream, and coincident with the surface of a skim plate extending approximately 0.45 m upstream and 0.78 m downstream of the wing mid-chord. The motion was achieved using an Emerson XVM-8020-TONS-000 DC servo motor driven by an Emerson EP-204B servo drive and Galil DMC-4040 motion controller. A second servo motor, Emerson Control Techniques XVM-6011-TONS capable of articulating the wing in a pitching mameuver.

The motor was programmed and operated using a Galil DMC-4040 motion control system. The airfoil's position was measured using the optical encoder which has 2048 counts per revolution, which is installed on the motor. Experiments were conducted in the University of Iowa's free-surface water channel with test section width of 0.61 m, and water depth of 0.33 m. The water channel has flow conditioning consisting of an 8:1 contraction ratio, honeycomb, and five screens to maintain free stream turbulence intensity

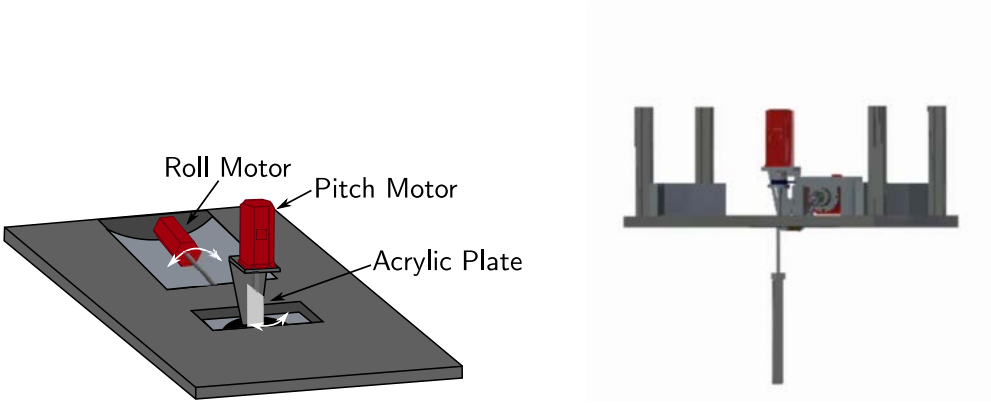

(a) Top view (b) Front view

Figure 4.2: Experimental Arrangement of pitching and rolling mechanism.

below 0.3%. Free-stream velocity is held constant for all experiments, producing a chord-based Reynolds number of Re_c = 10,000.

4.2.2 Plenoptic Particle Image Velocimetry

In order to characterize the flow field and apply the vorticity flux equation 3.13 that has been developed, a three dimensional characterization of the flow field need to be carried out. To capture the three-dimensional flow field, a plenoptic camera using light field technology was used in collaboration with Kyle Johnson and Prof. Brian Thurow of Auburn University. Kyle Johnson came to university of Iowa with the plenoptic camera to collect volumetric data, and then analyzed the data at Auburn University. Three-dimensional velocity measurements were made using plenoptic PIV, which utilizes a light-field, or plenoptic, camera, that was developed by Dr. Thurow's group. Through the addition of a microlens array in between the main lens and the image sensor a plenoptic camera gathers both spatial and angular information of a scene. The information stored in a plenoptic

image can be used to shift the perspective of the scene, change the focal plane, or, most notably, reconstruct a volume.

Ensemble-averaged measurements were obtained at multiple angles. In order to simplify the imaging configuration, the wing was imaged with the spanwise axis in the vertical orientation for each case, requiring that the initial roll position of the plate was varied for each measurement angle. In the present study, a modified 29 megapixel Imperx Bobcat B6620 was used to record plenoptic particle images. The flow was illuminated using a 200 mJ/pulse dual-cavity Nd:YAG laser, which entered the water channel from the side and at an angle in the x-y plane. The beam was spread into a volume using a spherical lens and a cylindrical lens. The arrangement can be seen in Figure 4.3. The coordinate system for the measurement volume is defined as follows: +x is along the chord originating at the leading edge, +y is normal to the plate surface originating at the plate surface, +z is along the span towards the tip and originating at the root. Nearly the entire span of the wing was studied using 3 distinct measurement volumes, each centered at 20, 55, and 89 percent span, respectively. These planes are the nominal focal planes for each individual measurement volume. Each laser volume was masked in the z direction before entering the water tunnel to extend ±30 mm from the nominal focal plane of and was clipped by the field of the view of the camera in the x and y directions, resulting in a volume with dimensions of 102 mm × 68 mm × 68 mm in x, y, and z, respectively. A raw plenoptic particle image, Figure 4.4, shows the location of the plate and leading edge. In the detail region, the hexagonal pattern of micro-images formed by each of the microlenses is shown. To properly remove the reflections from the plate, the background was subtracted using the

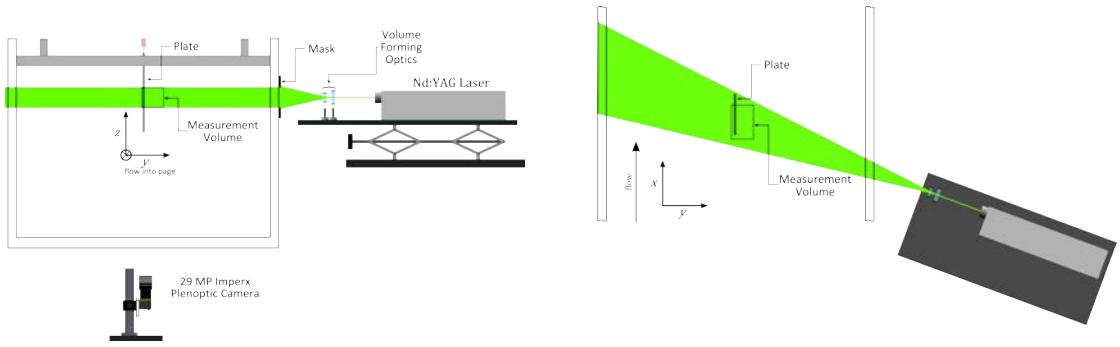

(a) side view (b) top view

Figure 4.3: Experimental Arrangement, Kyle Johnson JFM *In progress*

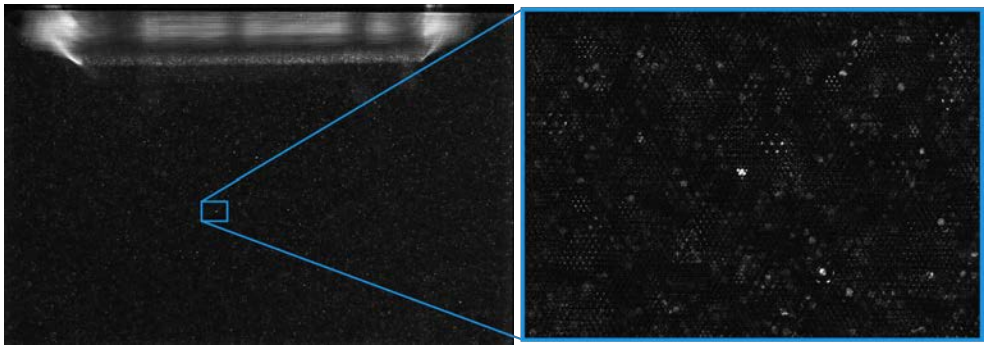

Figure 4.4: A raw plenoptic particle image, Kyle Johnson JFM *In progress*.

proper orthogonal decomposition (POD). To capture the entire plate and flowfield, three laser slabs were used with 5 mm of overlap for each region. Figure 4.5 highlights the three slabs and over lap per slab. This image also shows the plate aligned coordinate system.

Using 3 iterations of MART and a relaxation parameter $\mu = 1.0$ particle volumes were reconstructed onto a discretized grid of 527 voxels $\times$ 357 voxels $\times$ 357 voxels. An in-house 3D cross-correlation algorithm was used with 4 passes of decreasing correlation volumes (64 , 48, 32, 16, 16 voxels and 50% overlap) to produce vector fields of 63 vectors

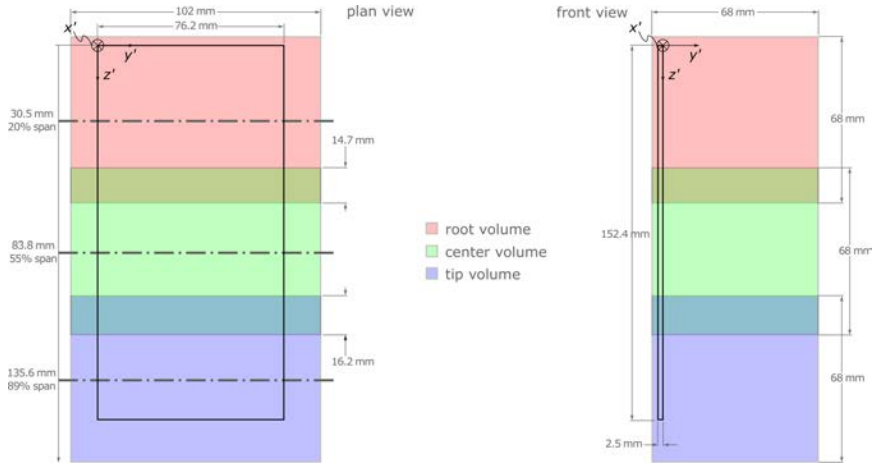

Figure 4.5: Laser slab definition and non-inertial coordinate system, Kyle Johnson JFM *In progress*.

× 42 vectors × 42 vectors. The final correlation volume had physical dimensions of 3.3 mm × 3.2 mm × 3.2 mm yielding a vector spacing of 1.6 mm in all directions. Each vector field was then interpolated onto a grid such that the previously defined origin was located at the leading edge of the plate. In each instantaneous volume, this point was manually selected by inspecting the particle image pairs. This insured that flow phenomena, such as the leading edge vortex, would not be diminished because of misalignment in the ensemble-averaged results.

4.2.3 Stereoscopic Particle Image Velocimetry

The three-dimensional velocity field of the pure pitching cases was characterized using a LaVision Flowmaster Stereo PIV system, a similar setup to the plenoptic PIV which is depicted within Figure 4.6 was used. In order to allow for the characterization of spanwise gradients within the velocity and vorticity fields, measurements were taken at

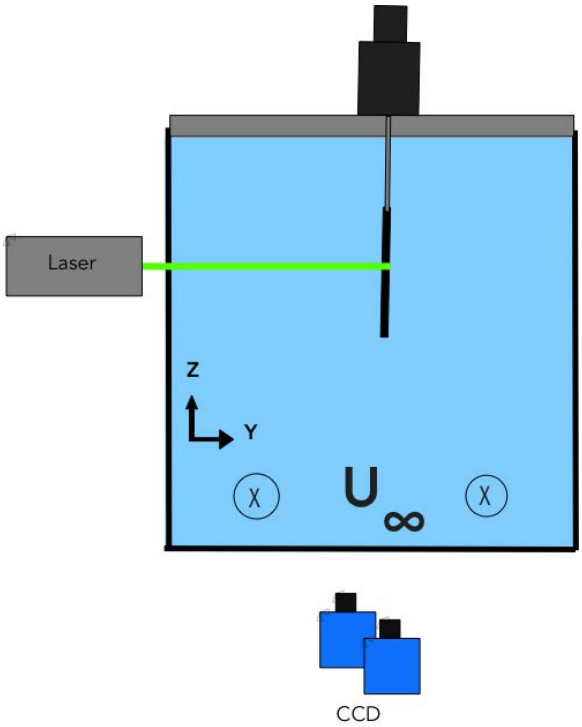

Figure 4.6: Schematic of the SPIV setup.

three spanwise planes, spaced 3.2 mm apart. A central difference approximation using the upper and lower planes could then be used to calculate the relevant spanwise gradients of the velocity and vorticity fields.

The first step in performing the PIV measurements was to seed the water channel with hollow glass spheres that had a mean diameter of 10 μm and a density of 1.1 g/cc. Stereo PIV data were acquired at a given spanwise location by using a dual-cavity 200 mJ/pulse Nd:YAG laser (Figure 4.7) with light sheet optics to illuminate the particles within the imaging plane. Images were acquired using two 14-bit Imager ProX CCD cameras with 2048×2048 pixel resolution and 14-bit dynamic range, equipped with Scheimpflug mounts and Nikon 50 mm lenses (Figure 4.8) with f-stops set to 8.0. The cameras were placed 42

Figure 4.7: Nd:YAG laser used for PIV measurements.

Figure 4.8: Imager ProX CCD cameras used for PIV measurements.

degrees to each other, with each camera being tilted 21 degrees from the vertical.

A Berkley Nucleonics Multi-Trigger Delay Generator, Model 725 was employed to trigger the motor motion and trigger the PIV system. A master signal was used was by created using an Keysight InfiniiVision 1000 X-Series Oscilloscopes, which was wired into the Berkley box. The Berkely box outputted two signals, one sent a TTL trigger pules to the Galil motion control to start the motion, then a delay was programmed and the other

sent a TTL signal to the LaVision PTU to trigger the cameras and laser. Data was collected every five degrees from 5°-40°, over one hundred cycles. Stereo PIV data were processed using LaVision DaVis 8.1.6 software and GPU to perform an adaptive multi-pass direct-correlation analysis. The first pass had an interrogation window size of 48×48 pixels and the next two had a window sizes of 24×24, all of which used 50% overlap and median filter between passes. While the PIV images were pre-processed using a particle intensity normalization (with scale of 5 pixels), the vector fields obtained by the direct-correlation analysis were not post-processed.

4.2.4 Volumetric Particle Tracking Velocimetry

Three-dimensional velocity measurements were also made, for the passive-bleed case, using three-dimensional particle tracking velocimetry. The Lavision Minishaker L, 4-camera imaging module, was used to acquire time-resolved, volumetric data. Each Minishaker camera has a resolution of 1984 x 1264 pixels and 10 bits of intensity depth, and was fit with a 12 mm lens set to $f/4$. The flow was illuminated using a Lavision LED Flashlight 300 pulsed LED bank. Lavision Davis 10.0.5 was used to process the image data using the Shake the Box algorithm [71]. The camera and lighting configuration are shown in Figure 4.9. In this case, the camera was mounted on the side of the channel, with illumination from below to provide improved overlap of the camera fields of view, and to optimize optical access to the flow field during the sweep, since time-resolved data were required for the PTV analysis. Images were captured continuously during the wing rolling motion at a frame rate of 150 Hz, and analyzed over a 160 mm x 229 mm x 200 mm

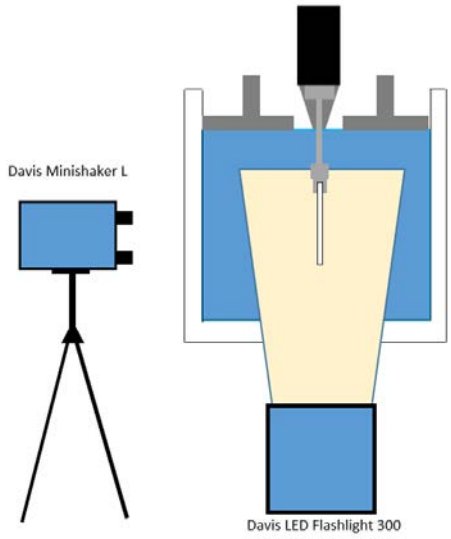

Figure 4.9: Particle Tracking Velocimetry Setup.

volume, corresponding to a region of 911 x 1301 x 1135 voxels.

Image data were pre-processed to reduce background noise by applying a 3x3 Gaussian smoothing filter. The particle tracking algorithm implemented a 2D particle detection threshold of 30 counts with a triangulation error of 1 voxel. Furthermore, particles that were within 1 voxel of another particle were removed. During the time-marching shaking process, particles were identified when appearing for a minimum of 4 time steps. Ensemble averages of 80 wing sweeps were constructed after interpolating instantaneous particle vectors onto a uniform Cartesian grid, using an interrogation subvolume of 64 voxels with an overlap of 16 voxels. A particle track conversion to velocity was done with a second order polynomial fit over 5 time step moving averages.

4.2.5 Pressure Measurements

Transient surface pressure measurements were acquired on the plunging flat-plate airfoils in order to obtain the pressure-gradient-driven diffusive boundary vorticity flux from the airfoil surface. Holes of diameter 0.0625 inches were drilled in the airfoil at the spanwise-centerline to be used for pressure taps, to calculate the diffusive flux. The first hole was 3.25 mm downstream of the leading edge, the second hole was located 65 downstream of the leading edge. These two holes were located at boundaries one and three of the control region. It was critical to capture the dynamics of the diffusive flux to close the vorticity budget. When a hole was not being used, it was sealed with modeling clay, which was pressed flush to the airfoil surface using a razor blade. In order to take pressure measurements from any given position, a barbed hypodermic tube was pressed into the appropriate hole. An 5.75 inch long piece of tygon tubing (0.0625 inch inner diameter and 0.125 inch outer diameter) was used to connect the tubulation to the Kistler pressure transducer. This tygon tubing was secured flush to the airfoil surface so as to minimize any effects on the surrounding flow, as shown in Figure 4.10.

The pressure transducer which was used to collect the pressure data was, a Kistler 4264A piezoresitive, unidirectional differential pressure transducer with a range of 104 Pa and overall uncertainty of 0.2% full scale was used for pressure measurements. The stated uncertainties were reported by the manufacturer and include errors due to non-linearity, hysteresis, and repeatability. A Kistler 4264A piezoresistive, unidirectional differential pressure transducer with a range of 10.3 kPa and overall uncertainty of 0.1% full scale was used for pressure measurements. The stated uncertainties were reported by the man-

Figure 4.10: Tygon tube connecting to a tabulation to gather pressure data, [61].

ufacturer and include errors due to non-linearity, hysteresis, and repeatability, the total uncertainty of which has been conservatively calculated as $\sigma_{Cp} = 0.1003$.

Pressure transducer output was acquired and stored using a National Instruments USB-6216 16-input, 16-bit, 400kS/s DAQ board and LabVIEW software running on a PC. For each pressure tap being measured, data for 125 oscillation cycles was obtained and then phase-averaged to obtain the final results, at 4 kHz. Static pressure transducer calibration was achieved using a Rouse manometer as the standard.

CHAPTER 5
A WING IN PURE ROLL

In this chapter four different cases of a wing in pure roll will be examined. This will set-up the framework for subsequent templates and will give insight into the transport mechanism driving a purely rotating wing, while varying the Rossby number and the advance coefficient.

5.1 Flow Structure of a Wing in Pure Roll

5.1.1 Flow Structure

Figure 5.2 shows the evolution of the LEV for all four cases. Plenoptic PIV data were acquired over the entire span for the $J_{3.25} = 0.54$ case, and subsets of the span for the others. Table 5.1 summarizes all cases that were considered within this paper. The top row in table 5.1 is referred to as the baseline case.

Both of the $J = 0.54$ cases ($R_g/c = 3.25, 2.5$) exhibit a conical LEV on the inboard region of the wing. Furthermore, for the baseline case ($J_{3.25} = 0.54$) three distinct behaviors can be observed across the span, as shown in figure 5.1a. In Region 1 ($z/b < 0.4$), the LEV is *attached*, and essentially stationary on the wing for the duration of the starting roll maneuver. In Region 2 ($0.4 < a/b < 0.75$), the LEV separates from the wing, forming a large arch structure, followed by the creation of a second vortex structure to form a dual vortex system, as observed by [12]. In Region 3 ($z/b > 0.75$), tip effects dominate. A large tip vortex is formed, and the arch structure appears to be confined by the boundary between Regions 2 and 3.

J	R_g/c	Name
0.54	3.25	$J_{3.25} = 0.54$
0.54	2.5	$J_{2.5} = 0.54$
1.36	3.25	$J_{3.25} = 1.36$
1.36	2.5	$J_{2.5} = 1.36$

Table 5.1: All the cases that were considered, within this paper. The naming convention that will be used hereafter, is denoted in the last column.

For the cases with $R_g/c = 2.5$ (figures 5.2f through 5.2j and 5.2p through 5.2t), data were acquired only along the central region of the wing $0.35 \leq z/b \leq 0.75$ In the $J_{2.5} = 0.54$ case, it is evident that the LEV remains stationary at the inboard extent of the measurement domain, suggesting, again, a conical vortex structure in the inner region. However, unlike the $J_{3.25} = 0.54$ case, the LEV structure appears to evolve smoothly across the measurement domain as, by $\phi = 30°$, it appears to be lifting into an arch in the outer region of the wing.

At $\phi = 12°$ the $J = 1.36$ cases exhibit structures similar to the $J = 0.54$ cases at later times in their evolution. The measured flow structure for $J_{3.25} = 1.36$ in figure 5.2k exhibits strong similarities to the $J_{3.25} = 0.54$ case at $\phi = 21°$ (figure 5.2c). Similarly, the central region of the $J_{2.5} = 1.36$ case visible in figure 5.2p bears a strong resemblance to the $J_{2.5} = 0.54$ case at $\phi = 21°$.

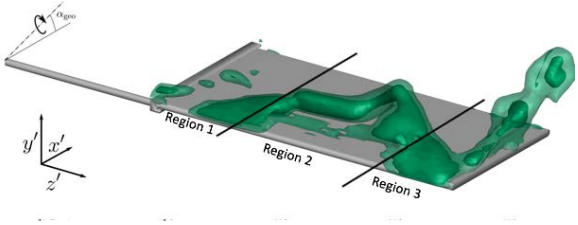

(a)

Figure 5.1: Three distinct topological regions shown in the baseline case.

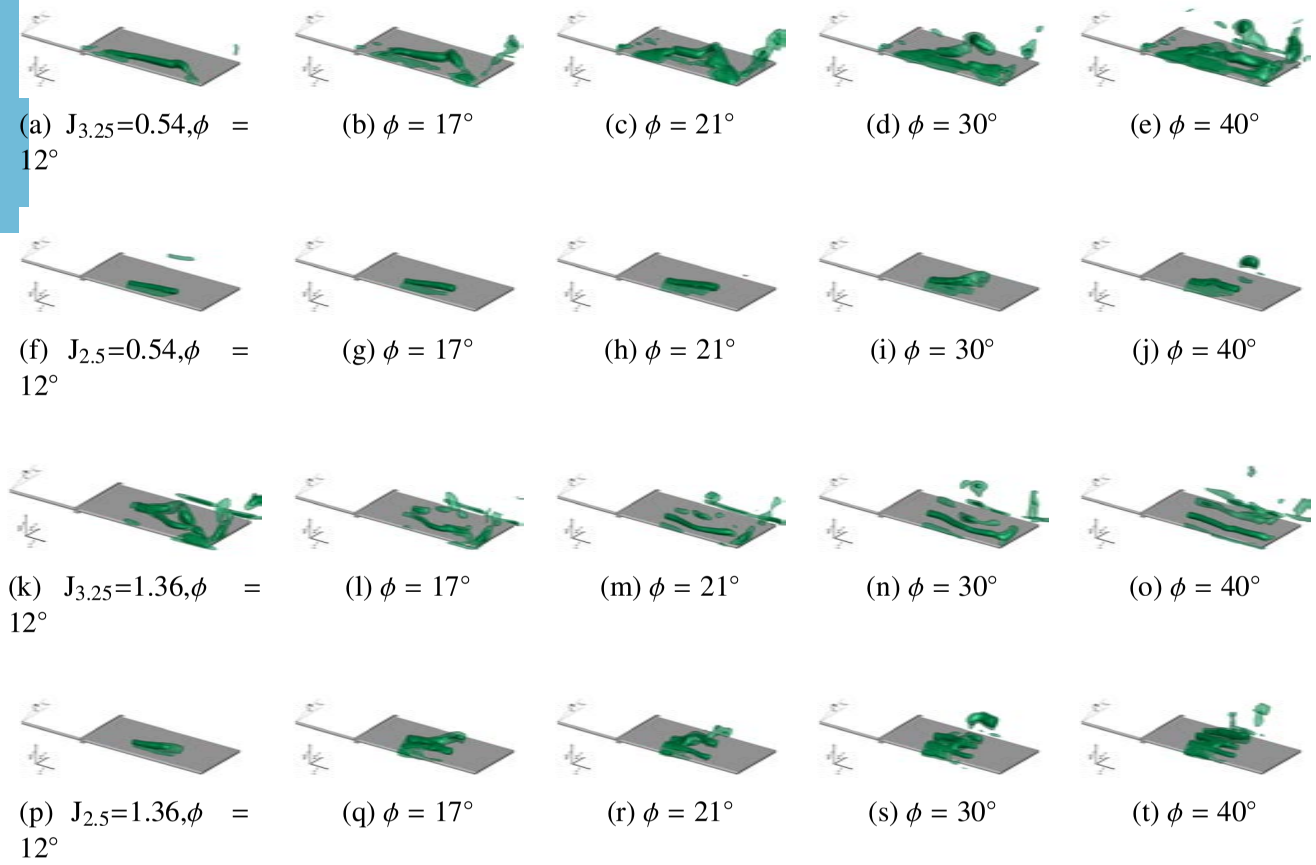

(a) $J_{3.25}$=0.54,ϕ = 12° (b) ϕ = 17° (c) ϕ = 21° (d) ϕ = 30° (e) ϕ = 40°

(f) $J_{2.5}$=0.54,ϕ = 12° (g) ϕ = 17° (h) ϕ = 21° (i) ϕ = 30° (j) ϕ = 40°

(k) $J_{3.25}$=1.36,ϕ = 12° (l) ϕ = 17° (m) ϕ = 21° (n) ϕ = 30° (o) ϕ = 40°

(p) $J_{2.5}$=1.36,ϕ = 12° (q) ϕ = 17° (r) ϕ = 21° (s) ϕ = 30° (t) ϕ = 40°

Figure 5.2: LEV formation shown with isosurfaces of normalized swirling strength, for J=0.54, J=1.36, α_{eff} = 35° for R_g/c=3.25 and 2.5.

5.1.2 Circulation Distributions

Figure 5.3 shows the variation in LEV circulation -measured within the control region illustrated in figure 3.1 for the four rolling wing cases. For the baseline case ($J_{3.25} = 0.54$), the circulation within Region 1 grows throughout the stroke (figure 5.3a). A sharp transition in circulation is observed at the boundary between Regions 1 and 2. In Region 2, the maximum circulation observed is approximately double that in Region 1, and exhibits two notable peaks at approximately $\phi = 21°$ and 30°, associated with the development of the first and second vortices in the dual vortex system. In contrast, in Region 3, the circulation remains relatively constant after approximately $\phi = 25°$. Comparing the baseline case to the $J_{2.5} = 0.54$ case (figure 5.3b), it is evident that the circulation growth is more uniform in time for the case with the smaller radius of gyration.

For the advance ratio $J = 1.36$ the circulation distribution is being aliased since there are multiple shedding events during the motion, but only finite realizations of the flow field itself. For the smaller R_g/c case, $R_g/c = 2.5$ there is an increase of circulation through the motion and then a subsequent dip in circulation, near $\phi = 40°$, which is due to an instance where a shedding event occurred and was captured during one of the realizations. When comparing the $R_g/c = 3.25$ case the to the $R_g/c = 2.5$, the larger R_g/c has larger circulation values.

5.1.3 Circulation Budget Closure and Non-inertial Contributions

Closure of the circulation budget implies equality between the left and right sides of equation 3.13. Each of the terms can be approximated by numerical integration using

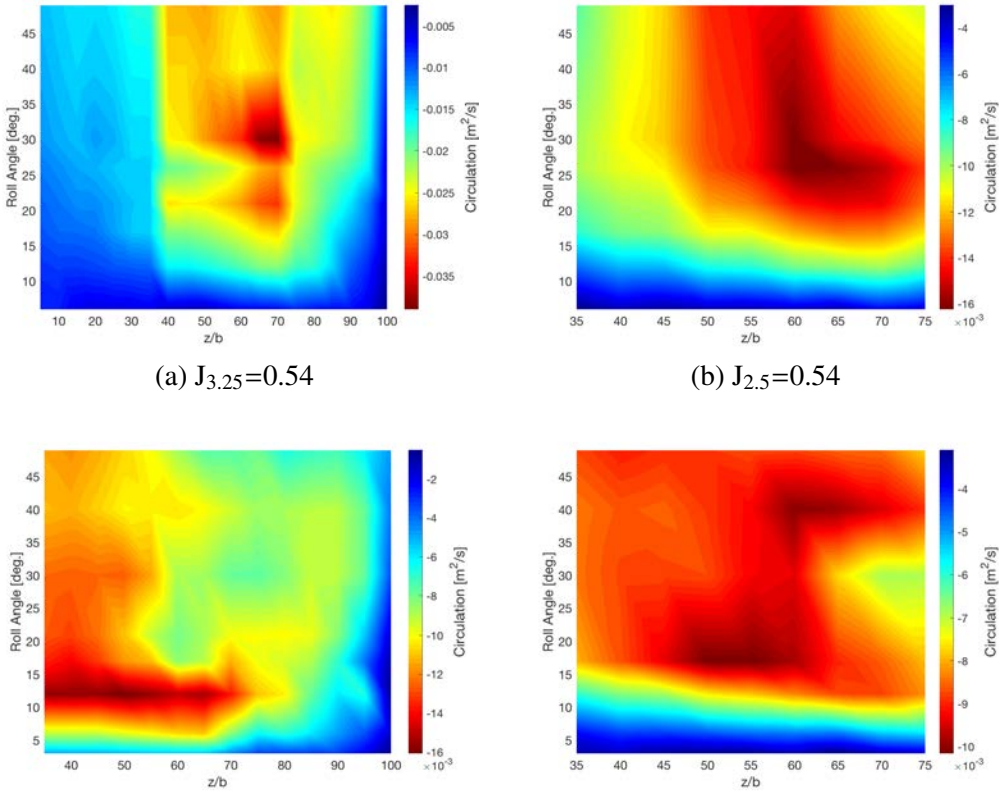

(a) $J_{3.25}$=0.54 (b) $J_{2.5}$=0.54

(c) $J_{3.25}$=1.36 (d) $J_{2.5}$=1.36

Figure 5.3: Spatiotemporal distribution of circulation.

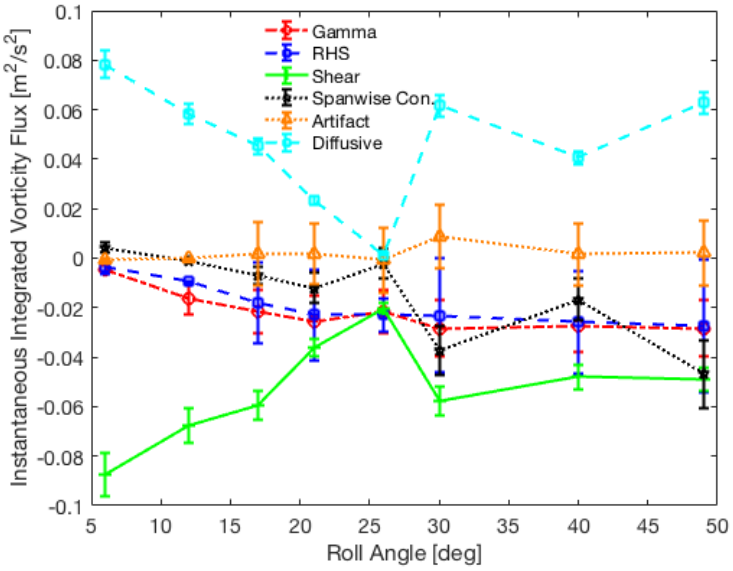

Figure 5.4: Flux distribution for $J_{3.25}$=0.54 at z/b=0.5.

the velocity field derived from plenoptic PIV, except for the integral on boundary 4 of the control region, which requires knowledge of the pressure on the surface of the wing. Pressure measurements were acquired at $z/b = 0.5$ to determine the surface diffusive flux on boundary 4. For the calculations in equation 3.13, a central difference scheme is used to calculate derivatives. Plotted in figure 5.4 is $J_{3.25} = 0.54$ computed at the mid-span location ($z/b = 0.50$), which shows the contributions of each term of the vorticity transport equation 3.13 discussed in chapter 3. The computed rate of change of circulation agrees well with the sum of the terms on the right hand side of equation 3.13 (RHS), indicating that the transport mechanisms governing control-region circulation are adequately described by equation 3.13. Based on this agreement, the diffusive flux on boundary 4 will be computed directly from equation 3.13, using plenoptic PIV data to obtain the remaining terms, and

assuming equality.

Figure 5.4 shows that the dominant contributions to the circulation within the control region are the leading-edge shear layer and the surface diffusive flux on boundary 4. It should be noted that the sign of the vorticity in the shear layer and LEV is primarily negative; hence the negative circulation contribution of the shear layer. The diffusive flux is opposite in sign, and thus strongly regulates the strength of the vortex as the shear layer contribution continues throughout the stroke. In the initial part of the roll maneuver ($\phi \leq 26°$), the spanwise convective flux contributes little to circulation growth, but grows to magnitudes on the order of the shear layer contributions later in the stroke. This will be discussed in detail. Interestingly, the tilting and Coriolis terms remain small throughout the stroke.

As discussed in chapter 3, Coriolis accelerations have been shown to play a role in governing LEV attachment on revolving wings. Possible effects of Coriolis accelerations can be divided into the categories of those that affect circulation directly, and those that otherwise affect flow dynamics, such as redistribution of existing vorticity. We consider the former possibility in the present work. In this regard, it should be noted that the free vorticity in the flow can be tilted by velocity gradients; however, the Coriolis tilting effect described in equation 3.9 acts on apparent vorticity present in the non-inertial coordinate system, due to solid-body rotations. Since these rotations are determined only by the wing kinematics, velocity gradients in the flow cannot tilt them, and we therefore assert that the Coriolis contributions, as presented in equation 3.9, cannot produce any real effect on circulation, but rather provide a correction to the tilting terms computed based on measurements

in the non-inertial frame.

The x- and y-components of the physical and Coriolis tilting contributions are examined in figure 5.5. Figure 5.5a shows that the spatial integral of x- and y-tilting terms within the control region exhibit a highly symmetric behavior as the roll angle progresses, resulting in significant cancellation of their contributions to the circulation within the control region. This was also observed by Wojcik and Buchholz [89] for a wing revolving in quiescent fluid. The Coriolis tilting, shown in figure 5.5b, behaves in a similar manner with similar amplitude as the physical tilting term. The net tilting and Coriolis contributions, as well as their sum is presented in figure 5.5c. It is evident that the net Coriolis contribution is less than that of the physical tilting contribution. As will be shown in the next section, these values are small in comparison to those due to the other fluxes represented in equation 3.13, and therefore do not have a significant effect on the circulation within the control region.

5.2 Vorticity Transport Analysis on the $J_{3.25} = 0.54$ Case

Figure 5.6 shows the circulation contributions for each of the vorticity transport fluxes, throughout the roll maneuver, and over the majority of the span of the wing, for the $J_{3.25} = 0.54$ case. The sum of tilting and Coriolis contributions in each case is shown as a single contribution, since their values are small, and not a significant part of the circulation budget. Similarly, the rate of change of circulation within the control region is small compared to the dominant flux contributions, indicating slow growth of the vortex, due to an approximate balance of fluxes throughout the measured roll angles. Figures 5.6a through

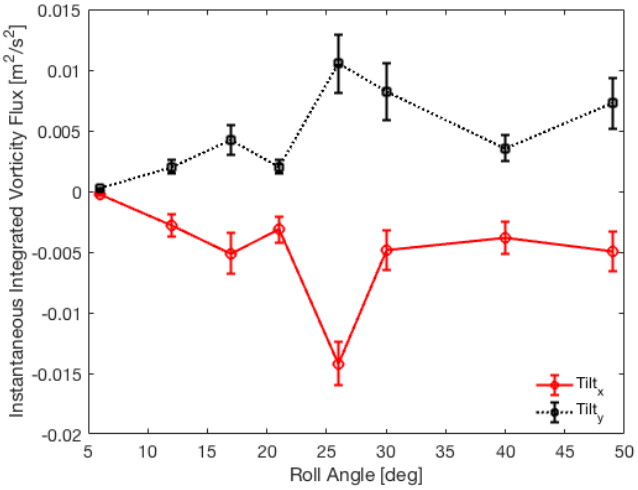

(a) Tilting x and y components

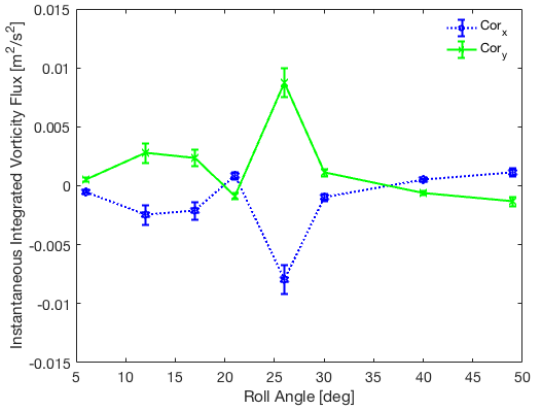

(b) Coriolis x and y components

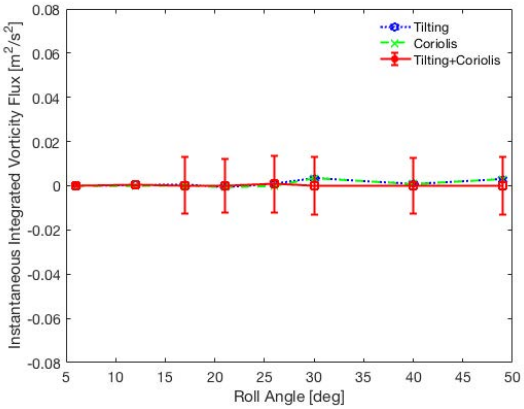

(c) Sum of Coriolis and Tilting

Figure 5.5: Coriolis and tilting fluxes, integrated over the control region, for $J_{3.25} = 0.54$ at $z/b = 0.5$. a) x- and y- tilting terms ($\omega_x \partial u_z/\partial x$, and $\omega_y \partial u_z/\partial y$), b) corresponding Coriolis terms ($2\Omega_x \partial u_z/\partial x$, and $2\Omega_y \partial u_z/\partial y$), and c) a comparison between tilting and Coriolis contributions, as well as the net values of combined tilting and Coriolis contributions.

5.6c contain data for planes within Region 1, figures 5.6d through 5.6f describe Region 2, and figures 5.6g to 5.6i describe Region 3. Juxtaposition of the transport rates for each of the regions in this way reveals distinct characteristics associated with each region.

Region one is characterized by a slow but relatively steady circulation growth due to the shear-layer flux, that is initially balanced by surface diffusion of circulation with similar magnitude. The diffusive flux diminishes over time and is overtaken by spanwise convection of circulation in the latter half of the maneuver.

Of particular interest are the origin and distribution of the spanwise convective flux. Figure 5.7 shows the sectional distributions of vorticity, and the constituents of the growing spanwise convective contributions: spanwise velocity (u_z), vorticity gradient ($\partial\omega_z/\partial z$), and the spanwise convective flux itself ($u_z\partial\omega_z/\partial z$) within a chordwise plane at $z/b = 0.25$. Note that the contribution to circulation, in equation 3.13 and figure 5.6 is the negative integral of this quantity, so blue (negative) regions in figures 5.7p to 5.7t produce positive contributions in figure 5.6c Figure 5.6b reveals an increase in control-region circulation magnitude until $\phi \approx 17$ deg. During that time, the contributions due to the spanwise convective flux are small compared to the shear layer and diffusive fluxes, and the spanwise vorticity distribution (figures 5.7a and 5.7b) reveals a vortex growing in size. As the spanwise convection of circulation increases – beginning at $\phi = 21$ deg., the vorticity distribution exhibits a regression in LEV development, as the LEV vorticity distribution becomes slightly more diffuse, reconnects to the downstream boundary layer, and collapses down toward the surface of the wing. In figure 5.7e, a weak vortical feature is apparent above the boundary layer, near the downstream edge of the frame. This is likely an artifact of the wing mounting bracket.

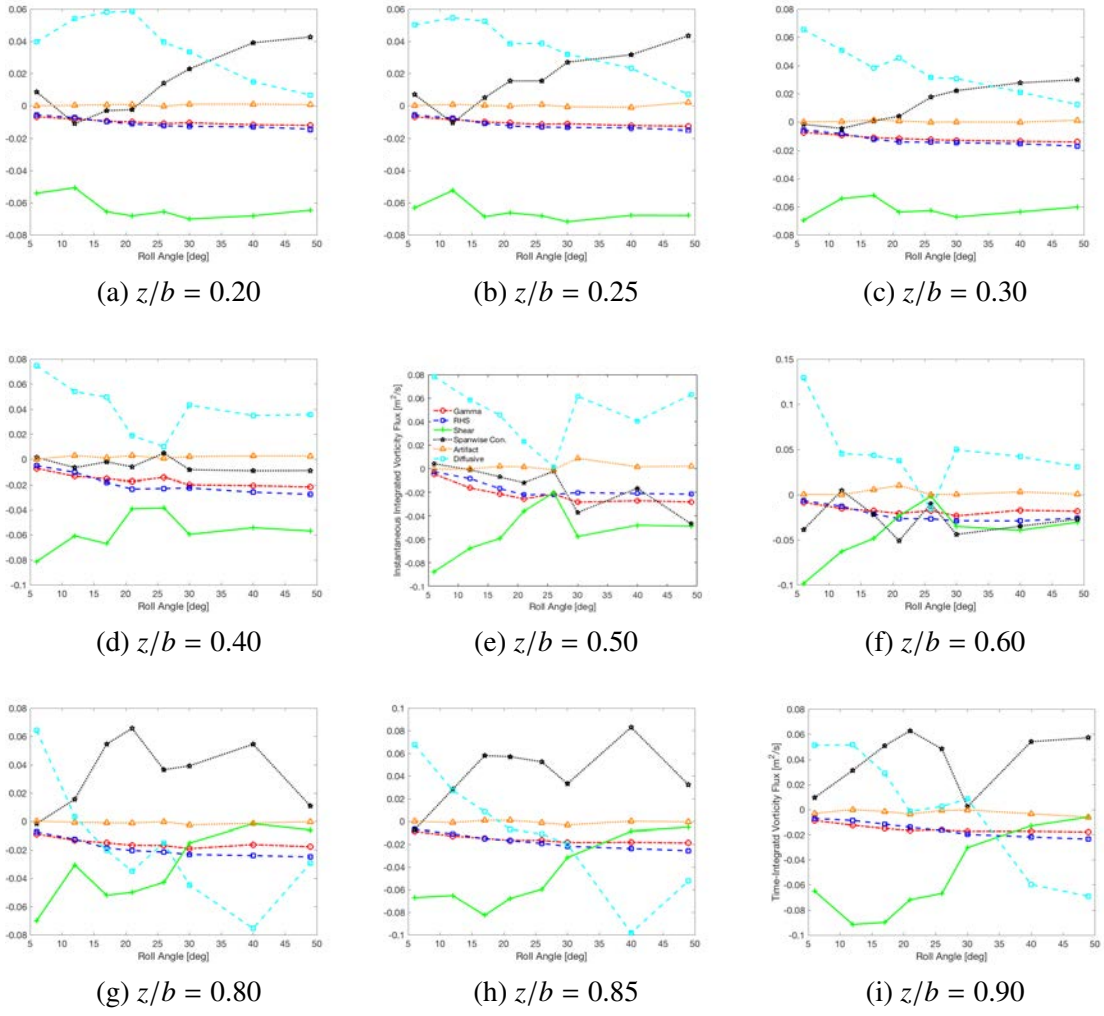

(a) $z/b = 0.20$ (b) $z/b = 0.25$ (c) $z/b = 0.30$

(d) $z/b = 0.40$ (e) $z/b = 0.50$ (f) $z/b = 0.60$

(g) $z/b = 0.80$ (h) $z/b = 0.85$ (i) $z/b = 0.90$

Figure 5.6: Vorticity transport budget for the attached region (top row), separated region (middle row) and tip induced region (bottom row).

At ϕ = 12 deg., figure 5.7f reveals a negative (tip-to-root) spanwise flow through much of the LEV cross-section. It should be noted that, before initiation of the roll maneuver, the pitch angle of the wing is such that the wing has a negative angle of attack, and the initial negative velocity is probably a remnant of three-dimensional root effects before the motion started. By ϕ = 17 deg. (figure 5.7g), the spanwise velocity is predominantly positive, and remains positive throughout the recorded motion. The spanwise vorticity gradient shown in figures 5.7k through 5.7o is predominantly negative, with greatest magnitude in the vicinity of the downstream, upper portion of the LEV, because of the expanding cross-section of the conical LEV with increasing spanwise position. The outboard convection of this gradient distribution, by the velocity fields shown in figures 5.7g through 5.7j, results in the classical spanwise convective sink often attributed to LEV regulation on revolving wings [54, 48, 92] . Interestingly, the weak vortical feature observed in figure 5.7j produces a local, strong, negative (red) spanwise convective flux, as shown in figure 5.7t.

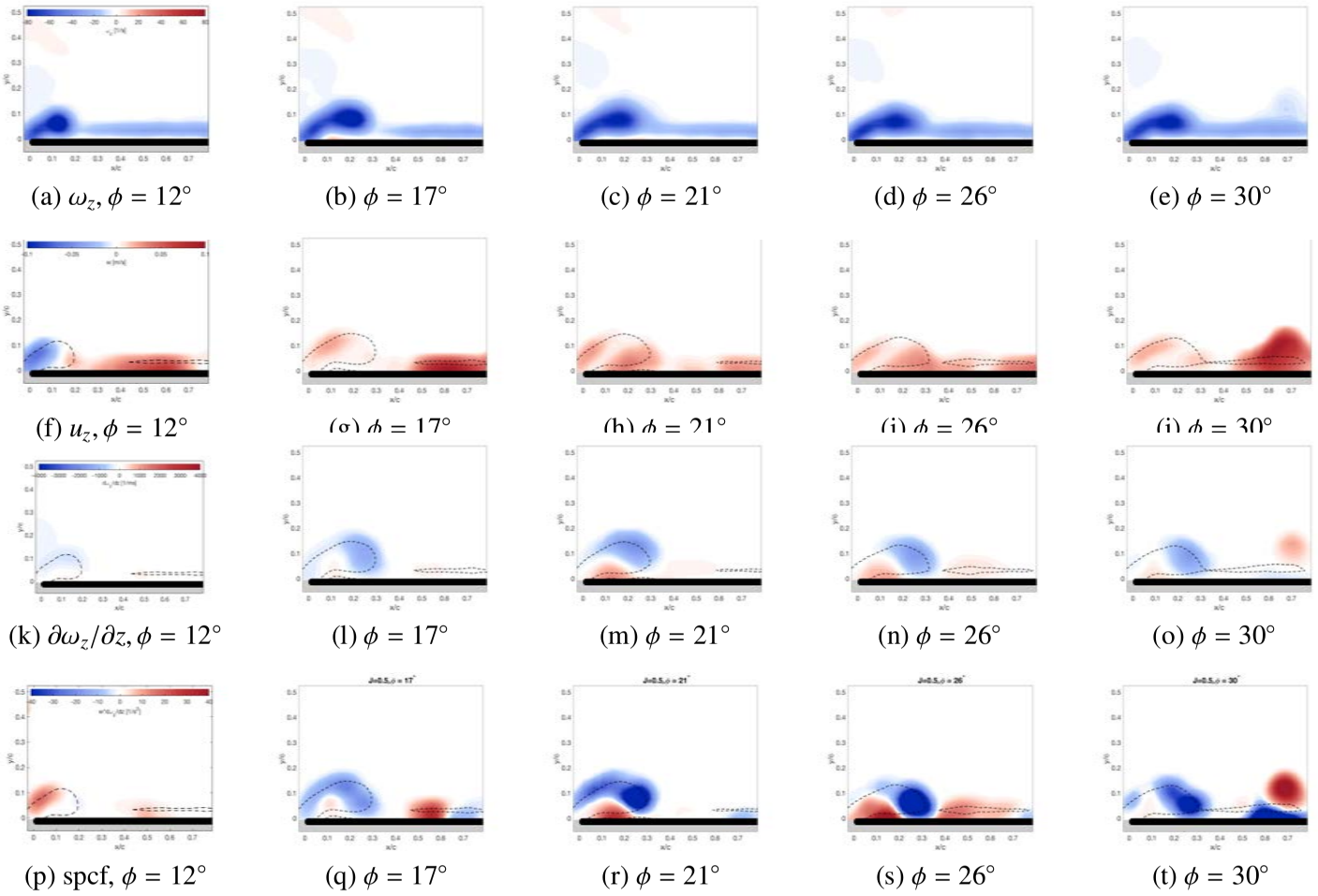

(a) $\omega_z, \phi = 12°$ (b) $\phi = 17°$ (c) $\phi = 21°$ (d) $\phi = 26°$ (e) $\phi = 30°$

(f) $u_z, \phi = 12°$ (g) $\phi = 17°$ (h) $\phi = 21°$ (i) $\phi = 26°$ (j) $\phi = 30°$

(k) $\partial\omega_z/\partial z, \phi = 12°$ (l) $\phi = 17°$ (m) $\phi = 21°$ (n) $\phi = 26°$ (o) $\phi = 30°$

(p) spcf, $\phi = 12°$ (q) $\phi = 17°$ (r) $\phi = 21°$ (s) $\phi = 26°$ (t) $\phi = 30°$

Figure 5.7: The LEV formation and components of the spanwise convective flux (spcf) at z/b=0.25. (a-e): evolution of the vorticity field, (f-j): spanwise velocity (u_z), (k-o): spanwise vorticity gradient ($\partial\omega_z/\partial z$), (p-t): the product of spanwise velocity and vorticity gradient ($u_z\partial\omega_z/\partial z$). Note that the actual spanwise convective flux in equation 3.13 within the control region is the opposite sign of $u_z\partial\omega_z/\partial z$.

Region two has a LEV with different flow topology than region one. The inboard portion of this region exhibits a quasi two-dimensional LEV. While the outboard portion of this region, develops an arch similar to a low aspect ratio plunging plate shown by Visbal [82], and creates a tip to root flow induced by this arch. In the case of the plunging plate, the arch vortex develops about the midspan; this is not the case for the rolling wing which, initiates at $z/b \approx 0.70$. Similar to a plunging plate, the primary sink of circulation in Region 2 (figures 5.6d through 5.6f) provided by the diffusive flux [26, 3]. However, with the shear layer contribution being the primary source of LEV circulation at some spanwise positions and roll angles, spanwise convection actually strengthens the vortex. This is particularly true at $z/b = 0.60$ (figure 5.6c, for $\phi > 30$ deg.), where the spanwise-convective and shear-layer contributions are similar.

Looking specifically at the midspan, z/b=0.5, figure 5.6e shows the vorticity transport budget, and figure 5.8, is the LEV evolution, the spanwise convective contribution and its constituent parts at this location. The later illustrates how the LEV grows in this region via the spanwise convective contribution.

The diffusive flux begins to decrease more sharply at $\phi = 17$ deg. (Fig. 5.8b). This is contemporaneous with the increase of secondary vorticity beneath the LEV. The shear layer reaches a minimum contribution by $\phi = 26$ deg., as the LEV begins to pinch off. A second LEV begins to roll up and form the dual vortex system observed Bross et al. [12]. Johnson et al. [42] describes this in detail for this particular case. After the formation of this dual vortex system the shear layer and diffusive flux recover.

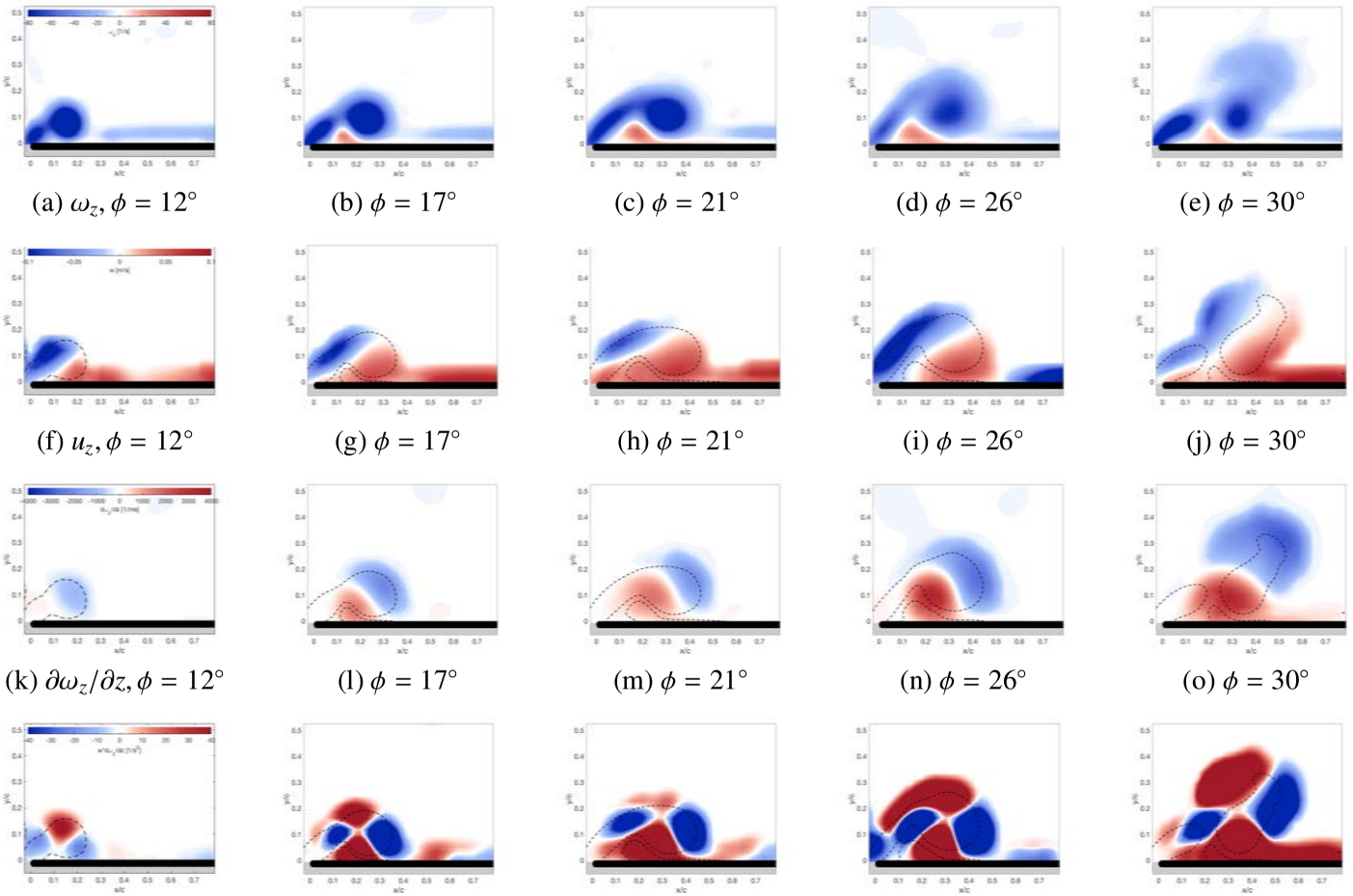

(a) ω_z, ϕ = 12° (b) ϕ = 17° (c) ϕ = 21° (d) ϕ = 26° (e) ϕ = 30°

(f) u_z, ϕ = 12° (g) ϕ = 17° (h) ϕ = 21° (i) ϕ = 26° (j) ϕ = 30°

(k) $\partial\omega_z/\partial z$, ϕ = 12° (l) ϕ = 17° (m) ϕ = 21° (n) ϕ = 26° (o) ϕ = 30°

(p) spcf, ϕ = 12° (q) ϕ = 17° (r) ϕ = 21° (s) ϕ = 26° (t) ϕ = 30°

Figure 5.8: The LEV formation and components of the spanwise convective flux (spcf) at z/b=0.50. (a-e): evolution of the vorticity field, (f-j): spanwise velocity (u_z), (k-o): spanwise vorticity gradient ($\partial\omega_z/\partial z$), (p-t): the product of spanwise velocity and vorticity gradient ($u_z\partial\omega_z/\partial z$). Note that the actual spanwise convective flux in equation 3.13 within the control region is the opposite sign of $u_z\partial\omega_z/\partial z$.

For much of the roll maneuver, the circulation budget in Region 3 is dominated by the spanwise convective contribution and the diffusive contribution. The shear layer contribution is relatively weak due to pressure relief on the pressure of the surface from tip effects. The rotational effects don't dominate here, as they do in the Region 1.

Figure 5.9 shows the LEV evolution, the spanwise convective flux and its constituent parts from ϕ = 12 deg. to ϕ = 30 deg. (fig. 5.9a-5.9e) at z/b =0.8. At ϕ = 21 deg. the shear layer flux is rapidly decreasing, with a concurrent spanwise velocity from the tip to root (fig. 5.9h), induced by the tip vortex in the upper region o the LEV. While the spanwise velocity is in the inboard direction, this acts as a weakening of the LEV (fig.5.9r). This behavior of the spanwise convective contribution can be attributed to the arch induction. This induction drives the spanwise velocity toward the root in the upper portion of the shear layer. The vorticity gradient shows strengthening of the LEV in the outboard region drawn inboard by the arch induction to strengthen the vortex. As the motion continues, an outboard flow develops (fig. 5.9j), while the spanwise convective contribution decreases. The spanwise convective contribution reaches a minimum at ϕ = 30 deg., while the LEV lifts off the surface at this spanwise location. Outboard of this location the LEV remains pinned. The spanwise convective contribution acts as a reverse evolution process in this region similar to that observed by Akkala and Buchholz [3] for an aspect ratio 2 plunging plate.

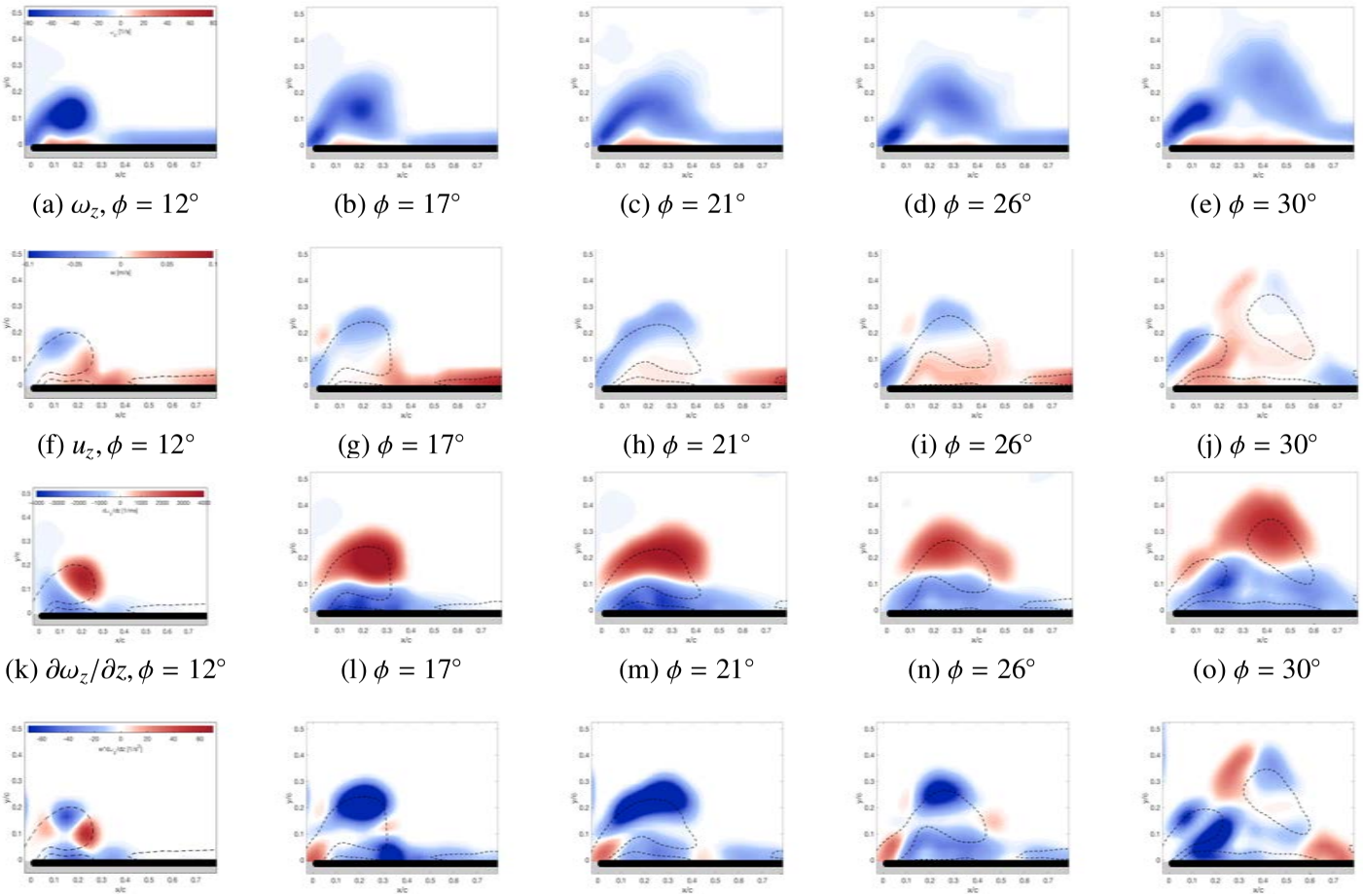

(a) ω_z, $\phi = 12°$ (b) $\phi = 17°$ (c) $\phi = 21°$ (d) $\phi = 26°$ (e) $\phi = 30°$

(f) u_z, $\phi = 12°$ (g) $\phi = 17°$ (h) $\phi = 21°$ (i) $\phi = 26°$ (j) $\phi = 30°$

(k) $\partial\omega_z/\partial z$, $\phi = 12°$ (l) $\phi = 17°$ (m) $\phi = 21°$ (n) $\phi = 26°$ (o) $\phi = 30°$

(p) spcf, $\phi = 12°$ (q) $\phi = 17°$ (r) $\phi = 21°$ (s) $\phi = 26°$ (t) $\phi = 30°$

Figure 5.9: The LEV formation and components of the spanwise convective flux (spcf) at z/b=0.80. (a-e): evolution of the vorticity field, (f-j): spanwise velocity (u_z), (k-o): spanwise vorticity gradient ($\partial\omega_z/\partial z$), (p-t): the product of spanwise velocity and vorticity gradient ($u_z\partial\omega_z/\partial z$). Note that the actual spanwise convective flux in equation 3.13 within the control region is the opposite sign of $u_z\partial\omega_z/\partial z$.

5.2.1 The Role of Radius of Gyration

Decreasing radius of gyration pushes circulation distributions further outboard. Circulation for the baseline case shown in figure 5.3a, has a strong gradient line delineating Region 1 and Region 2, where Region 2 contains the strongest circulation. The maximum circulation is observed near the $z/b = 0.62$ for the baseline case. For the $J_{2.5} = 0.54$ case (fig. 5.3b) the maximum circulation occurs near $z/b = 0.68$. A similar behavior can be seen in the $J = 1.36$ cases. For the larger R_g/c, $J_{3.25} = 1.36$ the maximum circulation is near $z/b = 0.62$ (fig. 5.3c), while for $R_g/c = 2.5$ the maximum occurs $z/b = 0.68$ (fig. 5.3c).

5.2.2 The Role of Advance Ratio

The role of advance ratio dictates the maximum circulation, at a given R_g/c. An increase in the advance ratio will decrease the maximum dimensionless circulation observed on the wing for a given R_g/c. Looking at $J_{3.25} = 0.54$ and $J_{3.25} = 1.36$ case, it is seen from figures 5.3 that $J_{3.25} = 0.54$ has a stronger maximum dimensionless circulation which peaks around at $\Gamma^* = -0.39$, while for $J_{3.25} = 1.36$ $\Gamma^* = -0.016$. The dimensionless circulation is non-dimensionalized by the chord,c, and the relative velocity at the radius of gyration, u_{rel}. This accounts for the velocity induced by the rotation. A similar behavior is seen at the lower R_g/c, $J_{2.5} = 0.54$ which has a maximum circulation of $\Gamma^* = -0.016$ and for $J_{2.5} = 1.36$ which has a maximum $\Gamma^* = -0.01$.

The advance ratio dictates the shear layer distribution over the span, when comparing $J = 0.54$ and $J = 1.36$. Figure 5.10c and 5.10d, have a more constant distribution while

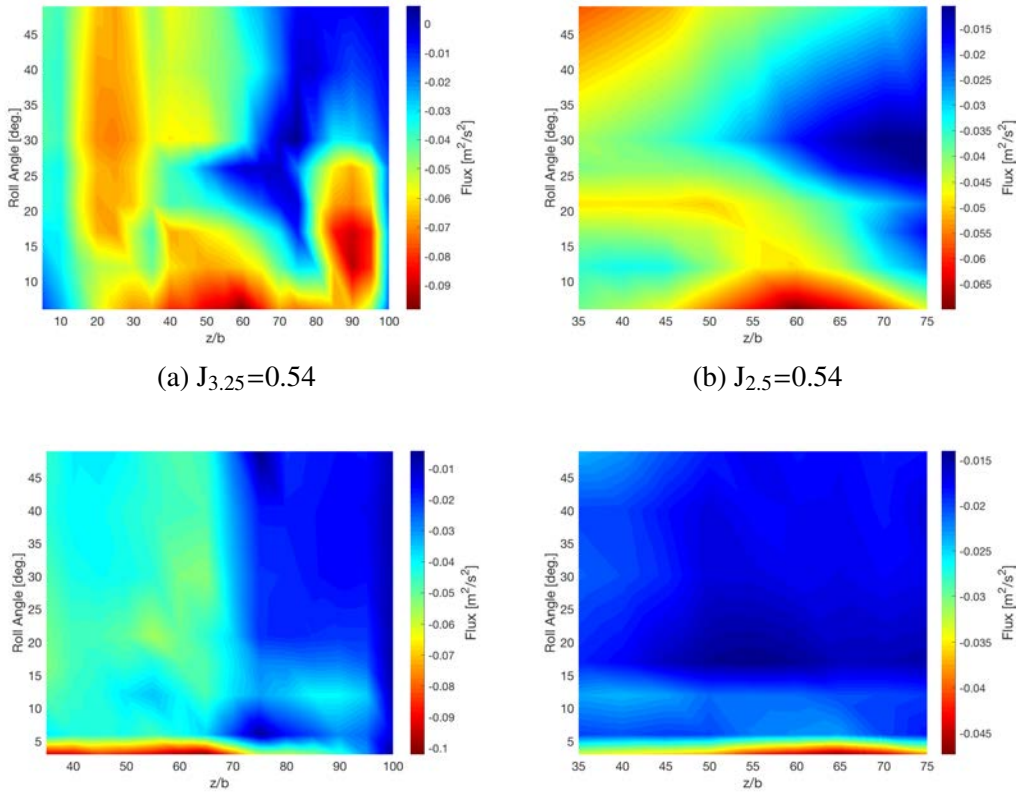

(a) $J_{3.25}$=0.54 (b) $J_{2.5}$=0.54

(c) $J_{3.25}$=1.36 (d) $J_{2.5}$=1.36

Figure 5.10: Spatiotemporal distribution of shear layer flux.

the $J = 0.54$ cases (figs. 5.10a and 5.10b) do not have a constant contribution. This is from the regions the form on the later case. I the former case the shear layer is driven by the rapid formation of the first LEV and the constant shedding of subsequent LEV's, which are being aliased.

5.3 Conclusion

Four cases that were in pure roll maneuver, which were held at $\alpha_{geo} = 33°$ for the duration of the motion, for two different advance ratios and R_g/c were studied. Vorticity

transport framework was extended to include non-inertial accelerations. It was found that the Coriolis term is a correction for the tilting term and did not contribute significant to the LEV formation. The baseline case ($J_{3.25} = 0.54$) exhibited three distinct regions encompassing a broad range of LEV behaviors previous observed on maneuvering wing. Region 1, in which an attached, conical LEV was observed during the measured trajectory, was governed by the shear layer flux which was near constant, and was balanced by the diffusive flux early in the motion, and then the spanwise convective contribution. Region 2 consisted of a quasi two dimensional LEV, a dual vortex system, and an arch structure. The shear layer contribution was the dominant source of vorticity, while in some spanwise location the spanwise convective contribution driven by the arch contributed as a source. These sources were balanced by the diffusive contribution, similar to a plunging wing. Region 3 was observed to be driven by tip effects, where the LEV wing was pinned to the surface, and exhibited a *reverse* evolution previously seen in a plunging plate. The circulation budget was dominated by a balance between the diffusive flux and the spanwise convective contribution which reversed the LEV evolution process to reattach the LEV to the downstream boundary layer. The role of the R_g/c was found to push the circulation distribution outboard. The advance ratio was found to determine the strength of the circulation, and also affected the overall structure of the flow. As the advance ratio decreased there was an increase in the non-dimensional circulation. That

CHAPTER 6
PURE PITCHING

In this section a pitch up maneuver will be examined to understand how the LEV forms and evolves, during this maneuver. The pitch up maneuver is the second of two maneuvers that will set the baseline behavior of the transport properties for the coupled pitching and rolling case. A typical pitch up maneuver is shown in Figure 6.2. The motion starts at $\alpha = 0°$ and pitches to a maximum of $\alpha = 45°$. An Eldredge smoothing function (Eq. 6.1) is used during the starting and ending phase of the motion to reduce vibration in the wing, that can alter LEV formation.

$$\alpha(t) = \frac{k}{a} ln\left[\frac{cosh(a(t-t_1))cosh(a(t-t_3))}{cosh(a(t-t_2))cosh(a(t-t_4))}\right] \tag{6.1}$$

Data is collected every 5 degrees of rotation starting at $\alpha = 5°$. Two reduced pitch rates (k) are examined, of 0.2 and 0.5, where k is defined in equation 6.2. Equation 6.2 is a ratio between how fast a wing is pitching in reference to the free-stream, this rate is composed of, $\dot{\alpha}$ which is the pitch rate, c is the chord, and U_∞ is the free-stream velocity. Figure 6.2 highlights the non-inertial frame x' and y' and the pitch angle α. The plate pitches about the leading edge, where the non-inertial coordinates are located.

$$k = \frac{\dot{\alpha}c}{2U_\infty} \tag{6.2}$$

This will give insight into what governs LEV development, and evolution for a fast pitch case (k=0.5) and slow pitch case (k=0.2).

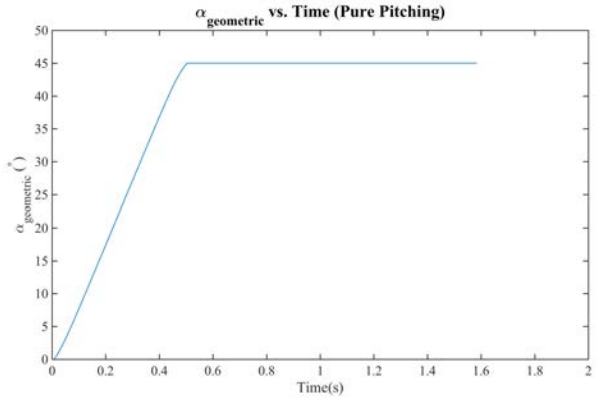

Figure 6.1: Kinematics of the pitch up maneuver.

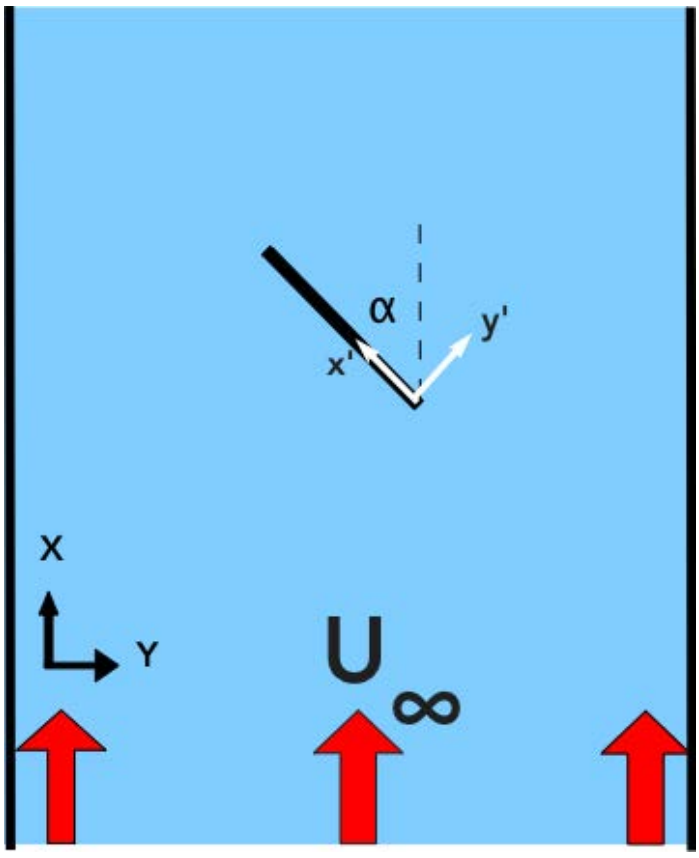

Figure 6.2: Diagram depicting a top down view of the pitch angle and the non-inertial reference frame.

6.1 Flow topology of a Purely Pitching Plate

For both reduced pitch rates, $k = 0.2$ and $k = 0.5$, the LEV evolves vastly different when compared to the baseline pure roll case case shown in figure 6.3. For the pure pitch maneuver an arch vortex forms across the span and begins to lift off, and eventually sheds. However, for the baseline roll case three distinct regions form. In the middle region (Region 2) can be considered similar to a plunging plate, or even reduced version (in the spanwise extent) of the pitching wing, where an arch forms.

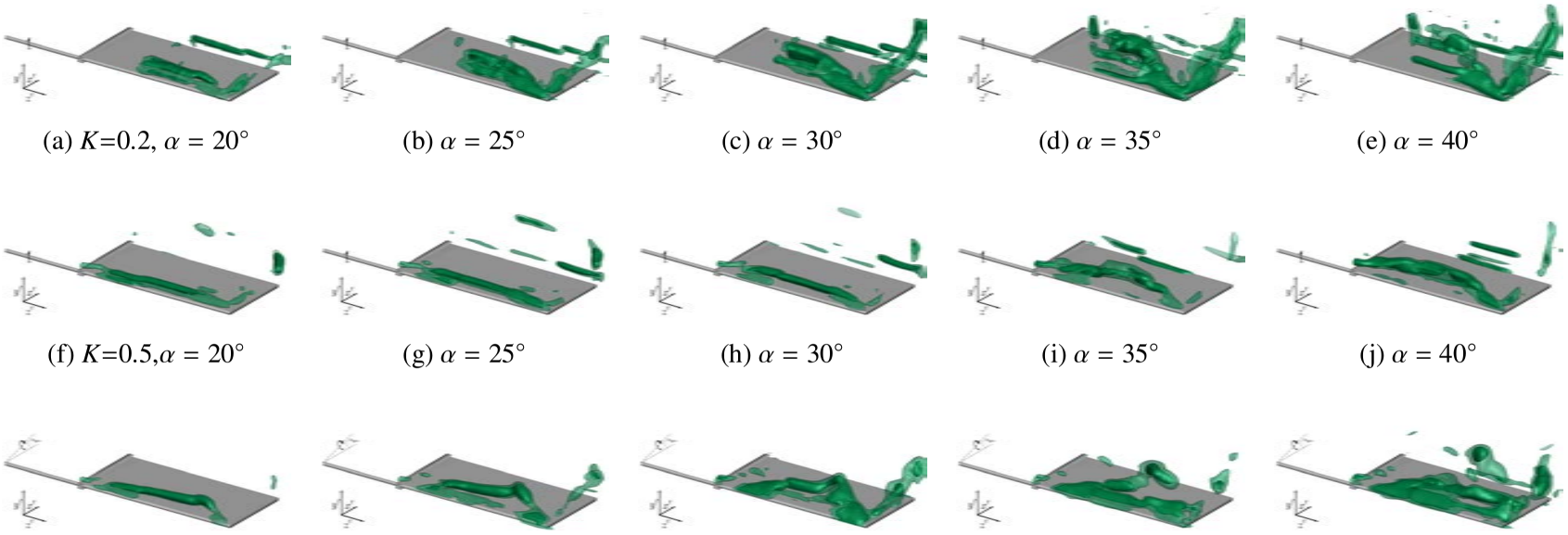

(a) K=0.2, α = 20° (b) α = 25° (c) α = 30° (d) α = 35° (e) α = 40°

(f) K=0.5,α = 20° (g) α = 25° (h) α = 30° (i) α = 35° (j) α = 40°

(k) $J_{3.25}$=0.54,ϕ = 12° (l) ϕ = 17° (m) ϕ = 21° (n) ϕ = 30° (o) ϕ = 40°

Figure 6.3: LEV formation shown with isosurfaces of normalized swirling strength, for k=0.2, k=0.5 from α = 20° to α = 40° and for $J_{3.25}$ = 0.54 over the roll angles of ϕ = 12° to ϕ = 40°.

6.2 Vorticity Transport on a Wing In Pure Pitch

Using vorticity transport analysis for the three cases shown in figure 6.4, it is seen that the shear layer contribution is the main source of vorticity while this is balanced by the diffusive flux. It is of interest to note that the shear layer contribution in both cases (k=0.2 and k=0.5) saturates by an angle of attack of $\alpha = 25°$ (fig. 6.4b and 6.4b), this is clearly evident for z/b=0.5 shown in figure 6.5. As the shear layer contribution saturates, this is concomitant with the first sign of secondary vorticity between the shear layer and the LEV (fig. 6.6).

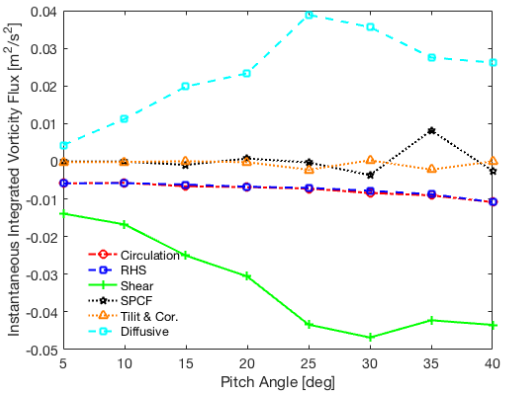

(a) k=0.5,z/b=0.35

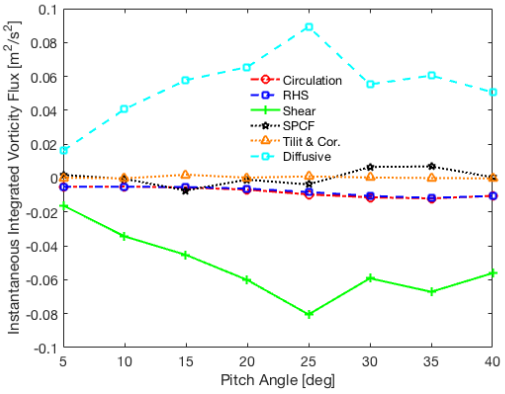

(b) k=0.5,z/b=0.50

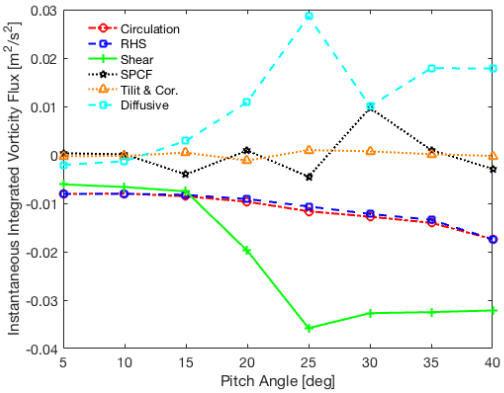

(c) k=0.2,z/b=0.50

Figure 6.4: Flux Distributions for pure pitch k=0.2 and k=0.5.

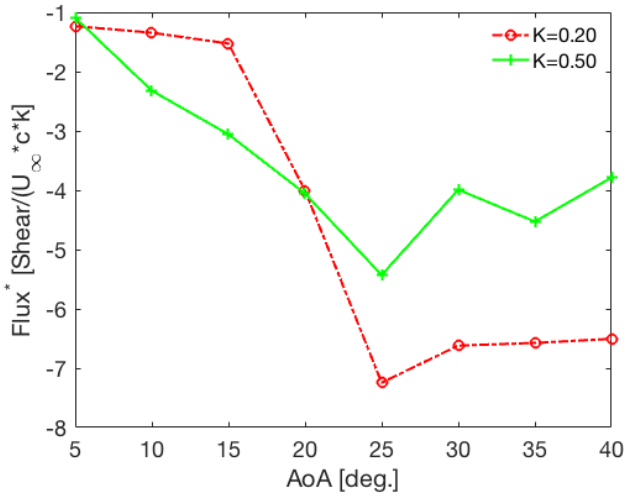

Figure 6.5: Shear layer contribution for k=0.2 and k=0.5 at z/b=0.5, highlighting the saturation at an angle of attack of $\alpha = 25°$.

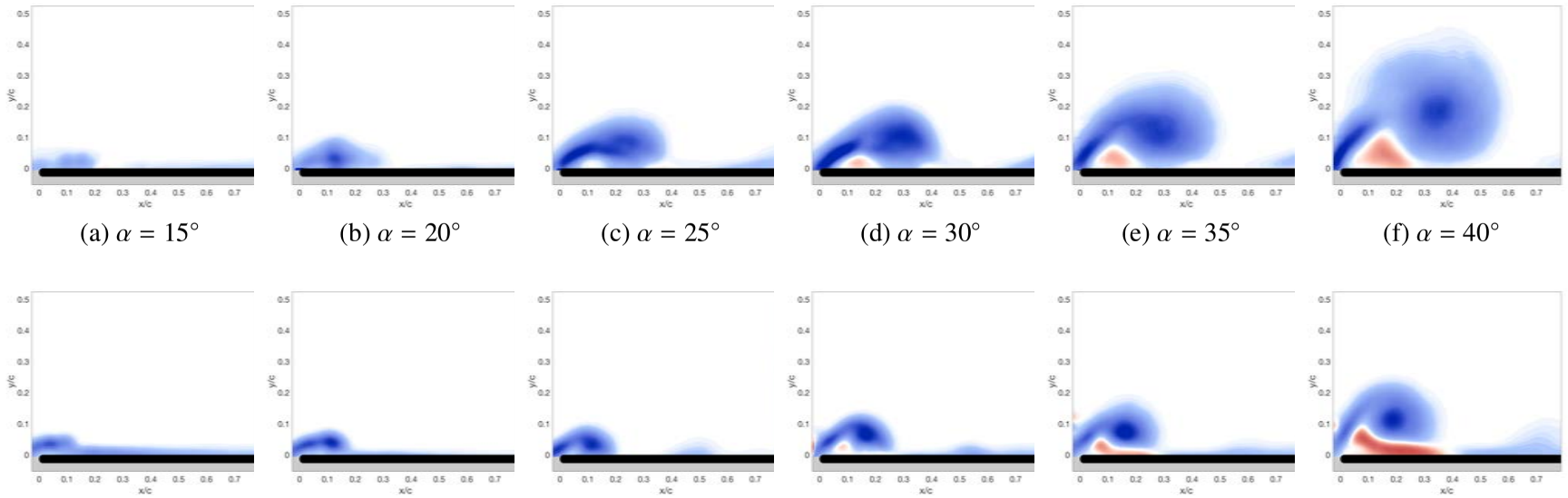

(a) α = 15° (b) α = 20° (c) α = 25° (d) α = 30° (e) α = 35° (f) α = 40°

(g) k=0.5, α = 15° (h) α = 20° (i) α = 25° (j) α = 30° (k) α = 35° (l) α = 40°

Figure 6.6: Vorticity at z/b=0.5 for a reduced pitch rate of k=0.2 (figs. 6.6a-6.6f) and k=0.5 (figs.6.6g-6.6l), over the range α = 10° − α = 40°.

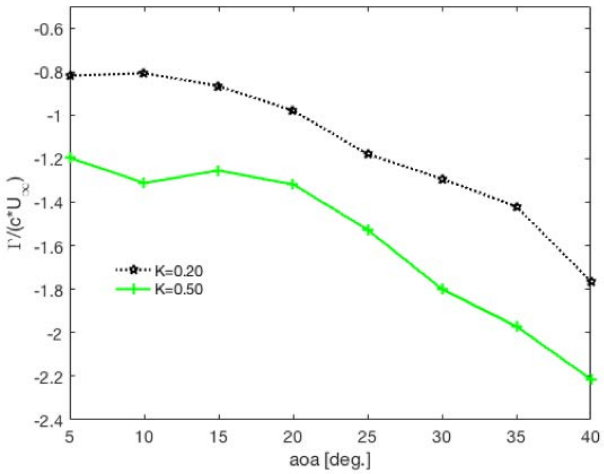

Figure 6.7: Circulation for k=0.2, and k=0.5.

6.3 Circulation of a Pitching Maneuver

Circulation generated by a pitching plate will be driven by the shear layer contribution while being regulated by the diffusive flux. Figure 6.7 shows the circulation for both cases, which appear to have similar growth. Both the shear layer and diffusive contribution are a function of the reduced pitch rate and angle of attack, but have different time scales shown in figure 6.8a. Plotting circulation against a the convective time scale highlights that the k=0.5 case reaches α_{max} in a shorter time. The circulation from a temporal perspective makes it difficult to compare, since the time scales are different.

Non-dimensionalizing by the $\Gamma/U_\infty * c$, and subtracting the first data point ($\alpha = 5°$) from all points collapses the circulation (fig. 6.8). This was done due to the fact at that there is no LEV structure shown in figure 6.6, which starts at $\alpha = 10°$, and has no LEV at this point as well. This removes the offset from the boundary layer. This shows that the circulation is a function of pitch rate since the initial values are very different. The pitch

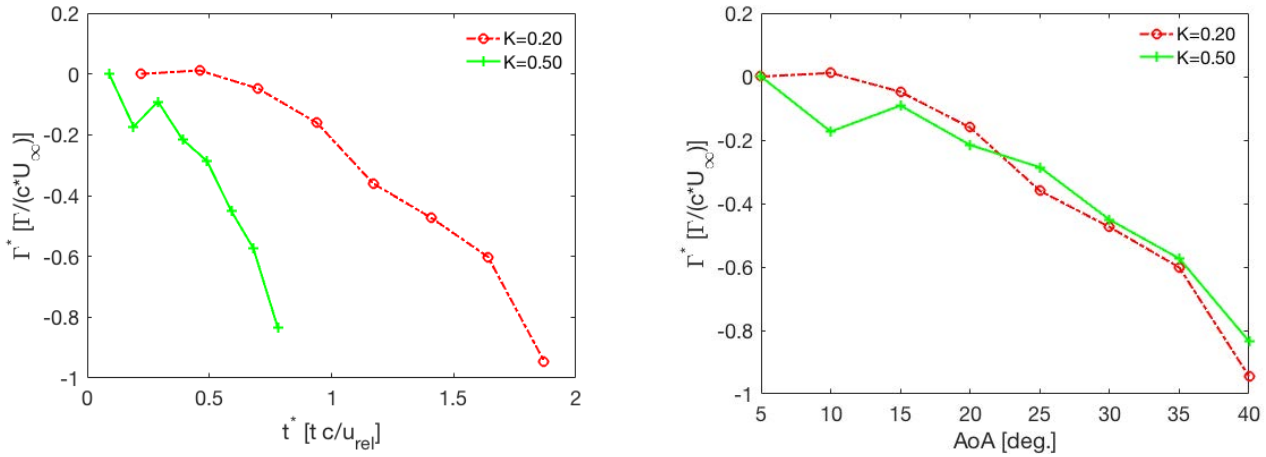

(a) t* (b) aoa

Figure 6.8: Circulation for k=0.2, and k=0.5.

rate effect is introduced at the beginning of the maneuver.

6.4 Conclusion

Pitching maneuver was examined in this chapter, which was examined from a topological perspective, and by using the vorticity transport framework. From a topology perspective, the pitching maneuver forms an arch structure, which is similar to the Region 2 and the higher J roll cases. The circulation can be collapsed if accounting for the initial boundary layer values making circulation affected by the reduced pitch rate early in the motion. The circulation magnitudes and function follow the angle of attack, once the initial value is accounted for. The diffusive flux and the shear layer contributions are functions of reduced pitch rate and angle of attack. In both the shear layer contribution and diffusive flux, a maximum is seen at an AoA of 25 deg. This is due to the secondary vorticity beginning to roll up and accumulate for both cases.

CHAPTER 7
A PITCHING WING IN A ROLLING ENVIRONMENT

In this section simultaneous pitching and rolling maneuvers will be examined. The wing will be geometrically pitched, such that when the roll velocity is constant the effective angle, α_{eff}, is zero. After the roll motion is initiated and α_{eff}=0°, the wing will pitch up with a prescribed angular velocity. This motion was governed by both J and k, a parameter k_{Rg} was defined to account for both of the these, shown in equation 7.3. This maneuver is show in figure 7.1, four different k_{Rg}'s were examined. Table 7.1 highlights what each case was composed of. Both J and k were changed to study the effect the maneuver has on the LEV formation and evolution. Specifically articulating a pitching motion on a rolling wing can help to isolate the effects of the roll motion on transport within the LEV, when compared to the pure pitch case (chapter 6). Secondly, through comparing the pure roll and pure pitch cases, we can determine whether vortex evolution in the combined motions is preferential governed by pitch or roll influences. Values were chosen to approximately match the advance ratios studied in the pure roll chapter, and the reduced pitch rates that were examined in the pure pitch chapter. The radius of gyration was held constant since there was a physical limitation on the experiment. During the pitch up motion for R_g/c=2.5 the wing would not have enough physical room to complete the pitching portion of the maneuver.

Both the pure roll maneuver and pure pitch maneuver were studied in detail in the previous chapter. The pure roll maneuver baseline case ($J_{3.25}$ = 0.54) exhibited three distinct regions. In Region 1 the shear layer contribution was relatively constant, which

was balanced by the diffusive contribution early in the motion, and then by the spanwise convective contribution later in the motion. Region 2 was balanced between the shear layer contribution and the diffusive contribution, which oscillated during the formation of the dual-vortex system. Region 3 was seen as the tip induced region, which was a balance between the diffusive contribution and the spanwise convective contribution. For the larger advance coefficient, J=1.36, it was seen that the shear layer contribution was balanced by the diffusive contribution. The contributions from each, grew quickly and then became relatively constant. As shear layer vortices were continuously created and convected out of the control region. In the case of the pure pitch maneuver, it was seen that the shear layer contribution grew until α=25 deg. and became saturated. This behavior was mirrored by the diffusive contribution.

$$k_{Rg} = \frac{\dot{\alpha}_{eff} c}{2U_{Rg}} \tag{7.1}$$

$$U_{Rg} = \sqrt{\left(\dot{\phi} R_g\right)^2 + U_\infty^2} \tag{7.2}$$

Knowing the definition of reduced pitch rate, $k = \dot{\alpha}c/2U_\infty$, and the advance ratio, $J = U_\infty/\dot{\Omega}_x R_g$, equation 7.2 can be written in terms of advance ratio:

$$k_{Rg} = \frac{k}{\sqrt{J^{-2} + 1}} \tag{7.3}$$

The effect of rolling wing on the pitching kinematics is expressed in equation 7.3. It is worth a note, that in the limit of of pure pitch, i.e. no roll, equation 7.3 reduces back to the reduce pitch rate of, $k = \dot{\alpha}c/2U_\infty$. The kinematics will be defined as in Figure 7.1,

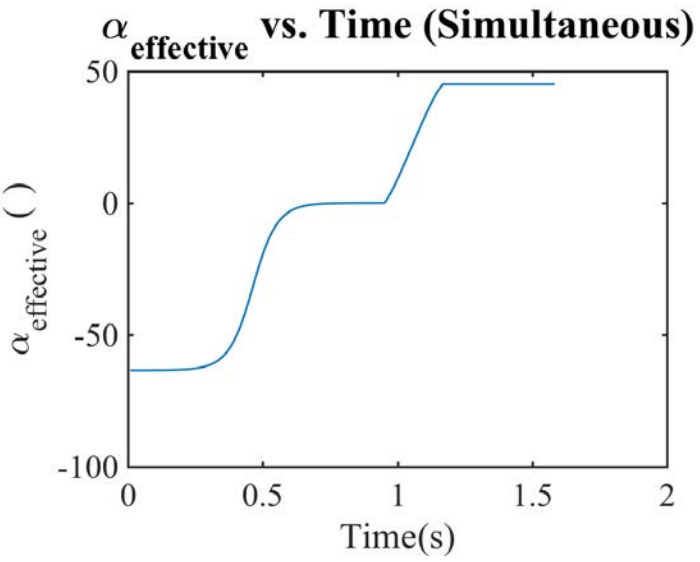

Figure 7.1: Pitch and roll kinematics.

where the wing will be feathered down, such that at a constant velocity the wing has an effective angle of attack of zero degrees at its radius of gyration. Once the wing reaches an effective angle of zero, the wing will begin to pitch up.

k_{Rg}	J	k	R_g/c
0.22	0.54	0.46	3.25
0.37	1.36	0.46	3.25
0.50	0.54	1.05	3.25

Table 7.1: Constituent parameters composing k_{Rg}.

7.1 Flow Structure of a Wing Pitching in a Rolling Environment

Figure 7.2 shows the evolution of the LEV for three of the three different k_{Rg} values. Plenoptic PIV data were acquired over the entire span for the k_{Rg} = 0.22 case, and $z/b \geq$ 0.34 for all other cases considered. The k_{Rg} = 0.22 case is shown in the first column of figure 7.2, in which its final state (α=45 deg.) looks similar to $J_{3.25}$=0.54 at ϕ=21 deg. shown in figure 5.2c. However, these two cases do not evolve in a similar manner. The pitching maneuver appears to keep he LEV attached, and near the surface similar to a pure pitching maneuver. However, dissimilar to the pure pitching kinematics where an arch structure forms about the mid-span, in this case it forms outboard of the mid-span akin to the baseline roll case. The evolution for the k_{Rg}=0.37 case, shown in second column of figure 7.2 appears more similar to the pure pitch case. The LEV remains near the surface of the plate for the duration of the motion, and does not form a outboard compact arch akin to the baseline roll case. Further more, when comparing this to the $J_{3.25}$=1.36 case, in which the LEV sheds rapidly, this LEV remains attached. Evolution for the k_{Rg} = 0.50 case, shown in the third column in figure 7.2, appears to be a superposition of both cases early in the motion. Again, the LEV remains near the surface for the duration of the motion, which is inline with higher reduced pitch rates. In this case an arch appears to form in outboard portion of the wing similar to the baseline roll case. The arch in this case is the most compact of any cases considered in this manuscript, this especially try at α=40 deg.. However, as the motion continues the arch appears to be diminishing α=45 deg. and returning to a pure pitch LEV.

J initially governs the flows structure early in the motion, since it is the only maneu-

ver being performed. This is manifested in the flow topology as the outboard arch structure. However, once the pitch maneuver initiates, the pitch rate is the governing parameter driving the flow topology.

7.2 Vorticity Transport of a Pitching Wing in a Rolling Environment

To probe into the mechanism which drives the formation of the LEV on this unique case, the vorticity transport analysis will be employed, to compare transport properties for all three cases (pure pitch, pure roll, simultaneous). Figures 7.3-7.5 are the instantaneous integrated transport properties for z/b=0.35, z/b=0.5, and z/b=0.65 for the simultaneous cases.

At z/b =0.35 all k_{Rg} values (k_{Rg}= 0.22, 0.37 and 0.50) have similar shear layer, diffusive and spanwise convective contribution evolutions, with respect to each other, shown in figure 7.3. The shear layer and diffusive contributions grow during the motion, which is the behavior that is observed in the pure pitching cases. The three cases with similar pitch rate k_{Rg}=0.22 and 0.37 values are similar as well, showing that the dominant maneuver is the pitching maneuver, which governs the flux contributions at this location. It is important to note, that for the k_{Rg}=0.22 case the flux contributions behaved in a similar manner as this location. Figure 8.5 shows the flux contributions at the midspan, z/b=0.50. Again, a similar trend is seen where the shear layer, and diffusive contributions mirror each other. This is similar to the pure pitch and in Region 2 of the baseline roll case. However, in Region 2 there is an oscillation in the contributions that is contemporaneous with the formation of the dual-vortex system. Figure 7.5 are the flux contributions at z/b=0.65. Here the k_{Rg} =

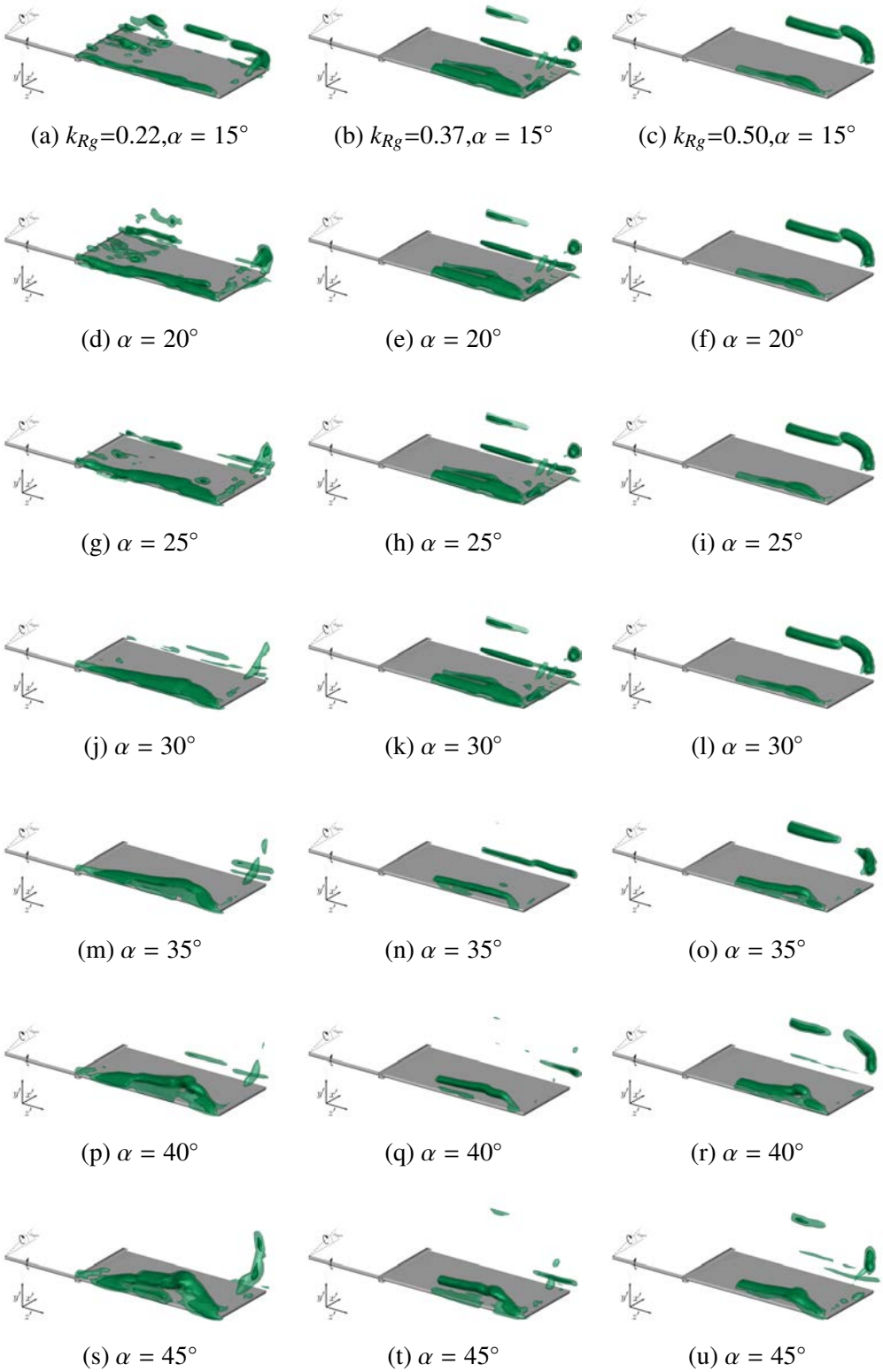

(a) k_{Rg}=0.22,α = 15° (b) k_{Rg}=0.37,α = 15° (c) k_{Rg}=0.50,α = 15°

(d) α = 20° (e) α = 20° (f) α = 20°

(g) α = 25° (h) α = 25° (i) α = 25°

(j) α = 30° (k) α = 30° (l) α = 30°

(m) α = 35° (n) α = 35° (o) α = 35°

(p) α = 40° (q) α = 40° (r) α = 40°

(s) α = 45° (t) α = 45° (u) α = 45°

Figure 7.2: LEV formation shown with isosurfaces of normalized swirling strength, for k_{Rg}=0.22 (figs. 7.2a-7.2s), k_{Rg}=0.37 (figs. 7.2b-7.2t), and k_{Rg}=0.50 (7.2c-7.2u).

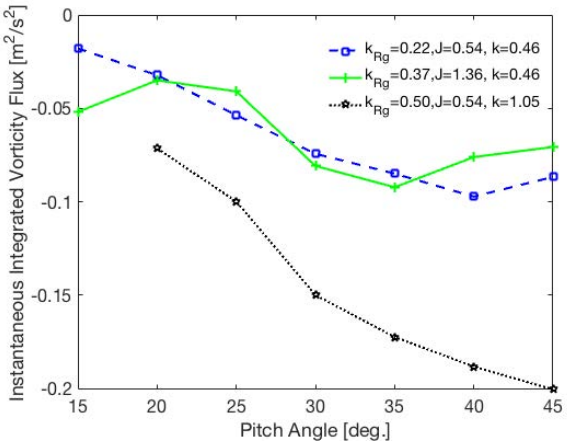

(a) Shear Layer, z/b = 0.35

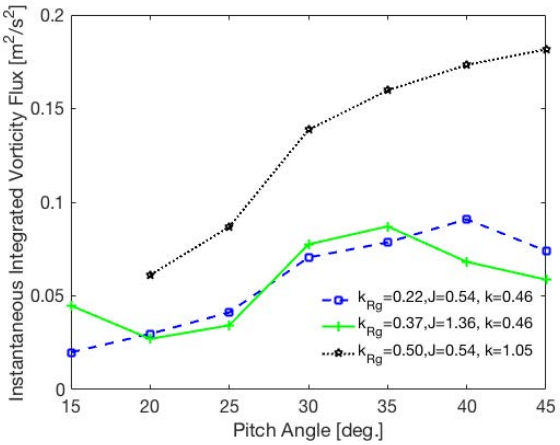

(b) Diffusive

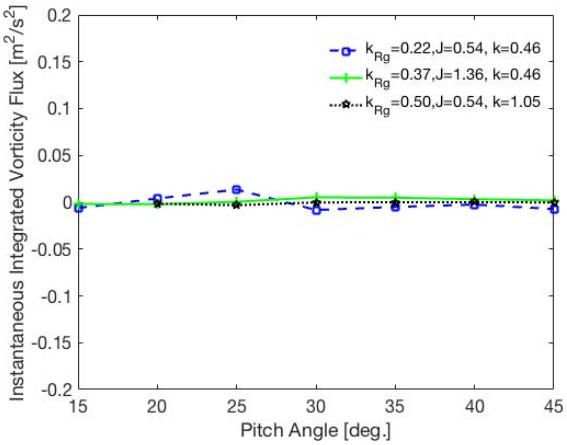

(c) SPCF

Figure 7.3: Flux Contributions for z/b=0.35.

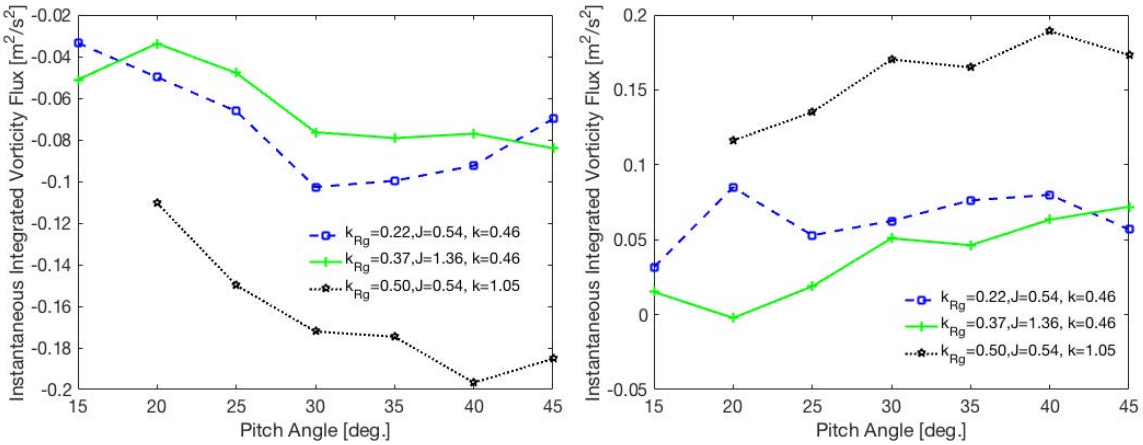

(a) Shear Layer (b) Diffusive

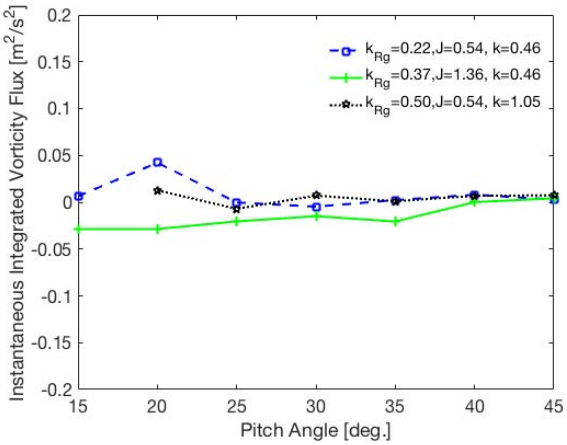

(c) SPCF

Figure 7.4: Flux Contributions for z/b=0.50.

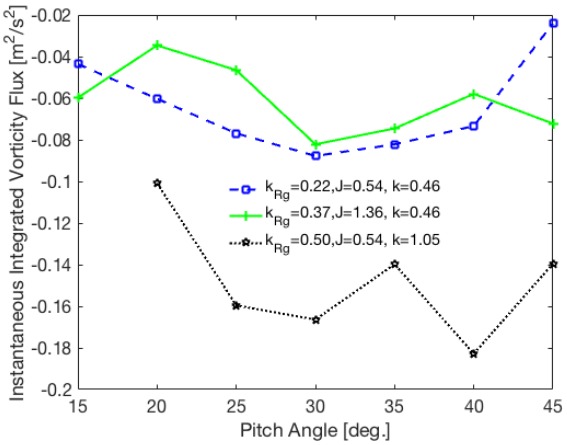

(a) Shear Layer

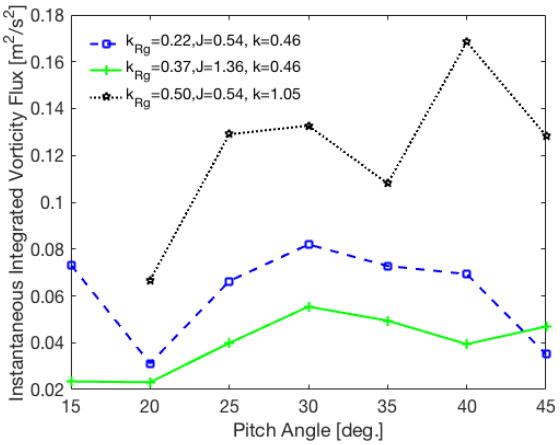

(b) Diffusive

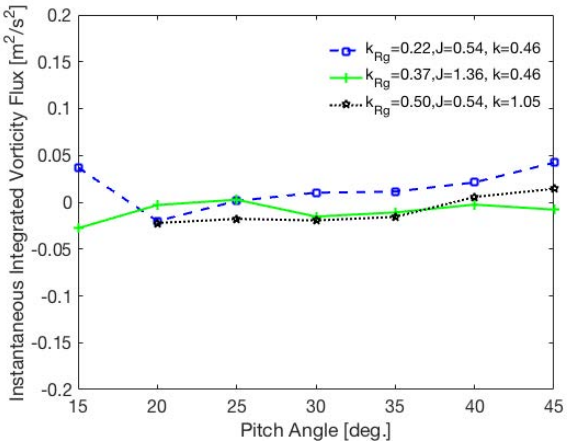

(c) SPCF

Figure 7.5: Flux Contributions for z/b=0.65.

0.22, and 0.37 all reach a maximum in the shear layer and diffusive contributions at α=30 deg., and this behavior is seen in the pure pitch case at α=25 deg. where the shear layer and diffusive contributions values saturate.The data presented points to k being the govern parameter of the flux contributions, for two reasons. The first being the similar behavior is observed over the wing similar to that of a plate in pure pitch, and secondly the shear layer contributions is balanced by the diffusive contribution, with no oscillations due to the formation of a dual-vortex system. Furthermore, to describe these in cases in a single parameter can be done with just the reduced pitch rate ,k, and not k_{Rg} since the advance coefficient plays no significant role in flux analysis. The reduced pitch rate can be further shown to be the governing parameter by comparing the similar k values which have similar values for the flux contributions and increasing k leads to larger contributions similar to the pure pitch maneuver.

Circulation distributions, are shown in figure 7.6 in all three spanwise locations, the circulation grows monotonically for the duration of the motion. This behavior is consistent with the pure pitch maneuver. For the pure roll maneuver the circulation grows rapidly then remains relatively constant. When non-dimensionalizing by u_{rel} shown in figure 7.7, which accounts for the rolling velocity at the radius of gyration, the four cases do not collapse similar to the pure pitch case. This is consistent showing that this is pitch dominated maneuver, since u_{rel} is a roll parameter and therefore not important. Since circulation is governed by k it can be used as a primary paramter in a low-order model to predict circulation in a simultaneous pitching and rolling plate.

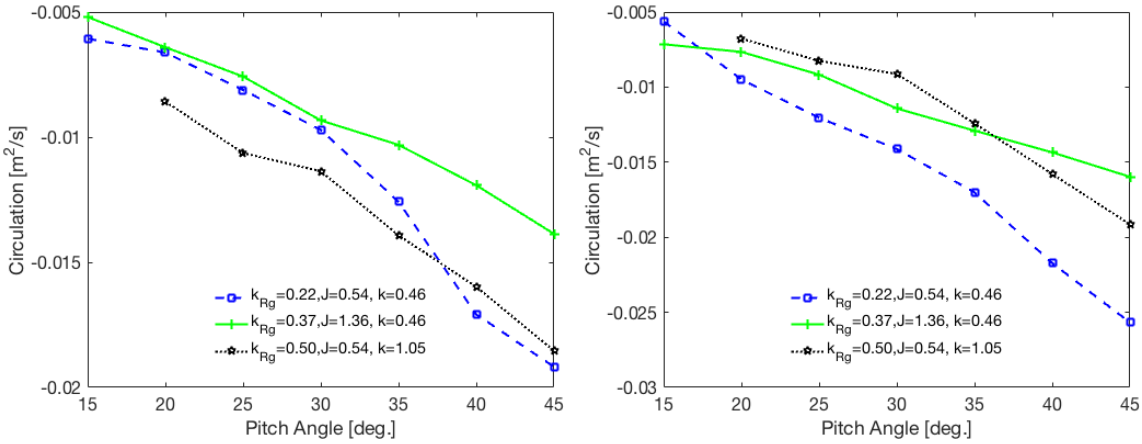

(a) z/b=0.35 (b) z/b=0.50

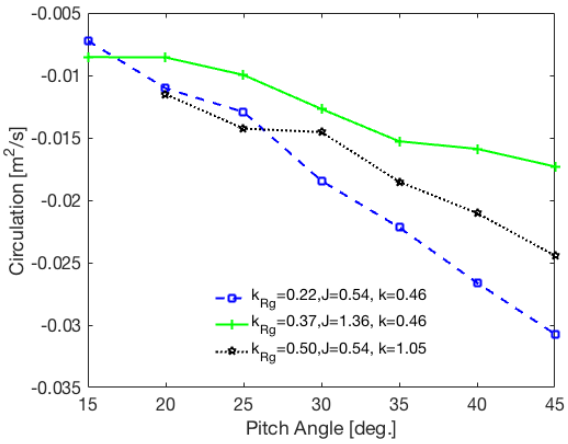

(c) z/b=0.65

Figure 7.6: Circulation comparison for the simultaneous case at z/b=0.35, z/b=0.50 and z/b=0.65.

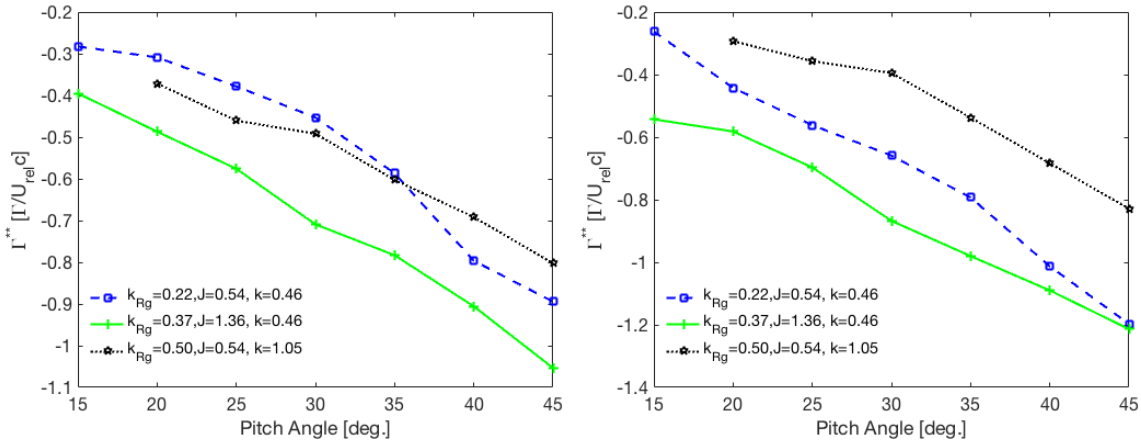

(a) z/b=0.35

(b) z/b=0.50

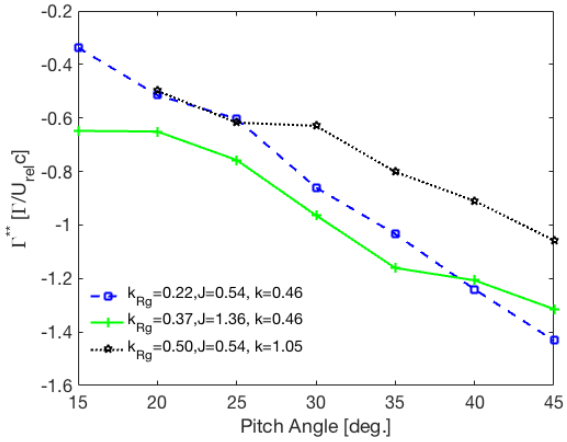

(c) z/b=0.65

Figure 7.7: Circulation comparison for the simultaneous case non-dimensionalized by u_{rel}*c at z/b=0.35, z/b=0.50 and z/b=0.65.

7.3 Conclusion

In this section a parameter k_{Rg} was defined to describe the effective pitch rate of a rolling and pitching plate, in which four different values of k_{Rg} were considered. The flow topology for k_{Rg} =0.22, 0.50 exhibited a compact outboard arch similar to that of baseline rolling case, it is important to note that J was equal to 0.54 for theses cases, as well. However, the LEV remained near the surface and more compact similar to that of the pitching plate. In the case of k_{Rg}=0.50 the arch begins to rebound to the surface at α=45 deg. and begins to appear similar to a pitching plate. In the case where a plate has a low advance coefficient the LEV will resemble that of a rolling wing, to some degree, mainly and outboard arch being formed, but once the wing begins the pitching maneuver the LEV will progress similar to a pitching wing LEV evolution. Vorticity transport analysis was applied to the four cases and found that across the span of the wing the individual contributions behaved similar to a pitching wing, where the shear layer contribution grows and is balanced by the diffusive contribution. It is important to note here, that this is not similar to Region 2 of the baseline roll case, where this type of balanced was observed. In that case an oscillation is seen due to the formation o the dual-vortex system, which is not observed in any of these cases. Circulation was shown to be a primary function for the reduced pitch rate, k, and not k_{Rg}. This knowledge can be used to create low-order models of a flat plate pitching and rolling by only using a single parameter, namely the reduced pitch rate to predict the circulation.

CHAPTER 8
FLOW CONTROL WITH PASSIVE BLEED

In this chapter it will be shown that by using the vorticity transport frame work, a given transport property can be targeted and manipulated to alter the LEV evolution. To do this the baseline pure roll case, $J_{3.25} = 0.54$, will be reexamined, this time a passive bleed hole will be introduced to the wing to target the attached region of the LEV. This passive bleed hole is hole that is passed from the pressure side of the wing, to the suction side. The LEV evolution for the passive bleed case will be examined and compared to baseline case.

8.1 Dye visualization

Dye visualizations were performed by Randal Berdon, for the rolling maneuver in the presence of a free stream. Preliminary visualizations with the absence of flow control were recorded at advance ratio values $J = 0.54$ and 1.36 at radius of gyration $R_g/c = 3.25$, this corresponds to $J_{3.25}$=0.54 and $J_{3.25}$=1.36, which were examined in detail in Chapter 5. In the preliminary visualizations a maximum roll angle of $\phi = 85°$ and effective angle of attack $\alpha_{eff} = 33°$ during the constant velocity phase was maintained. Flow visualizations were conducted for both $J_{3.25} = 0.54$ and $J_{3.25} = 1.36$ without passive bleed for comparison. All passive bleed cases that were conducted can be seen in table 8.1. A mixture of water-soluble glue along with fluorescein disodium salt was used to create visualizations of the vortex structure on the wing. For all visualizations, the glue-dye mixture was painted as a strip along the leading-edge of the wing.

Passive Flow Control Configurations				
Name	**Advance Ratio** (J)	**Hole Spanwise location** (z/b)	**Hole chordwise location** (x/c)	**Hole Diameter**(mm)
Baseline	0.54	N/A	N/A	N/A
p_{is}	0.54	0.1	0.065	1.6
p_{os}	0.54	0.16	0.065	1.6
p_{il}	0.54	0.1	0.065	3.2
p_{ol}	0.54	0.16	0.065	3.2

Table 8.1: Locations and sizes of passive bleed holes [9].

8.1.1 Qualitative Characterization of LEV Development using Flow Visualization

Preliminary flow visualizations were performed at $J_{3.25} = 0.54$ and $J_{3.25} = 1.36$ to identify important topological features and differences between the variation in advance ratio. Additional visualizations were performed on wing with an advance ratio $J = 0.54$ and the implementation of passive bleeding at various hole sizes and spatial locations to help understand the qualitative impact of each applied flow control configuration. Qualitative visualizations can help narrow the parameter space for quantitive measurements, vorticity transport analysis and help identify altered flux quantities.

Figure 8.1 shows a comparison of the evolution for a rolling wing with an advance ratio $J_{3.25} = 0.54$ and $J_{3.25} = 1.36$ respectively. At $\phi = 16°$ the flow features are signif-

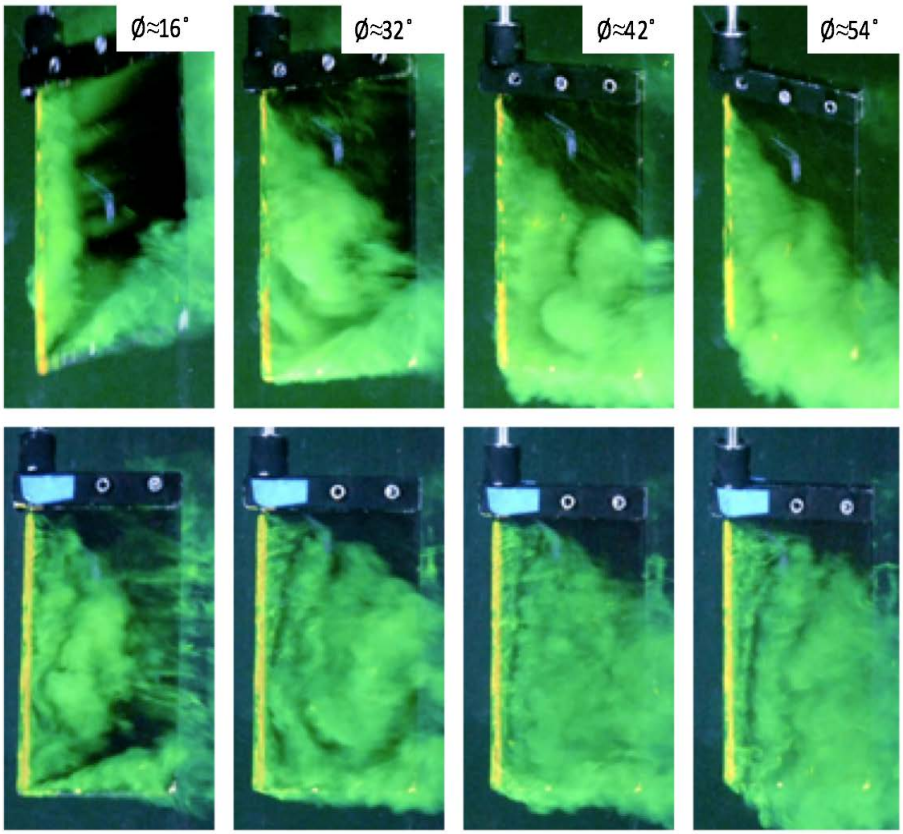

Figure 8.1: LEV evolution for (a) $J = 1.36$, $Rg/c = 3.25$, $\alpha_{eff} = 33°$ (b) $J = 1.36$, $Rg/c = 3.25$, $\alpha_{eff} = 33°$ taken by R. Berdon [9].

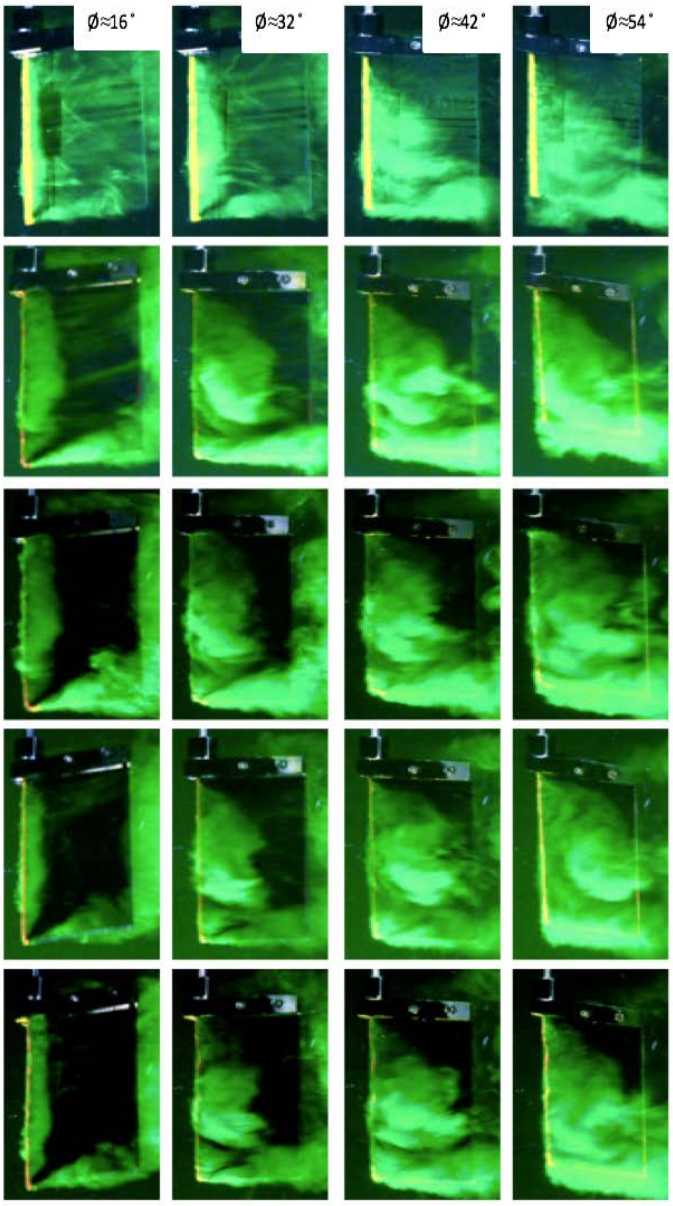

Figure 8.2: LEV evolution for $J = 0.54$, $R_g/c = 3.25$, $\alpha_{eff} = 33°$ with (Row 1) No bleeding (Row 2) Passive bleeding at $z/b \approx 0.1$, $d = 1.6$ mm (p_{is}) (Row 3) Passive bleeding at $z/b \approx 0.16$, $d = 1.6$ mm (p_{os}) (Row 4) Passive bleeding at $z/b \approx 0.1$, $d = 3.2$ mm (p_{il})(Row 5) Passive bleeding at $z/b \approx 0.16$, $d = 3.2$ mm (p_{ol}). Courtesy of R. Berdon [9].

icantly different. For $J_{3.25} = 0.54$, an LEV has rolled up across the span of the wing and remains attached. The $J_{3.25} = 1.36$ however, has generated an arch structure pinned at the root and the tip similar to that of a purely translating wing. As the wing progresses to $\phi = 32°$, the $J = 0.54$ wing has a coherent conical structure at the inboard position that extends to approximately the 50% spanwise position. This conical structure persists for the entirety of the motion. For the $J_{3.25} = 1.36$ case at $\phi = 32°$, arch structure has shed and convects downstream. A subsequent LEV has formed. This subsequent LEV is shed by $\phi = 54°$. This suggests that, for $J_{3.25} = 0.54$, rotational effects substantially alter LEV development.

Visualizations at different roll angles are shown in Figure 8.2 for a wing in the absence of passive bleeding in comparison to a wing with passive bleed at various configurations. The overall flow evolution for the different instances vary with the hole diameter and spatial location. For different sized holes and locations the LEV behavior is altered from the baseline case. This behavior can range form the baseline case behavior to an arch structure forming across the span similar to that of a translating wing at an angle of attack.

This method of passive bleeding appears to mitigate roll induced effects such that the flow near the wing resembles a purely translating case. This result suggests that this passive bleeding method is an effective way to decrease lift on a rolling wing as the LEV sheds. The greatest value of this passive bleeding case however, is that it provides a platform for understanding the flow mechanisms that govern LEV formation and evolution by fundamentally changing the flow while maintaining the same kinematics and geometry. The most effective configuration was the largest bleed at the most inboard location (i.e. z/b

= 0.1 and d = 3.2 mm).

8.2 Flow topology comparison

The evolution of the LEV for the flow control case is drastically different than the baseline case, shown in figure 8.3. Difference can be seen as early as $\phi = 6°$, where an arch structure is seen for the flow control case, figure 8.3a. As the motion progresses the attached region seen in the baseline case, is broken down into smaller shedding structures, leaving an arch LEV. By introducing the passive bleed hole to a the $J_{3.25} = 0.54$ is removes region one, but leaves the LEV evolving into an arch structure similar to that of a plunging wing or a pitching wing. Furthermore, the dual vortex system is not observed in the flow control case as well.

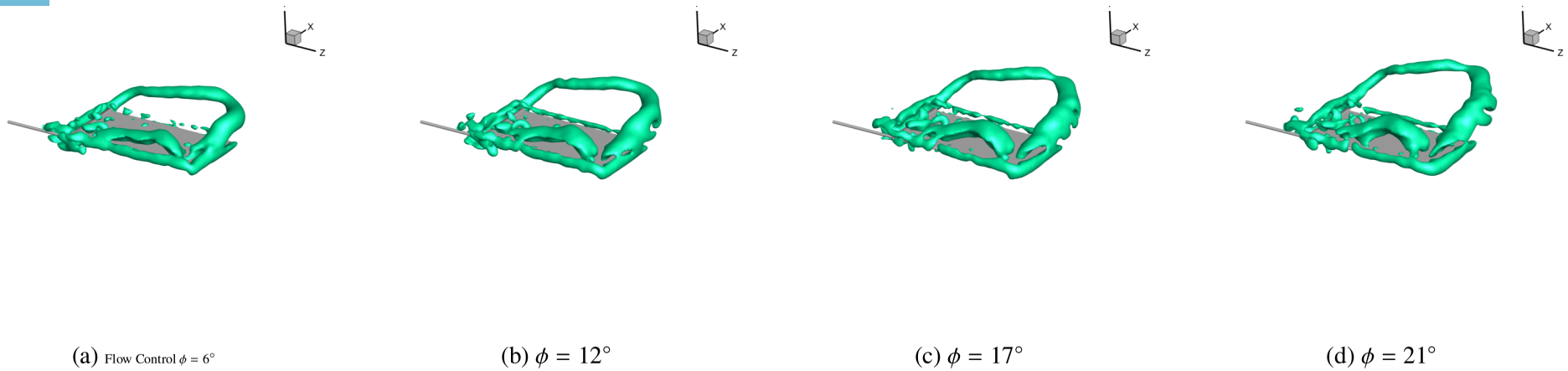

(a) Flow Control $\phi = 6°$ (b) $\phi = 12°$ (c) $\phi = 17°$ (d) $\phi = 21°$

(f) $J_{3.25}$=0.54,$\phi = 06°$ (g) $\phi = 12°$ (h) $\phi = 17°$ (i) $\phi = 21°$

Figure 8.3: LEV formation shown with isosurfaces of normalized swirling strength, for the flow control case (figs. 8.3a-8.3e), and the baseline case,$J_{3.25} = 0.54$ (figs.8.3f-8.3j), isosurface colored by $\lambda_{ci}/\lambda_{mac}$.

8.3 Vorticity Transport in the Passive Bleed Case

Figure 7.3 compares the transport contributions for the baseline $J_{3.25} = 0.54$, corresponding passive bleed, and the $J_{3.25} = 1.36$ cases at $z/b = 0.35$. The three cases in figure 7.3 were acquired by two different experimental methods. The $J = 0.54$ case (Fig. 8.4a) and $J = 1.36$ case (Fig.8.4b) used plenoptic PIV to capture the flow field. Particle tracking velocimetry was used to capture flowfield for the $J_{PB} = 0.54$ case (Fig. 8.4c), which is the passive bleed case. Important differences are evident that provide insight into the development of the leading-edge vortices in each case. Assessment of the circulation budget closure (i.e. comparison between the measured circulation and the right hand side (RHS) of Equation 3.13) suggests that the PTV has a larger error than the plenoptic PIV data – perhaps due, in part, to the smaller number of measurements in the averages – however, the deviation remains small with respect to the values of the dominant fluxes.

Qualitative differences are apparent in the behaviors of the shear-layer and diffusive fluxes between the fast and slow roll cases (Figs 8.4a and 8.4b, respectively). Whereas the slow roll case ($J_{3.25} = 1.36$) is affected by negligible spanwise convective flux, and the shear layer flux becomes approximately constant after a roll angle of $\phi = 30°$, the fast roll case ($J_{3.25} = 0.54$) exchanges a mostly monotonically decreasing diffusive flux for a complementary increasing spanwise convective flux as the roll angle increases. In both cases, the diffusive flux is on the same order of magnitude as the shear layer flux, and approximately mirrors the shear layer flux.

The passive bleed case provides an unique opportunity to perturb the fluxes in order to provide some insight into how changes in vorticity transport correlate with differences in

LEV evolution. Comparing the fluxes at z/b=0.35 for the passive bleed case (Fig. 7.3) to the fast and slow roll cases, it appears that the transport phenomena are more representative of the slow-roll case, despite having fast-roll kinematics. Specifically, the shear layer flux is relatively constant throughout the motion, and the spanwise flux does not form a significant portion of the budget. Thus, the application of passive bleed has disrupted the establishment of the spanwise flux. This increase in the spanwise flow has been correlated with the Coriolis acceleration (e.g. Jardin et al. [39]).

Looking further outboard at z/b=0.50, figure 8.5c compares the passive bleed case to the fast and slow roll cases. For the fast roll case the shear layer contribution is balanced by the diffusive contribution at this spanwise location with some source of vorticity from the spanwise convective contribution. The formation of the dual-vortex system causes the shear layer contribution and the diffusive contribution to oscillate. For the slow roll case the shear layer contribution decreases rapidly and then remains relatively constant, while there are oscillations in the diffusive contribution and the spanwise convective contribution, these are due to shedding events that are being aliased. The passive bleed case (Fig. 8.5c) is different than both of the other cases. In this case the shear layer contribution and diffusive contribution are relatively constant with a near zero spanwise convective contribution. Unlike both of the non passive bleed cases the the circulation grows monotonically with the grows of the LEV.

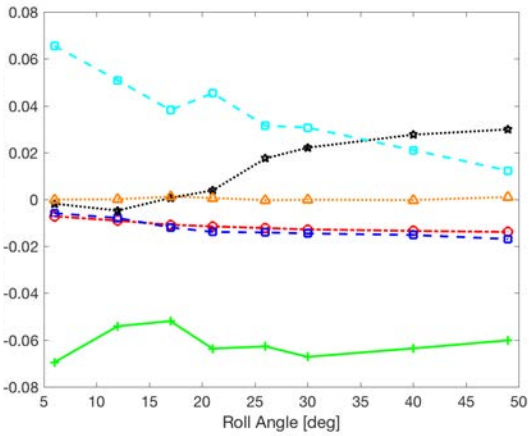

(a) $J_{3.25} = 0.54$

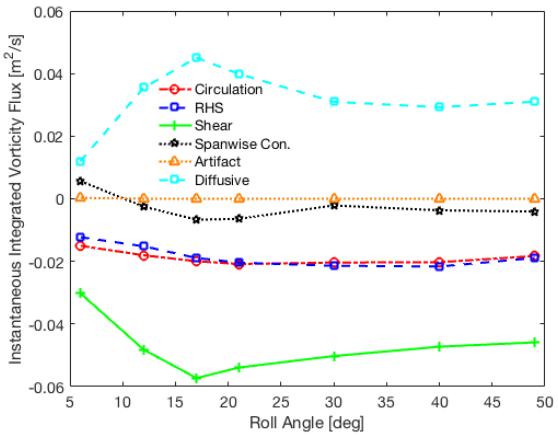

(b) $J = 1.36$

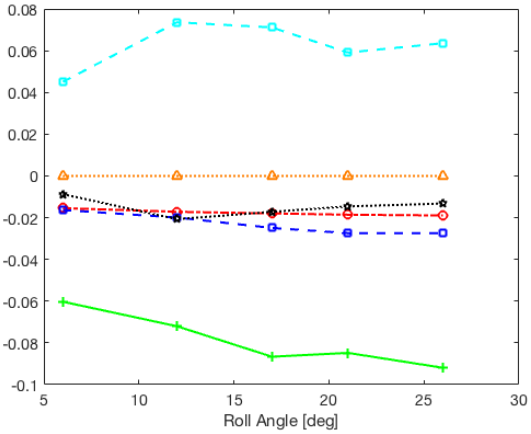

(c) $J_{PB} = 0.54$

Figure 8.4: Flux analysis at $z/b = 0.35$ for $J_{3.25} = 0.54$, J_{PB}=0.54 and J=1.36.

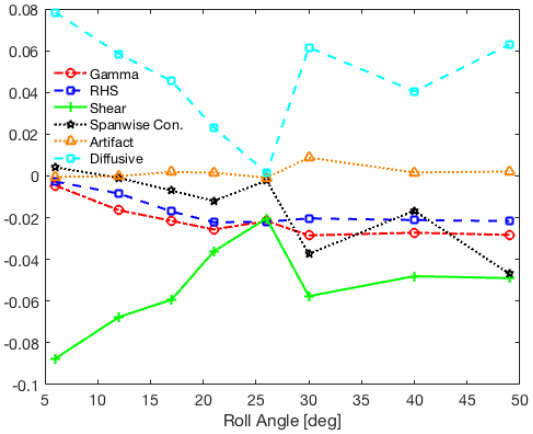

(a) $J_{3.25} = 0.54$

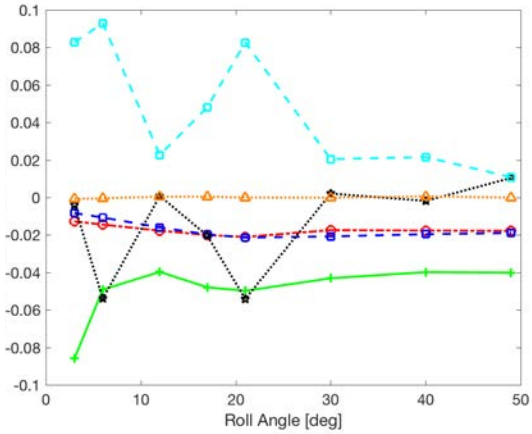

(b) $J = 1.36$

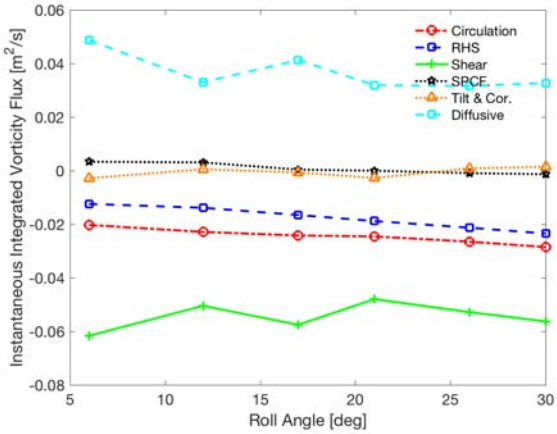

(c) $J_{PB} = 0.54$

Figure 8.5: Flux analysis at $z/b = 0.50$ for $J_{3.25} = 0.54$, J_{PB}=0.54 and J=1.36.

8.4 Conclusions

A passive bleed hole was added to the $J_{3.25} = 0.54$ case. From the addition of this passive bleed hole, the flow topology was fundamentally altered. The flow topology went from having three distinct regions, to forming into one large arch structure. The transport properties were altered from a growing spanwise convective contribution in Region 1, to the shear layer contribution balanced by the diffusive contribution. At the midspan no dual-vortex system was observed, and the shear layer contribution was balanced by the diffusive contribution as well. While the flow field and transport quantities were altered significantly, the circulation was marginally greater than the baseline case at the chosen spanwise locations. This section has two impacts, the first being, by using the vorticity transport framework, a region was identified and targeted to manipulate the global flow significantly. Secondly, since the flow fields were drastically different, yet the circulation was marginally great, perhaps flow structure doesn't doesn't contribute to the lift as much as previously thought.

CHAPTER 9
CONCLUSIONS AND FUTURE WORK

9.1 Conclusions

Analysis of a rectangular wing of aspect ratio two was examined for three maneuvers – pure roll, pure pitch and rolling and pitching wing–using a non-inertial vorticity transport framework. In Chapter 3, the vorticity transport equation was expanded with two new terms. The first being the Coriolis acceleration for a pitching maneuver, and second Coriolis term came from the rolling maneuver. By expanding this equation any rotating motion is accounted for. Furthermore, it was shown that the surface diffusive flux term is unaffected in the non- inertial frame, shown in Chapter 3.2, since it assumed to have a no slip condition on the surface of the plate.

When applying the vorticity transport framework to an airfoil performing a pure roll maneuver, it was shown that the Coriolis term did not significantly contribute to the vorticity transport. Instead it was found to be a correction to the measurements in the non-inertial frame. The baseline roll maneuver examined in Chapter 5, ($J_{3.25}$=0.54) exhibited three distinct regions. Region 1 was driven by the shear layer contribution which was a balance between the diffusive contribution early in the motion. As the spanwise flow developed the diffusive contribution dropped and there was a concomitant increase in the spanwise convective contribution. Region 2 was a balance between the shear layer contribution and the diffusive contribution, both which oscillated due to the forming of a dual-vortex system. Region 3 was the tip induced area, which was a balance between the

diffusive contribution and the spanwise convective contribution. The relative importance of the spanwise convective contribution was also described in this chapter and how it altered the bulk flow. The spanwise convective contribution in Region 1, is the classical spanwise convective sink attributed to LEV regulation on revolving wings. Region 2 is quasi 2D, but later in the motion is influence by an arch, vie Biot–Savart induction, which is propagating inboard. Region 3 is also arch induced, but from the other side of the arch. In this area the flow is toward the root of the plate, which is cause by arch induction pulling the flow inboard. This interaction from the tip and the arch in Region 3 cause the LEV to act as a reverse evolution process. Reducing the radius of gyration for this advance ratio caused the LEV to remain attached longer, while increasing the advance ratio caused LEV's to be shed rapidly from the leading edge.

In Chapter 6 a pure pitch maneuver was examined. From a topology perspective, the pitching maneuver forms an arch structure, which is similar to the Region 2, but is highly symmetrical and encompasses the majority of the span. The circulation can be collapsed if accounting for the initial boundary layer values making circulation affected by the reduced pitch rate early in the motion. The circulation magnitudes and function follow the angle of attack, once the initial value is accounted for. The diffusive flux and the shear layer contributions are functions of reduced pitch rate and angle of attack. In both the shear layer contribution and diffusive flux, a maximum is seen at an AoA of 25 deg. This is due to the secondary vorticity beginning to roll up, and accumulating for both cases.

In Chapter 7, a reduced effective pitch rate, k_{Rg}, was defined which accounted for the rolling maneuver and the pitching maneuver. Three different values of k_{Rg} were examined in

this section. The flow topology for k_{Rg} = 0.22, and 0.50 exhibited a compact outboard arch similar to that of baseline rolling case, but this was due to the fact the LEV had time to roll up before the pitching maneuver initiated. From the flow topology standpoint, J determined the LEV evolution early in the motion, but once the pitching maneuver initiated, k was the governing parameter. Vorticity transport analysis was applied to the three cases, and it was shown that the individual contributions behaved similar to a pitching wing, where the shear layer contribution grows and is balanced by the diffusive contribution. Circulation was shown to be a primary function for the reduced pitch rate, k, and not k_{Rg}. It was shown that neither J nor k_{Rg} predicated the behavior of the LEV, but rather solely k for the cases studied.

A passive bleed hole was introduced to the baseline roll case in Chapter 8 in an attempt to control and the alter the flow field. By consulting the vorticity transport analysis of the $J_{3.25}$ =0.54 case, and with guidance from flow visualization, a targeted strategy was implemented. This targeted strategy not only altered the flow field significantly, but also the transport contributions. From a topology standpoint, the flow field went from having three distinct regions in the baseline roll case, to forming an arch structure similar to a translating wing. The transport quantities were examined at z/b=0.35 and 0.50, which were vastly different from the baseline roll case. At z/b=0.35 the shear layer contribution was altered by the diffusive contribution, which showed negligible spanwise convective contribution. By adding the passive bleed hole at the chosen location the spanwise convective contribution was mitigated, thus impairing the mechanism of moving weak vorticity outboard from the inboard region, and increasing the diffusive contribution. This highlights that the

spanwise convective contribution is easily altered, and the diffusive contribution is a robust mechanism of vorticity transport.

While there have been many different flow structures that have been observed within this manuscript, but one feature that appears in each case is an arch structure. For the baseline rolling wing ($J_{3.25}$=0.54) and arch structure was observed in Region 2. For the pure pitching cases, a larger arch structure was observed, similar to that of a plunging plate. For the simultaneous cases, evidence showed that the LEV had begun to lift off the surface in a similar manner to the pitching case, leading to an arch structure. For the last case the passive bleed case evolved to an arch structure quickly. Even though each arch structure formed and evolved differently, the vorticity transport was similar. The shear layer contribution was balanced by the diffusive contribution, for the duration of the motion for each case. Furthermore, the diffusive contribution nearly mirrored the shear layer contribution for each of theses cases that formed an arch structure.

9.2 Future Work

Throughout this manuscript, there have been a few mechanisms that contributed to the growth and regulation of the LEV, namely the shear layer contribution, diffusive contribution and the spanwise convective contribution. The spanwise convective contribution was shown to be easily manipulated, and a relatively fragile transport mechanism. This leads most maneuvers to be a balance between the shear layer contribution and the diffusive contribution regulating the growth of the LEV.

By taking surface measurements on the surface of the wing, via pressure taps, these

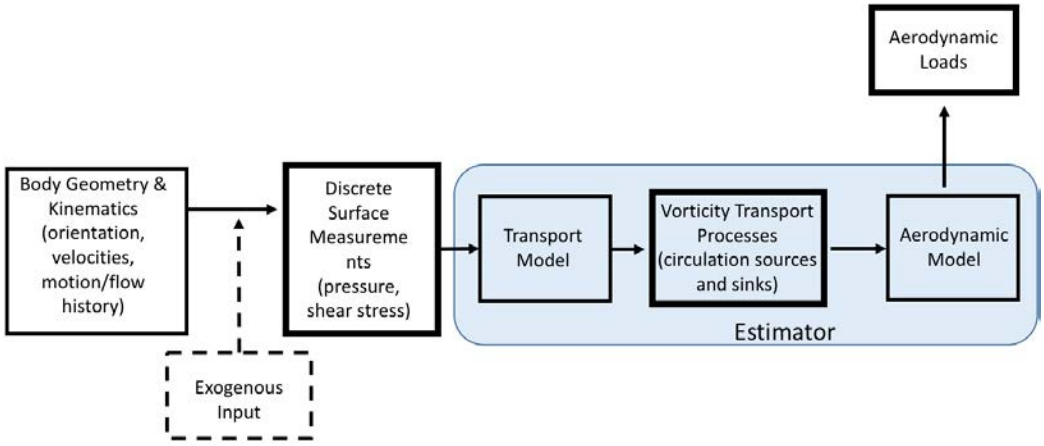

Figure 9.1: Flow chart depicting the use of vorticity transport processes can be inputed as an estimator to get the aerodynamic loads.

measurements can be used as inputs in to the estimator for a aerodynamic model, this can be implemented in the following way. The wing would be fitted with instrumentation to get shear stress on the leading edge and the pressure gradients from the surface of the wing, these are the only two measurements needed. For instance, if this instrumentation was fitted to a helicopter blade, that is trying to land in the air-wake of a super structure on a ship. This scenario will have two parts. The first part will be the purely rotating wing from the helicopter, and secondly an exogenous input when the shed vortices from the superstructure impinge on the rotor, and change the local angle of attack in time.

The need for future work show in figure 9.1 are two parts. The first is to extend the flux prediction capabilities of the transport model to predict spanwise fluxes based on surface pressure measurements. When transport is dominated by the shear layer and diffusive fluxes, then surface measurements tell most of the story, but what if the spanwise

flux is important? This is a logical next step. An important clue is that the sum of the spanwise and diffusive fluxes remains constant, so there must be some common underlying mechanism regulating these transport processes. The second is that these fluxes have to be related back to aerodynamic loads.

In this manuscript the vorticity transport was extended to incorporate rotational accelerations, and showed this diffusive flux term remains unaffected by rotation. It was also shown that in the majority of maneuvers, regulation of circulation was a balance by the diffusive contribution and the shear layer contribution. The future of this work, would be applying this knowledge, and using physical inputs to build a real time estimator of aerodynamic loads.

APPENDIX
UNCERTAINTY ANALYSIS

A.1 Uncertainty Analysis

This section provides an analysis that serves to quantify the uncertainties within the vorticity transport mechanism from Equation 3.13, the approach for which follows a technique developed by Wojcik [87]. In order to determine an appropriate estimate of the (maximum) uncertainty within the flux analyses that have been reported and discussed within Chapters 5-8.

The velocity vectors calculated from Plenoptic PIV images using the implementation of the MART algorithm, the plenoptic images were reconstructed into volumes using three iterations and a relaxation parameter μ=1.0. The convergence of the chordwise velocity of u is calculated for a $5x5x5$ vec^3 region, far away from the wing surface. Using 100 image pairs, the converged value is within 0.4 percent of the converged value using 500 pairs. In the core of the vortex, where the chordwise velocity is small, the averaged chordwise velocity is 15 percent larger using 100 pairs then the when using 500 pairs. However, just outside of the vortex core, the velocity from the 100 pair average is about 1 percent different than the final averaged velocity. To aid in quantification of measurement uncertainty of this particular application of plenoptic PIV, 1000 image pairs of freestream flow were gathered with the identical experimental arrangement and imaging parameters, with the wing removed. Using the same processing techniques, the vector fields were created and averaged. The standard deviation of each velocity component was calculated at every

point in the volume, allowing for the uncertainty to be quantified spatially. The velocity reported by Kyle Johnson components have uncertainty of approximately (percent of the freestream) velocity.

$$\sigma_{u'} = 2.3\% \tag{A.1}$$

$$\sigma_{v'} = 1.8\% \tag{A.2}$$

$$\sigma_{w'} = 4.0\% \tag{A.3}$$

The spanwise vorticity component was calculated via a central difference approximation. Using the uncertainties in the velocity components, the uncertainty in the vorticity values at any given point within the flow can be determined by:

$$\sigma_{\omega z} = \sqrt{\frac{\sigma_{v'}^2}{2X_g^2} + \frac{\sigma_{u'}^2}{2Y_g^2}} \tag{A.4}$$

where X_g and Y_g represent the horizontal and vertical vector spacing , both of which are 1.5 mm. This gives an maximum uncertainty in the spanwise vorticity data calculated within the control region was found to be:

$$\sigma_{\omega - zMAX} = 1.2(s^{-1}) \tag{A.5}$$

which gives a maximum error of

$$\sigma_{\omega_z - MAX} = 2.74\% \tag{A.6}$$

The circulation of the control region was found by multiplying the z-vorticity data by the differential area element given by $(X_g \cdot Y_g)$ and the summing all of the points within the control region. The total uncertainty of this area integral can be derived by adding the uncertainty from each point in quadrature. This gives the uncertainty of the circulation calculations can be found as:

$$\sigma_\Gamma = X_g Y_g \sqrt{\sum_{m=1}^{M} (\sigma_{\omega z})_m^2} \tag{A.7}$$

where $(\sigma_{\omega z})_m$ is the total uncertainty in the z-component of the vorticity vector located at a point within the control region and M is the total number of points within the control region.

$$\sigma_\Gamma = 0.00102 \ \ (\mathrm{m}^2/\mathrm{s}) \tag{A.8}$$

which is approximately 0.32% of the total circulation measured within the control region at that phase.

To properly conduct an error analysis, each term in the vorticity transport equation has to be analyzed. The in-plane convective flux is evaluated as:

$$\int_{1-3} \omega_z \, (\vec{u} \cdot \hat{n}) \, d\ell \tag{A.9}$$

The uncertainty in the convective flux through Boundaries 1-3 is found by summing the errors from each point along the boundary in quadrature:

$$\sigma_{Boundary\ 1} = \sqrt{\sum_{i=1}^{N_y} \left(\omega_z Y_g \sigma_{Ux}\right)_i^2 + \left(U_x Y_g \sigma_{\omega z}\right)_i^2} \tag{A.10}$$

$$\sigma_{Boundary\,2} = \sqrt{\sum_{j=1}^{N_x} \left(\omega_z X_g \sigma_{Uy}\right)_j^2 + \left(U_y X_g \sigma_{\omega z}\right)_j^2} \tag{A.11}$$

$$\sigma_{Boundary\,3} = \sqrt{\sum_{k=1}^{N_y} \left(\omega_z Y_g \sigma_{Ux}\right)_k^2 + \left(U_x Y_g \sigma_{\omega z}\right)_k^2} \tag{A.12}$$

where i, j and k specify a single point located on Boundaries 1, 2 and 3 respectively, N_y is the total number of points located on Boundaries 1 and 3 and N_x is the total number of points located on Boundary 2. Upon evaluating Equations A.10-A.12 the total uncertainty in the convective flux through the three boundaries comes out to be:

$$\sigma_{Boundary\,1} = 1.6700 \ (\mathrm{m}^2/\mathrm{s}^2) \tag{A.13}$$

$$\sigma_{Boundary\,2} = 0.0329 \ (\mathrm{m}^2/\mathrm{s}^2) \tag{A.14}$$

$$\sigma_{Boundary\,3} = 0.451 \ (\mathrm{m}^2/\mathrm{s}^2) \tag{A.15}$$

This gives a relative error of 1.93% for the convective term. The next term to consider are the X-tilting and Y-Tilting. Adding the sources of error in quadrature, the general uncertainty in the Y-tilting terms gives:

$$\begin{aligned}\sigma_{Y_{Tilting}} = \Bigg[&\left(\frac{\partial Y_{Tilting}}{\partial U_{x_{k+1}}}\sigma_{U_{x_{k+1}}}\right)^2 + \left(\frac{\partial Y_{Tilting}}{\partial U_{x_{k-1}}}\sigma_{U_{x_{k-1}}}\right)^2 + \left(\frac{\partial Y_{Tilting}}{\partial U_{z_{i+1}}}\sigma_{U_{z_{i+1}}}\right)^2 \\ &+ \left(\frac{\partial Y_{Tilting}}{\partial U_{z_{i-1}}}\sigma_{U_{z_{i-1}}}\right)^2 + \left(\frac{\partial Y_{Tilting}}{\partial U_{z_{j+1}}}\sigma_{U_{z_{j+1}}}\right)^2 + \left(\frac{\partial Y_{Tilting}}{\partial U_{z_{j-1}}}\sigma_{U_{z_{j-1}}}\right)^2 \\ &+ \left(\frac{\partial Y_{Tilting}}{\partial X_g}\sigma_{X_g}\right)^2 + \left(\frac{\partial Y_{Tilting}}{\partial Y_g}\sigma_{Y_g}\right)^2 + \left(\frac{\partial Y_{Tilting}}{\partial Z_g}\sigma_{z_g}\right)^2\Bigg]^{\frac{1}{2}}\end{aligned} \tag{A.16}$$

Carrying out this calculation for an area with large gradients its seen that 0.053 m^2/s^2 is the error, or the relative error is 3.83%. This calculation can be similarly done for the X-tilting term.

The general uncertainty in the X-tilting is expressed in Equation A.17 assuming the contributions of the errors can be added in quadrature.

$$\sigma_{X_{Tilting}} = \left[\left(\frac{\partial X_{Tilting}}{\partial U_{z_{j+1}}}\sigma_{U_{z_{j+1}}}\right)^2 + \left(\frac{\partial X_{Tilting}}{\partial U_{z_{j-1}}}\sigma_{U_{z_{j-1}}}\right)^2 + \left(\frac{\partial X_{Tilting}}{\partial U_{y_{k+1}}}\sigma_{U_{y_{k+1}}}\right)^2 + \left(\frac{\partial X_{Tilting}}{\partial U_{y_{k-1}}}\sigma_{U_{y_{k-1}}}\right)^2 + \left(\frac{\partial X_{Tilting}}{\partial U_{z_{i+1}}}\sigma_{U_{z_{i+1}}}\right)^2 + \left(\frac{\partial X_{Tilting}}{\partial U_{z_{i-1}}}\sigma_{U_{z_{i-1}}}\right)^2 + \left(\frac{\partial X_{Tilting}}{\partial X_g}\sigma_{X_g}\right)^2 + \left(\frac{\partial X_{Tilting}}{\partial Y_g}\sigma_{Y_g}\right)^2 + \left(\frac{\partial X_{Tilting}}{\partial Z_g}\sigma_{Z_g}\right)^2\right]^{\frac{1}{2}} \quad \text{(A.17)}$$

This gives an error of 3.83%. The diffusive flux was characterized using the following relation:

$$\text{Diffusive} = \frac{1}{\rho}\int_4 \frac{\partial p}{\partial x} dx \quad \text{(A.18)}$$

Which can be physically calculated as:

$$\text{Diffusive} = \frac{1}{\rho}(p_b - p_a) \quad \text{(A.19)}$$

where p_a and p_b are the pressures on the surface of the airfoil at the start and end of the control region respectively. Assuming that the total uncertainty in the pressure data is the same at both points (σ_p = 0.84 Pa), the total uncertainty in the diffusive flux can be calculated as:

$$\sigma_{Diffusive} = \frac{\sigma_p}{\rho\sqrt{2}} \quad \text{(A.20)}$$

$$\sigma_{Diffusive} = 0.434 \ (\text{m}^2/\text{s}^2) \quad \text{(A.21)}$$

which is approximately 0.28% of the maximum diffusive flux.

REFERENCES

[1] M. Acharya and M. H. Metwally. Unsteady pressure field and vorticity production over a pitching airfoil. *AIAA J.*, 30(2):403–411, 1992.

[2] J. M. Akkala, A. Eslam Panah, and J. H. J. Buchholz. Vortex dynamics and performance of flexible and rigid plunging airfoils. 2014. Accepted.

[3] James M. Akkala and James H. J. Buchholz. Vorticity transport mechanisms governing the development of leading-edge vortices. *Journal of Fluid Mechanics*, 829:512?537, 2017.

[4] D. L. Altshuler, R. Dudley, and C. P. Ellington. Aerodynamic forces of revolving hummingbird wings and wing models. 264:327–332, 2004.

[5] J.-Z. Wu an Y.-T. Yan, Y.-B. Luo, and C. Pozrikidis. Fluid kinematics on a deformable surface. *J. Fluid Mech.*, 541:371–381, 2005.

[6] J. Andreopoulos and J.H. Agui. Wall-vorticity flux dynamics in a two-dimensional turbulent boundary layer. *J. Fluid Mech.*, 309:45–84, 1996.

[7] S A Ansari, R Żbikowski, and K Knowles. Non-linear unsteady aerodynamic model for insect-like flapping wings in the hover. part 1: Methodology and analysis. *Proceedings of the Institution of Mechanical Engineers, Part G: Journal of Aerospace Engineering*, 220(2):61–83, 2006.

[8] H. R. Beem, D. E. Rival, and M. S. Triantafyllou. On the stabilization of leading-edge vortices with spanwise flow. *Expts. Fluids*, 52:511–517, 2012.

[9] R. Berdon. Flow structure and aerodynamic loads of a rolling wing in a free stream. Master's thesis, University of Iowa, 2018.

[10] J. M. Birch and M. H. Dickinson. Spanwise flow and the attachment of the leading-edge vortex on insect wings. 412:729–733, 2001.

[11] M. Brons, M. C. Thompson, T. Leweke, and K. Hourigan. Vorticity generation and conservation for two-dimensional interfaces and boundaries. *J. Fluid Mech.*, 758:63–93, 2014.

[12] M. Bross, C.A. Ozen, and D. Rockwell. Flow structure on a rotating wing: Effect of steady incident flow. *Phys. Fluids*, 25:081901, 2013.

[13] J. H. J. Buchholz, M. A. Green, and A. J. Smits. Scaling the circulation shed by a pitching panel. *J. Fluid Mech.*, 688:591–601, 2011.

[14] Abel-John Buchner, Nicolas Buchmann, Kareem Kilany, Callum Atkinson, and Julio Soria. Stereoscopic and tomographic piv of a pitching plate. *Experiments in Fluids*, 52(2):299–314, Feb 2012.

[15] Zakery R. Carr, Adam C. DeVoria, and Matthew J. Ringuette. Aspect-ratio effects on rotating wings: circulation and forces. *Journal of Fluid Mechanics*, 767:497?525, 2015.

[16] Anna C. Carruthers, Adrian L. R. Thomas, and Graham K. Taylor. Automatic aeroelastic devices in the wings of a steppe eagle aquila nipalensis. *Journal of Experimental Biology*, 210(23):4136–4149, 2007.

[17] K. K. Chen, T. Colonius, and K. Taira. The leading-edge vortex and quasisteady vortex shedding on an accelerating plate. *Phys. Fluids*, 22, 2010. Art. 033601.

[18] J. Choi, T. Colonius, and D. R. Williams. Surging and plunging oscillations of an airfoil at low reynolds number. *J. Fluid Mech.*, 763:237–253, 2015.

[19] A. C. DeVoria and M. J. Ringuette. Vortex formation and saturation for low-aspect-ratio rotating flat-plate fins. *Expts. Fluids*, 52(2):441–462, 2012.

[20] M. H. Dickinson, F. Lehmann, and S. P. Sane. Wing rotation and the aerodynamic basis of insect flight. 284(5422):1954–60, 1999.

[21] T. L. Doligalski, C. R. Smith, and J. D. A. Walker. Vortex interactions with walls. *Annu. Rev. Fluid Mech.*, 26:573–616, 1994.

[22] C. E. Doyle, J. J. Bird, T. A. Isom, J. C. Kallman, D. F. Bareiss, D. J. Dunlop, R. J. King, J. J. Abbott, and M. A. Minor. An avian-inspired passive mechanism for quadrotor perching. *IEEE/ASME Transactions on Mechatronics*, 18(2):506–517, 2013.

[23] J. D. Eldredge, C. Wang, and M. V. OL. A computational study of a canonical pitch-up, pitch-down maneuver. In *39th AIAA Fluid Dynamics Conference*, San Antonio, TX, 2009. AIAA. AIAA Paper 2009-3687.

[24] Jeff D. Eldredge and Anya R. Jones. Leading-edge vortices: Mechanics and modeling. *Annual Review of Fluid Mechanics*, 51(1):75–104, 2019.

[25] C. P. Ellington, C. van den Berg, A. P. Willmott, and A. L. R. Thomas. Leading-edge vortices in insect flight. *Nature*, 384:626–630, 1996.

[26] A. Eslam Panah and J. H. J. Buchholz. Parameter dependence of vortex interactions on a two-dimensional plunging plate. *Expts. Fluids*, 55(3):1687, 2014.

[27] D. J. Garmann and M. R. Visbal. Dynamics of revolving wings for various aspect ratios. *J. Fluid Mech.*, 748:932–956, 2014.

[28] Daniel Garmann and Miguel Visbal. *Three-Dimensional Flow Structure and Aerodynamic Loading on a Low Aspect Ratio, Revolving Wing*. American Institute of Aeronautics and Astronautics, 2018/09/27 2012.

[29] M. Gharib, E. Rambod, and K Shariff. A universal time scale for vortex ring formation. *J. Fluid Mech.*, 360:121–140, 1998.

[30] Kenneth O. Granlund, Michael V. Ol, and Luis P. Bernal. Unsteady pitching flat plates. *Journal of Fluid Mechanics*, 733:R5, 2013.

[31] I. Gursul, R. Gordnier, and M. Visbal. Unsteady aerodynamics of nonslender delta wings. *Progress in Aerospace Sciences*, 41(7):515 – 557, 2005.

[32] Patrick Hammer. A discrete vortex method application to low reynolds number aerodynamic flows, 05 2011.

[33] P.W. Hammerton and E.J. Kerschen. Leading-edge receptivity for bodies with mean aerodynamic loading. *J. Fluid Mech.*, 535:1–32, 2005.

[34] R. R. Harbig, J. Sheridan, and M. C. Thompson. Reynolds number and aspect ratio effects on the leading-edge vortex for rotating insect wing planforms. *Journal of Fluid Mechanics*, 717:166?192, 2013.

[35] A. Hondan and J. Andreopoulos. Instantaneous three-dimensional vorticity measurements in vortical flow over a delta wing. *AIAA J.*, 35(10):1612–1620, 1997.

[36] H.-Y. Ma J.-Z. Wu and M.-D. Zhou. *Vorticity and Vortex Dynamics*. Springer, 2007.

[37] R. Jantzen, K. Taira, K. Granlund, and M. Ol. Vortex dynamics around pitching plates. *Phys. Fluids*, 26, 2014. Art. 053606.

[38] Ryan T. Jantzen, Kunihiko Taira, Kenneth O. Granlund, and Michael V. Ol. Vortex dynamics around pitching plates. *Physics of Fluids*, 26(5):053606, 2014.

[39] T. Jardin and T. Colonius. On the lift-optimal aspect ratio of a revolving wing at low reynolds number. *Journal of The Royal Society Interface*, 15(143), 2018.

[40] T. Jardin and L. David. Spanwise gradients in flow speed help stabilize leading-edge vortices on revolving wings. *Phys. Rev. E*, 90:013011, Jul 2014.

[41] T. Jardin and L. David. Coriolis effects enhance lift on revolving wings. *Phys. Rev. E*, 91:031001, Mar 2015.

[42] K. Johnson, B. Thurow, K. Wabick, R. Berdon, and J. Buchholz. Vortex topology of a pitching and rolling wing in forward flight. *J. Fluid Mech.*, NA:NA, 2019.

[43] A. R. Jones and H. Babinsky. Reynolds number effects on leading edge vortex development on a waving wing. *Expts. Fluids*, 51:197–210, 2011.

[44] E. J. JUMPER, S. J. SCHRECK, and R. L. DIMMICK. Lift-curve characteristics for an airfoil pitching at constant rate. *Journal of Aircraft*, 24(10):680–687, 2018/09/25 1987.

[45] D. Kim and M. Gharib. Experimental study of three-dimensional vortex structures in translating and rotating plates. *Expts. Fluids*, 49:329–339, 2010.

[46] J. Kriegseis, M. Kinzel, and D. Rival. On the persistence of memory: do initial conditions impact vortex formation? *J. Fluid Mech.*, 736:91–106, 2013.

[47] C.H. Kuo and J.K. Hsieh. Unsteady flow structure and vorticity convection over the airfoil oscillating at high reduced frequency. *Exp. Therm. and Fluid Science*, 24:117–129, 2001.

[48] D. Lentink and M. H. Dickinson. Biofluiddynamic scaling of flapping, spinning, and translating fins and wings. *J. Exp. Biol.*, 212:2691–2704, 2009.

[49] D. Lentink and M. H. Dickinson. Rotational accelerations stabilize leading edge vortices on revolving fly wings. *J. Exp. Biol.*, 212:2705–2719, 2009.

[50] G. C. Lewin and H. Haj-Hariri. Modelling thrust generation of a two-dimensional heaving airfoil in a viscous flow. *J. Fluid Mech.*, 492:339–362, 2003.

[51] M. J. Lighthill. Introduction. boundary layer theory. In L. Rosenhead, editor, *Laminar boundary Layers*, pages 46–113. Oxford University Press, London, 1963.

[52] Field Manar, Peter Mancini, David Mayo, and Anya R. Jones. Comparison of rotating and translating wings: Force production and vortex characteristics. *AIAA Journal*, 54(2):519–530, 2018/09/24 2015.

[53] Peter Mancini, Field Manar, Kenneth Granlund, Michael V. Ol, and Anya R. Jones. Unsteady aerodynamic characteristics of a translating rigid wing at low reynolds number. *Physics of Fluids*, 27(12):123102, 2015.

[54] T. Maxworthy. Experiments on the Weis-Fogh mechanism of lift generation by insects in hovering flight. Part 1. Dynamics of the 'fling'. *J. Fluid Mech.*, 93(1):47–63, 1979.

[55] B. R. Morton. The generation and decay of vorticity. 28:277–308, 1984.

[56] R. C. Nelson and A. Pelletier. The unsteady aerodynamics of slender wings and aircraft undergoing large amplitude maneuvers. *Progress in Aerospace Sciences*, 39:185–248, 2003.

[57] Michael OL, Aaron Altman, Jeff Eldredge, Daniel Garmann, and Yongsheng Lian. *Résuméof the AIAA FDTC Low Reynolds Number Discussion Group's Canonical Cases*. American Institute of Aeronautics and Astronautics, 2018/09/24 2010.

[58] Kyohei Onoue and Kenneth S. Breuer. Vortex formation and shedding from a cyber-physical pitching plate. *Journal of Fluid Mechanics*, 793:229?247, 2016.

[59] C. A. Ozen and D. Rockwell. Flow structure on a rotating plate. *Expts. Fluids*, 52(1):207–223, 2012.

[60] A. Eslam Panah. *Flow Structure and Vorticity Transport on a Plunging Wing*. PhD thesis, University of Iowa, 2014.

[61] A. Eslam Panah, J.M. Akkala, and J.H.J. Buchholz. Vorticity transport and the leading-edge vortex of a plunging airfoil. *Expts. Fluids*, 2015.

[62] J. Panda and K. B. M. Q. Zaman. Experimental investigation of the flow field of an oscillating airfoil and estimation of lift from wake surveys. *J. Fluid Mech.*, 265:65–95, 1994.

[63] C. W. Pitt Ford and H. Babinsky. Lift and the leading edge vortex. In *50th AIAA Aerospace Sciences Meeting*, Nashville, TN, January 2012. AIAA Paper 2012-911.

[64] C. W. Pitt Ford and H. Babinsky. Lift and the leading-edge vortex. *Journal of Fluid Mechanics*, 720:280?313, 2013.

[65] Charles W. Pitt Ford and Holger Babinsky. Impulsively started flat plate circulation. *AIAA Journal*, 52(8):1800—1802, 2018/09/24 2014.

[66] E. Polhamus. Predictions of vortex-lift characteristics by a leading-edge suction analogy. *Expts. Fluids*, 8(4):193–199, 1971.

[67] M. C. Potter and J. F. Foss. *Fluid Mechanics*. Great Lakes Press, Inc., Okemos, MI, 1982.

[68] D. I. Pullin and Z. J. Wang. Unsteady forces on an accelerating plate and application to hovering insect flight. *J. Fluid Mech.*, 509:1–21, 2004.

[69] D. Rival, J. Kriegseis, P. Schaub, A. Windmann, and C. Tropea. A criterion for vortex separation on unsteady aerodynamic profiles. January 2013. AIAA Paper 2013-0836.

[70] D. Rival, T. Prangemeier, and C. Tropea. The influence of airfoil kinematics on the formation of leading-edge vortices in bio-inspired flight. *Expts. Fluids*, 46:823–833, 2009.

[71] Daniel Schanz, Andreas Schröder, Sebastian Gesemann, Dirk Michaelis, and Bernhard Wieneke. 'shake the box': A highly efficient and accurate tomographic particle tracking velocimetry (tomo-ptv) method using prediction of particle positions. pages 1–13, 01 2013.

[72] Ryan M. Shelton, Brandon E. Jackson, and Tyson L. Hedrick. The mechanics and behavior of cliff swallows during tandem flights. *Journal of Experimental Biology*, 217(15):2717–2725, 2014.

[73] C. Shih and C.M. Ho. Vorticity balance and time scales of a two-dimensional airfoil in an unsteady free stream. *Phys. Fluids*, 6, 1994.

[74] C. SHIH, L. LOURENCO, L. VAN DOMMELEN, and A. KROTHAPALLI. Unsteady flow past an airfoil pitching at a constant rate. *AIAA Journal*, 30(5):1153–1161, 2018/09/25 1992.

[75] W. Shyy, P. Trizilla, C. k. Kang, and H. Aono. Can tip vortices enhance lift of a flapping wing? *AIAA J.*, 47(2):289–293, 2009.

[76] J. H. STRICKLAND and G. M. GRAHAM. Force coefficients for a naca-0015 airfoil undergoing constant pitchrate motions. *AIAA Journal*, 25(4):622–624, 2018/09/25 1987.

[77] K. Taira and T. Colonius. Three-dimensional flows around low-aspect-ratio flat-plate wings at low reynolds numbers. *J. Fluid Mech.*, 623:187–207, 2009.

[78] J. L. Tangler. The nebulous art of using wind tunnel aerofoil data for predicting rotor performance. 4(2-3):245–257, 2002.

[79] J. R. Usherwood and C. P. Ellington. The aerodynamics of revolving wings i. model hawkmoth wings. *J. Exp. Biol.*, 205:1547–1564, 2002.

[80] J. R. Usherwood and C. P. Ellington. The aerodynamics of revolving wings ii. propeller force coefficients from mayfly to quail. *J. Exp. Biol.*, 205:1565–1576, 2002.

[81] L.L. van Dommelen and S.F. Shen. The spontaneous generation of the singularity in a separating laminar boundary layer. *J. Comp. Phys.*, 38:125–140, 1980.

[82] M. R. Visbal. Flow structure and unsteady loading over a pitching and perching low-aspect-ratio wing. In *42nd AIAA Fluid Dynamics Conference.*, New Orleans, Louisiana, 2012. AIAA Paper 2012-3279.

[83] Miguel R. Visbal. Unsteady flow structure and loading of a pitching low-aspect-ratio wing. *Phys. Rev. Fluids*, 2:024703, Feb 2017.

[84] MIGUEL R. VISBAL and J. S. SHANG. Investigation of the flow structure around a rapidly pitching airfoil. *AIAA Journal*, 27(8):1044–1051, 2018/09/25 1989.

[85] JOHN WALKER and DAVID CHOU. *Forced unsteady vortex flows driven by pitching airfoils*. American Institute of Aeronautics and Astronautics, 2018/09/25 1987.

[86] A. Widmann and C. Tropea. Parameters influencing vortex growth and detachment on unsteady aerodynamic profiles. *J. Fluid Mech.*, 773:432–459, 2015.

[87] C. J. Wojcik. The dynamics of spanwise vorticity on a rotating flat plate in a starting motion. Master's thesis, University of Iowa, 2012.

[88] C. J. Wojcik and J. H. J. Buchholz. Parameter variation and the leading-edge vortex of a rotating flat plate. *AIAA J.*, 52(2):348–357, 2014.

[89] C. J. Wojcik and J. H. J. Buchholz. Vorticity transport in the leading-edge vortex on a rotating blade. *J. Fluid Mech.*, 743:249–261, 2014.

[90] M. Wolfinger and D. Rockwell. Flow structure on a rotating wing: effect of radius of gyration. *Journal of Fluid Mechanics*, 755:83?110, 2014.

[91] Maxwell Wolfinger and Donald Rockwell. Transformation of flow structure on a rotating wing due to variation of radius of gyration. *Experiments in Fluids*, 56(7):137, Jun 2015.

[92] JaimeG. Wong and DavidE. Rival. Determining the relative stability of leading-edge vortices on nominally two-dimensional flapping profiles. *Journal of Fluid Mechanics*, 766:611?625, 2015.

[93] J. Wu and J. Wu. Boundary vorticity dynamics since lighthill's 1963 article: Review and development. *Theo. Comp. Fluid Dyn.*, pages 459–474, 1998.

[94] J. Z. Wu and J. M Wu. Interactions between a solid surface and a viscous compressible flow field. *J. Fluid Mech.*, 254:183–211, 1993.

[95] J. Z. Wu, X. H. Wu, and J. M. Wu. Streaming vorticity flux from oscillating walls with finite amplitude. *Phys. Fluids*, 5(8):1933–1938, 1993.

[96] J.Z. Wu, R.L. Roach, C.F. Lo, F.L. Zhu, R. M. Dowgwillo, L.B. Jiang, and R.W. Tramel. Aerodynamic diagnostics and design based on boundary vorticity dynamicsl. In *17th AIAA Applied Aerodynamics Conference*, Norfolk, Virginia, June-July 1999. AIAA 99-3103.

[97] Xi Xia and Kamran Mohseni. *Trapped Vortex on a Flat Plate: Equilibrium and Stability*. American Institute of Aeronautics and Astronautics, 2018/09/27 2012.

[98] T. O. Yilmaz and D. Rockwell. Flow structure on finite-span wings due to pitch-up motion. *Journal of Fluid Mechanics*, 691:518?545, 2012.

[99] Huai-Te Yu and Luis P Bernal. Experimental investigation of three-dimensional flow development by pitching low-aspect-ratio wing, 01 2016.